

1-1-2010

A Study Of Structure-Property Correlation In V₂O₅ And TiO₂ Based Thin Films As Functional Materials

Chandra Thapa
Wayne State University,

Follow this and additional works at: http://digitalcommons.wayne.edu/oa_dissertations

Recommended Citation

Thapa, Chandra, "A Study Of Structure-Property Correlation In V₂O₅ And TiO₂ Based Thin Films As Functional Materials" (2010).
Wayne State University Dissertations. Paper 32.

This Open Access Dissertation is brought to you for free and open access by DigitalCommons@WayneState. It has been accepted for inclusion in Wayne State University Dissertations by an authorized administrator of DigitalCommons@WayneState.

**A STUDY OF STRUCTURE-PROPERTY CORRELATION IN V₂O₅ AND TiO₂
BASED THIN FILMS AS FUNCTIONAL MATERIALS**

by

CHANDRA THAPA

DISSERTATION

Submitted to the Graduate School

of Wayne State University,

Detroit, Michigan

in partial fulfillment of the requirements

for the degree of

DOCTOR OF PHILOSOPHY

2010

MAJOR: PHYSICS

Approved by:

Advisor

Date

Co-Advisor

Date

Dedication

To my Family

Acknowledgements

I am much indebted to my advisor Dr. Ratna Naik for her guidance and support throughout the completion of this Dissertation. I would never have come to this position without her guidance and support. She is the person of greatest inspiration in my life. I am also indebted to Dr. Vaman Naik for his crucial support and guidance to complete this work.

I would like to thank my advisor Dr. K. R. Padmanabhan for his help and suggestions throughout the completion of this work. His help beyond the academia is appreciated. I would like to thank Dr. Simon Ng for his useful suggestions, specifically during the prospectus phase of this work.

I would like to express my sincere thanks to Dr. Sahana & Dr. Sudakar with whom all my PhD work is connected. They have enormous contribution to every bit of my Dissertation work. They were my informal advisors throughout my PhD work and will be always remembered for their enormous help and support.

I would like to thank my master thesis advisor Dr. Gavin Lawes for his guidance throughout my master and PhD work. His help and suggestions were crucial in many steps of this research.

I would like to thank Dr. Payson for his every kind of help and encouragement in some difficult circumstances. I will always remember Dr. Karchin for his support during the processing period of my PhD application. I would not have been here without his help and consideration for my admission into this program.

Special thanks go to Ambesh Dixit for his help in many experimental measurements. He is a brilliant guy with magical experimental efficiency. I would like to thank Dr. Talagala for her help during the beginning of this work. Thanks to Rajesh Regmi for sharing many things both outside and inside the academia. All other personnel and colleagues who helped me in one way or another during my stay in the physics department will be remembered. Many thanks to Dr. Wadehra and other staff members of the department for their help!

My family is the source of greatest support and encouragement in every up and down of my life. I would never have been to this stage of life without their endless support regardless of enormous pains and sufferings.

TABLE OF CONTENTS

Dedication.....	ii
Acknowledgements.....	iii
Table of Contents.....	v
List of Tables.....	vi
List of Figures.....	vii
Chapter 1: INTRODUCTION.....	1
Chapter 2: SYNTHESIS AND CHARACTERIZATION METHODS.....	24
Chapter 3: ELECTROCHEMICAL PROPERTIES OF V ₂ O ₅ THIN FILMS.....	56
Chapter 4: ELECTROCHEMICAL PROPERTIES OF V ₂ O ₅ -TiO ₂ COMPOSITES.....	79
Chapter 5: DIELECTRIC PROPERTIES OF TiO ₂ THIN FILMS.....	104
Chapter 6: SUMMARY AND CONCLUSIONS.....	132
References.....	136
Abstract.....	153
Autobiographical Statement.....	155

List of Tables

Table 3.1	Peak potential and current density, intercalation/deintercalation capacity as deduced from the CV at a scan rate of 2mV/sec for V ₂ O ₅ thin films, together with difference in the cathode and corresponding anode peak current density.....	73
Table 3.2	The difference in (EP _{a1} -EP _{c2}) at a scan rate of 0.5 and 30 mV/sec and the difference in (EP _{a2} -EP _{c1}) at a scan rate of 0.5 and 30 mV/sec, together with the slope and the diffusion coefficient (cm ² /sec) corresponding to the peaks as measured form the Randles-Sevčik plot for three V ₂ O ₅ thin films.....	74
Table 4.1	The changes in the optical band gap and the appearance of IR active modes due to the symmetry breaking caused by oxygen vacancies of TiO ₂ -V ₂ O ₅ thin films.....	87
Table 4.2	Peak potential and current density, intercalation/deintercalation capacity as deduced from the CV at a scan rate of 2mV/sec for V ₂ O ₅ thin films.....	97
Table 4.3	The diffusion coefficient (cm ² /sec) corresponding to the peaks as measured form the Randles-Sevčik plot for three V ₂ O ₅ thin films.....	100
Table 5.1	Slopes of SCLC plots (High Field region).....	124
Table 5.2	Slopes of PF plots (High Field region).....	126
Table 5.3	Fitting parameters from Cole-Cole analysis of dielectric data.....	129

List of Figures

Figure 1.1	Volumetric and gravimetric energy density of different battery technologies.....	3
Figure 1.2	Charging and discharging process in a typical rechargeable lithium-ion battery.....	5
Figure 1.3	Open circuit diagram of a cell.....	6
Figure 1.4	Potential Vs capacity of some electrode materials.....	8
Figure 1.5	Phase diagram of V-O system.....	11
Figure 1.6	Layer structure of V_2O_5 as seen along the ac-plane.....	12
Figure 2.1	Schematic diagram of a typical spin-coating deposition technique.....	26
Figure 2.2	Schematic diagram of sol-gel technique.....	28
Figure 2.3	Bragg's diffraction of x-rays from different planes.....	32
Figure 2.4	A typical three electrode electrochemical cell.....	41
Figure 2.5	(a) Scanning Voltage and (b) Typical Voltammogram.....	42
Figure 2.6	A typical MIM capacitor structure.....	46
Figure 3.1	XRD spectra of V_2O_5 thin films; * = ITO peaks.....	59

Figure 3.2	Raman spectra of V ₂ O ₅ thin films.....	61
Figure 3.3	The arrangement of oxygen polyhedra in V ₂ O ₅ in (a) (ab) plane (b) the c direction. The oxygen atoms are represented as participating in bridges (a), chains (b) and vanadyl (c) bonds. Bond distances are given in nanometers.....	62
Figure 3.4	Raman spectra of three films, before annealing at 450°C. The peaks below 1000 cm ⁻¹ are from V ₂ O ₅ , distorted V ₂ O ₅ and V ₂ O ₅ .nH ₂ O.....	65
Figure 3.5	TEM micrographs of V ₂ O ₅ thin films: (a) VNA, (b) VOSG, (c) VISG; and HRTEM of (d) VNA, (e) VISG. The planar defects in (d) are highlighted with an arrow mark.....	67
Figure 3.6	Optical transmittance of the three films and ITO coated glass substrate and (b) the corresponding plots of (αhν) ^{2/3} vs. hν, the photon energy.....	68
Figure 3.7	Linear-sweep cyclic voltammograms at sweep rates 0.5, 1, 2, 5, 10, 15, and 30 mV/sec of (a) VNA, (b) VOSG, and (c) VISG. The sweep rate increases in the direction of the arrow.....	70
Figure 3.8	Cyclic voltammograms of the three films at the scan rate 2 mV/sec from 0 to 0.7 V. Inset: An enlarged portion of the CV of VOSG and VISG between 0 to 0.5 V.....	72

Figure 3.9	Randles-Sevcik plot (i_p vs. $\gamma^{1/2}$) for the two cathodic and anodic peaks for V_2O_5 thin films.....	75
Figure 4.1	XRD of V_2O_5 - TiO_2 thin films prepared using (a) sol-gel (b) metalorganic precursors; * = ITO peaks.....	83
Figure 4.2	Raman spectra of V_2O_5 - TiO_2 thin films prepared using (a) sol-gel (b) metalorganic precursors. The intensities of Raman spectra of SG70V30Ti and MO70V30Ti are multiplied by 3 times the actual value to observe the peaks clearly.....	86
Figure 4.3	Raman spectra of V_2O_5 - TiO_2 thin films prepared using (a) sol-gel (b) metalorganic precursors. The deconvoluted peak are also shown.....	88
Figure 4.4	TEM micrographs of V_2O_5 - TiO_2 thin films: (a) SG100V, (b) MO100V (c) SG95V5Ti and (d) MO95V5Ti.....	89
Figure 4.5	HRTEM micrographs of V_2O_5 - TiO_2 thin films: (a) SG100V, (b) MO100V (c) SG95V5Ti and (d) MO95V5Ti. Planar defects and faint and diffuse discontinuity in lattice fringes are marked by an arrow in the HRTWM of the films.....	90
Figure 4.6	Optical transmittance of V_2O_5 - TiO_2 films on ITO coated glass substrate prepared using (a) sol-gel (b) metalorganic precursors and (c) and (d) corresponding plots of $(\alpha h\nu)^{2/3}$ vs. $h\nu$, the photon energy for V_2O_5 - TiO_2 thin films and $(\alpha h\nu)^2$ vs. $h\nu$ for TiO_2 thin films.....	93

Figure 4.7	Linear-sweep cyclic voltammograms of V ₂ O ₅ -TiO ₂ thin films at sweep rates of 0.5, 1, 2, 5, 10, 15, and 30 mV/sec prepared using (a) sol-gel (b) metalorganic precursors	94
Figure 4.8	Cyclic voltammograms of V ₂ O ₅ -TiO ₂ thin films prepared using (a) sol-gel (b) metalorganic precursors at a scan rate of 2 mV/sec from -0.1 to 0.6 V. The arrow mark indicates the direction of voltage sweep.....	96
Figure 4.9	Variation in the lithium intercalation capacity of V ₂ O ₅ thin films prepared using sol gel and metalorganic precursors with respect Ti concentration.....	98
Figure 4.10	Randles-Sevcik plot (<i>i_p</i> vs. $\gamma^{1/2}$) for the peaks (a) pa1 and (b) pc2 of pure V ₂ O ₅ and 5%Ti incorporated V ₂ O ₅ thin films thin film.....	99
Figure 5.1	Variation in particle size with annealing temperature of the films.....	109
Figure 5.2	Cross-sectional images of (a) MODT (b) MOD75T and (c) SPDT films.....	109
Figure 5.3	Plots of (a) XRD and (b) Raman spectra of the MODT films annealed at different temperatures.....	111
Figure 5.4	J-E characteristic of MOD TiO ₂ films annealed at different temperatures.....	112

Figure 5.5	Frequency dependence of (a) dielectric constant and (b) loss tangent the films annealed at different temperatures.....	113
Figure 5.6	Plots of (a) XRD and (b) Raman spectra of Zr-doped films annealed at different temperature.....	114
Figure 5.7	EDAX image of a Zr-doped TiO ₂ film annealed at 950°C.....	115
Figure 5.8	J-E curve of 25% Zr-doped MOD films annealed at different temperatures.....	116
Figure 5.9	Frequency dependence of (a) dielectric constant (b) loss tangent of Zr-doped films annealed at different temperatures.....	117
Figure 5.10	Plots of (a) XRD and (b) Raman spectra of sputtered deposited films annealed at different temperatures.....	118
Figure 5.11	J-E characteristic of sputtered deposited films annealed at different temperatures.....	119
Figure 5.12	Frequency dependence of (a) dielectric loss and (b) loss tangent of sputtered deposited films annealed at different temperatures.....	120
Figure 5.13	J-E characteristic of MOD, MOD75T and SPDT films annealed at 950°C.....	121

Figure 5.14	Plots of (a) dielectric constant and (b) loss tangent as a function of frequency for MODT, MOD75T and SPDT films annealed at 950°C.....	121
Figure 5.15	Variation in dielectric breakdown field of the films with annealing temperatures within the region of measurement.....	122
Figure 5.16	Plots of $\ln J$ Vs $\ln E$ of three sets of films annealed at different temperatures.....	124
Figure 5.17	Plots of (J/E) Vs $E^{1/2}$ of three sets of films annealed at different temperatures.....	126
Figure 5.18	Cole-Cole plots of films annealed at 750°C	128
Figure 5.19	Real and imaginary dielectric constants for films annealed at 750°C, symbols (experimental) and solid lines (fitted).....	128

Chapter 1

INTRODUCTION

The cyclic stability and current density of V_2O_5 thin films critically depend on the degree of non-stoichiometry which depends on the amount of carbon contents in the precursor used. The proper amount of transition metal doping could lead to the optimal degree of non-stoichiometry for better cathodic performance. The better understanding of non-stoichiometry is crucial for the overall improvement in the performance of V_2O_5 thin film as a cathode material.

Dielectric constant and leakage current of TiO_2 thin film critically depend on the method of preparation and annealing temperature. Proper amount of transition metal doping can have number of implications such as phase stability, improvement in leakage current as well as stability in dielectric constant, which can lead to the finding of better high-k dielectric material for future gate dielectric and energy storage ceramic capacitor.

1.1 TRANSITION METAL OXIDES AS FUNCTIONAL MATERIALS

Transition metal oxides exhibit a wide range of electrical, optical, magnetic, electrochemical, semiconducting, photochemical, dielectric properties, making them interesting materials for varieties of applications to meet the ever increasing demands in the field of rapidly advancing science and technology. The occurrence of

extraordinarily varied chemical and physical properties of the transition metal oxides is a feature of the progressive filling of shells of d orbital across each series in periodic table [1]. The broad range of physical properties of transition metal oxide has spurred exploration of their potential use in a wide variety of applications, such as renewable energy sources [2], catalysis [3], smart materials [4], memory devices [5] to name a few. The properties of many transition metal oxide thin films can be drastically manipulated and even new properties can be created by engineering the microstructure and composition, which makes the studies of these materials ever challenging and exciting. The focus of this thesis is to study the structure-property correlation in thin films of V_2O_5 and TiO_2 based transition metal oxides as functional materials.

1.2 CATHODE MATERIALS FOR LITHIUM ION BATTERY TECHNOLOGY

Batteries are the power sources for almost all portable electronic devices, ranging from laptop computers to calculators, cellular phones to personal music players, and cameras to camcorders. Rapid technological advances have led to a remarkable miniaturization of these electronic devices. However, less progress has been made in advancing the technology of the batteries that power these devices. Among various rechargeable batteries, lithium based batteries are promising batteries for portable application. Lithium has high standard potential (-3.04V versus standard hydrogen electrode), small radius and it is also the lightest material. These two properties combined lead to high gravimetric and volumetric

capacity making it a candidate for high performance applications. Figure 1.1 shows the comparison of volumetric and gravimetric energy density of presently employed battery technologies.

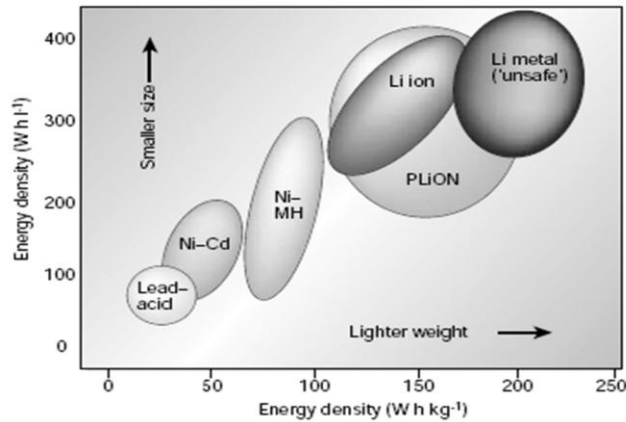


Figure 1.1 Volumetric and gravimetric energy density of different battery technologies [6]

Lithium battery technology appears to be the best in terms of both volumetric and gravimetric energy density. However, because of the safety issues, lithium ion batteries dominate the power sources for portable electronic industries worldwide. Lithium ion battery has many distinguished features, which make it superior over other traditional battery technologies.

- Highest operating voltage, 3.6 V, which is more than three times higher than the operating voltage of nickel cadmium, NiCd, and Nickel Metal Hydrate, NiMH, batteries
- Compact, light weight and superior specific energy density, more than 2 times higher than the energy density of other traditional batteries.

- Faster charging and discharging, attains above 90% of its full capacity within an hour.
- Higher discharge rate of up to 3C/s.
- Wider operating temperature range, 20 to 60°C.
- Very low self-discharging rate, less than 5% a month, comparing with other traditional batteries, NiCd and NiMH.
- Free from memory effects.
- Longer life cycle of up to 1000 cycles.
- Safer and free of pollution unlike other traditional batteries, which use toxic metals such as Pb, Cd, Hg etc.

LI-ION BATTERY

Similar to any other battery a lithium ion battery consists of one or more electrochemical cells, electrically connected in an appropriate series / parallel arrangement to provide the required operating voltage and current levels, including, if any, monitors, controls and other ancillary components. A cell is the basic electrochemical unit providing a source of electrical energy by direct conversion of chemical energy, and consists of electrodes, separators, electrolyte, container and terminals. Charging and discharging of the lithium ion battery is

related to the intercalation and deintercalation of lithium ions into a host matrix (see Fig. 1.2). As the host matrix is oxidized and reduced, ions are transported through the electrolyte causing the flow of electric current through the external circuit. When battery is in use Li^+ ions migrate through the electrolyte from anode to the cathode and integrate inside the lattice of the cathode, known as intercalation. As a result the electrons flow in the outer circuit and into the device to provide electrical energy to the device being used.

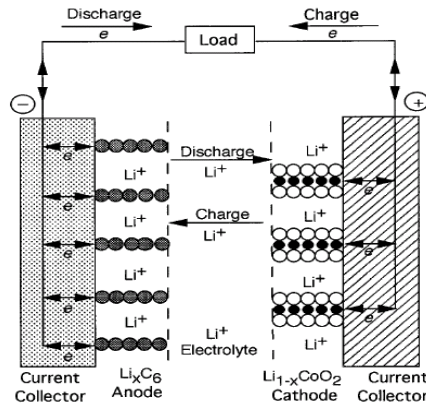


Figure 1.2 Charging and discharging process in a typical rechargeable lithium– ion battery [7]

The reverse process occurs during the charging of the battery, which is known as deintercalation of Li^+ ions from the host lattice. The development of lithium battery technologies allowing higher energy densities is related to the development of high capacity electrodes to provide a higher cell voltage V , which is related to the work functions of the anode (φ_a) and cathode (φ_b). The open circuit voltage of the cell (see Fig. 1.3) is related to the work functions as

$$V_{oc} = \frac{\varphi_c - \varphi_a}{ne} \quad (1.1)$$

where n is the number of electrons which transfer from the cathode to the anode and e is the charge of an electron.

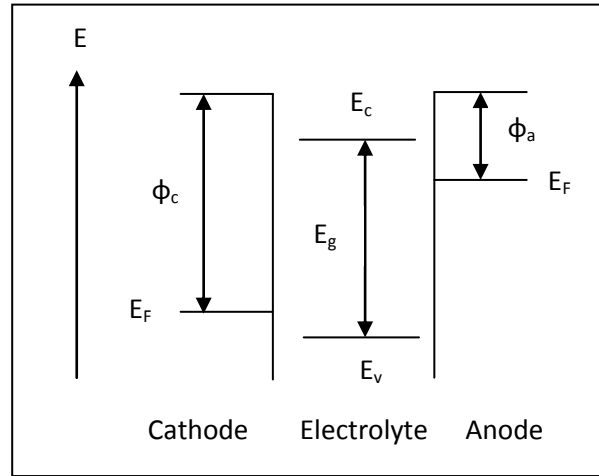


Figure 1.3 Open circuit diagram of a cell

For the transfer of lithium ions, V_{oc} is actually equivalent to the difference of lithium chemical potentials between cathode and anode. Therefore for the development of lithium ion battery technology, it is essential to understand the fundamental properties of constituting electrode material. At present, portable batteries are substantially more expensive than other widely used power sources. One of major costs in conventional Li-ion batteries is the use of a cobalt based oxide as the cathode material. Replacing Co-based cathodes with a different material could significantly lower the overall cost of Li-ion batteries.

1.2 CATHODE MATERIALS

For the better performance of a lithium ion cell, a good cathode material should possess the following properties.

- The structure of the cathode should be ideal to host as many numbers of lithium ions as possible. This depends on the number of sites in the host structure as well as the ability of the host material to access multiple oxidation-reduction states.
- The lithium intercalation/deintercalation inside the host matrix should be reversible with minimal or no change in the host structure.
- The host material should have good electronic and lithium ion conductivities to minimize the effect of cell polarization.
- The host material should not react with the electrolyte over the entire voltage range.
- The host material should be lightweight, cost effective, environmentally friendly and easily available.
- There should not be any unwanted oxidation/reduction of the electrolyte.
- The potential of the cell must lie within the stability window of the solvents and salts used.

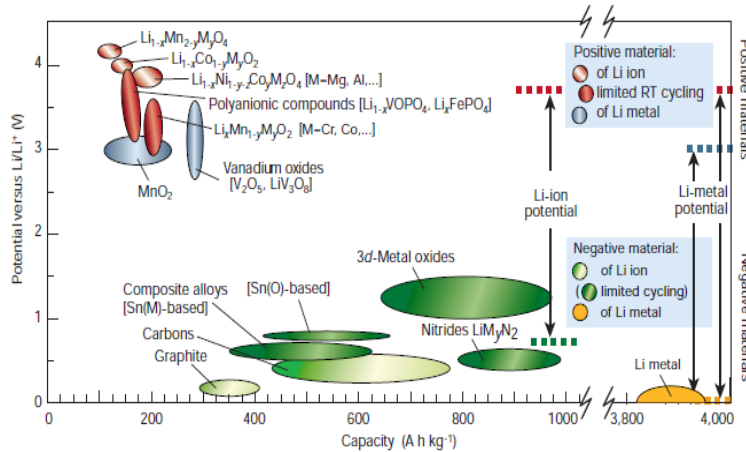


Figure 1.4 Potential Vs capacity of some electrode materials [6]

An overview of the different electrode materials, displaying their individual potential and capacity is shown in Fig. 1.4. LiCoO_2 based materials are currently used in LIBS, however, high cost, limited capacity, and narrow safety margin has led for search for alternative cathode electrode. Possible alternatives include oxides of manganese and iron such as LiMn_2O_4 [8] and LiFePO_4 [9] and LiMnO_2 [10]. LiMn_2O_4 is cheaper and less toxic but the reduced capacity at elevated temperatures is a problem. LiMn_2O_4 spinel and LiMnO_2 layered are the potential candidates to replace LiCoO_2 because they possess good electrochemical performance. The important fact is that manganese is less expensive, non-toxic and is abundant in nature. The situations encountered using manganese was the capacity fading at elevated temperatures due to dissolution of manganese in the form of Mn^{+2} [11]. In addition, the voltage is a two step complicated solid state reaction. To minimize the effect studies have been done on doping with heteroatoms such as Li [12], Al [13], Ti [14], Cr [15], Fe [16], Co [17], V [18] and Ni [18]. In

addition conductivity and cyclic stability were found to be improved by coating LiMn_2O_4 particles with LiCoO_2 because LiCoO_2 has higher conductivity and the dissolution of Mn^{+2} is suppressed due to the coating [16]. The coating with ZnO and $\text{LiAl}_x\text{Mn}_{1-x}\text{O}_4$ was also found to improve electrochemical performance significantly [19]. It has been shown that coating with $\text{LiAl}_x\text{Mn}_{2-x}\text{O}_4$ can significantly improve the electrochemical performance. Although LiMn_2O_4 is a promising cathode material with excellent electrochemical properties with some improvement to be done, its discharge is low due to inherent structure.

Layered LiMnO_2 appears to be a promising candidate because of its good electrochemical properties [19]. In addition it has very high theoretical value of capacity, almost double the capacity of LiMn_2O_4 [20]. But it suffers from structural change during charging/discharging and two plateaus appear at two different potentials, causing capacity fading [21]. The doping of Ni is found to improve structural stability and prevent capacity fading [22]. The addition of Ni also helps lower preparation temperature [23]. The doping of Li and both Li and Ni is also found to improve the electrochemical performance significantly [24]. Coating with Al_2O_3 , CoO or combinations of both in different proportions have shown to improve electrochemical performance [25].

LiFePO_4 is another good candidate material which has some good advantages such as longer cycle life of 2000 cycles and excellent thermal stability [26]. Iron is also less expensive, non-toxic and is abundant in nature. But compared to LiCoO_2 , it still has some major drawbacks such as lower specific capacity, premature failure in

discharging below 33%, capacity loss even at moderate discharge rates and poor electric conductivity [27]. Basically, its poor electric conductivity has been the main problem to use it in commercial production. Its conductivity can be improved by coating LiFePO_4 particles with carbon, metal and other metal oxides [28]. Addition of metals such as Cu, Ag etc is proved to improve capacity and cyclic stability [29].

1.3 V_2O_5 AS A CATHODE MATERIAL FOR Li-ION BATTERY

Vanadium is a transition metal which exists in different oxidation states from +2 to +5, with the possibility of forming many types of vanadium oxides such as VO, V_2O_3 , VO_2 and V_2O_5 determined mainly by the parameters temperature and pressure [30]. This ability of vanadium atoms to form stable multiple oxidation states provide the opportunity of conversion between oxides of different stoichiometry by reduction and oxidation of oxygen. In addition, series of intermediate states are known due to wide range of ordered and disordered defect structures [31]. These defect structures result in the wide range of stoichiometry of the cubic VO lattice and the existence of the two homologous series, the Magneli series, $\text{V}_n\text{O}_{2n-1}$ ($2 < n < 9$) [31], between V_2O_3 and VO_2 , and the Wadsley series [31], $\text{V}_n\text{O}_{2n+1}$ [31], between VO_2 and V_2O_5 . This gives the possibilities of forming vast numbers of vanadium oxides but only some of them are stable and known to exist depending on the temperature and partial pressure of oxygen as shown in the phase diagram (Fig. 1.5).

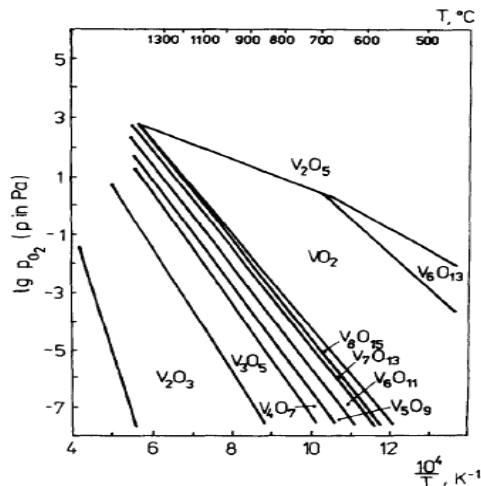


Figure 1.5 Phase diagram of V-O system [34]

The stability of the series V_nO_{2n+1} decreases with n increasing and is not known to exist beyond V_8O_{15} . It can be also inferred from the phase diagram that the stability range of V_nO_{2n+1} becomes narrower with n increasing and resulting these compounds to mix in narrow bands. Among various vanadium oxides, V_2O_5 is studied extensively, because of its promising applications in lithium ion batteries and catalysis. The ability of vanadium to possess multiple stable oxidation states results in the easy conversion between oxides of different stoichiometry by oxidation or reduction, leading to its extensive use as catalyst in selective oxidation. Therefore, the surface properties of V_2O_5 are of particular interest from heterogeneous catalysis point of view, since it is used as active catalysis for oxidation reactions of hydrocarbons [31].

Vanadium pentoxide belongs to P_{mmm} space group with unit cell parameters $a = 11.510 \text{ \AA}$, $b = 3.563 \text{ \AA}$, and $c = 4.369 \text{ \AA}$. The crystal structure of V_2O_5 is made of chains of corner-sharing and edge-sharing VO_6 octahedra. However, the octahedral

are irregular in V_2O_5 with five V–O distances ranging from 1.78 to 2.02 \AA and the sixth distance as large as 2.79 \AA . The structure is orthorhombic with the large separation along the crystallographic c direction. The one very large V–O distance makes the structure equivalent to the square pyramids of VO_5 , with five oxygen atoms surrounding the vanadium atom, with the layer separation of 4.4 \AA . This layered structure makes V_2O_5 well suited for inserting lithium ions into the structures (see Fig. 1.6). In this study, we have focused on structure-electrochemical property correlation in V_2O_5 thin film as a cathode material for lithium ion thin film batteries.

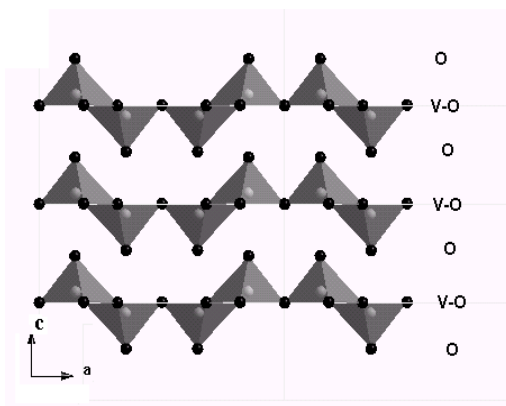


Figure 1.6 Layer structure of V_2O_5 as seen along the ac -plane [31]

Although a wide range of insertion-deinsertion materials have been synthesized and studied, no significant gains in capacity have been realized. One method for increasing the capacity is to insert more than one Li ion per transition metal, which is possible with vanadium based oxides. Vanadium forms several binary oxides. This is possible in the vanadium based oxides, since vanadium can exist in a range of oxidation states from $2+$ to $5+$. Vanadium pentoxide is described

from the packing of V_2O_5 layers along the c axis of the unit cell. Each layer is built up from VO_5 square pyramids sharing edges and corners with five V-O distances between 0.159 and 0.202 nm. The short and intermediate length bonds are mainly covalent and the long vanadyl bond is mainly ionic. During the electrochemical reaction of lithium with V_2O_5 , Li^+ intercalates between the layers and can be described by the following reversible redox reaction.



Lithiation leads to layer separation, corresponding to a widening of the vanadyl bond. The distance between the V_2O_5 layers play a major role in the electrochemical properties of V_2O_5 . Up to three Li^+ can be inserted as the vanadium oxide transforms through five different crystal structures, although some of insertions are irreversible. Due to its layered structure, which allows insertion of a large amount of lithium ions, vanadium pentoxide exhibits the most attractive specific capacity, the theoretical value being around 380 Ah/g in the potential window 3.8/1.5 V.

Other limitations associated with conventional lithium ion batteries are their larger size and safety concerns. In certain electronic devices the battery system comprises as much as half the total weight and volume. Liquid lithium cells also present safety hazards, due to the presence of volatile chemicals and excess heat production. Thin film batteries, which are still in the prototype stage, may offer a safer, more compact alternative to conventional lithium batteries. Unlike conventional batteries, thin film batteries can be deposited directly onto chips or

chip packages in any shape or size and, when fabricated on thin plastics, can be quite flexible. Some of the positive features of thin-film batteries include all solid state construction, a wide range of operating temperatures, versatility in size and shape, and they are significantly less hazardous. A thin film battery stack is less than 5 μm from current collector to anode. Depending on the choice of substrate and packaging, the total battery thickness ranges from 0.35 mm to 0.62 mm. Despite these advantages, it is necessary to develop a more complete understanding of thin-film batteries before they could replace conventional Li-ion batteries.

While vanadium oxide thin films have great potential as lithium intercalation cathodes, their use in commercial available batteries is limited for the following reasons:

1. A wide spectrum of electrochemical properties has been observed in V_2O_5 films, depending strongly on the preparation techniques used, including: vacuum evaporation [32], sputtering [33], pulsed laser deposition [34], chemical vapor deposition [35], and sol-gel processes. [36]
2. The Li capacity of V_2O_5 decreases over successive charging and discharging cycles. This decrease may arise from an increasing electrical resistance produced by ion trapping arising from slight structural distortion.
3. V_2O_5 also has low intrinsic electrical conductivity and diffusion coefficient. For intercalation electrodes, good ionic conductivity is required for fast ion migration during discharge and charge reactions.

Research on V_2O_5 thin films is mainly focused on understanding the influence of various physical properties on the electrochemical characteristics and to increase the electrical conductivity and diffusion coefficient, and to stabilize the structure during repeated charging and discharging. To improve the intercalation rate, specific capacity, and cycling performance, transition metal doped V_2O_5 , vanadium oxide bronzes such as $M_xV_2O_5$ ($M = Na, Ag, Cu, \text{etc.}$), and mixed phases of V_2O_5 and electrochemical active transition metal oxides such as TiO_2 and WO_3 have been considered as cathode materials. In doped V_2O_5 , the dopant elements (Fe, Cr, Tb, Ag, or Cu) are distributed homogeneously and increase the interactions between V_2O_5 layers. The dopants act like pillars between the vanadium oxide layers and thus stabilize the structure during intercalation and deintercalation, providing good cycling behavior. In addition, the dopants increase the interlayer distance, so more lithium ion can be inserted, and these pillars increase the diffusion rate of lithium ions in the materials, improving the kinetics of the charge and discharge reactions [37-40]. Some of the bronzes and vanadates are found to have better electrochemical properties than V_2O_5 . For example Coustier et al. investigated $Ag_xV_2O_5$ and $Cu_xV_2O_5$ bronzes as host materials for lithium-ion intercalation and demonstrated these electrode materials having high specific capacity, good cycle stability, and high electronic conductivity. However most of the initial research efforts have focused on polycrystalline powders. Only very recently has the research on the electrochemical properties of vanadium based oxides shifted towards thin films.

V₂O₅ THIN FILMS

The electrochemical characteristics of V₂O₅ thin films depend critically on the synthesis conditions, film thickness, microstructure, and composition. For example, the evolution of the crystal structure of Li_xV₂O₅ on Li⁺ intercalation depends on the crystallinity of the film and on the partial pressure of oxygen during sputtering [41-43]. Thickness of 2.5 μm, (*h00*) oriented DC sputtered V₂O₅ films exhibit a better electrochemical behavior in terms of rate capability and cycling properties than 800 nm thick (*h00*) and (*100*) oriented films [44]. While the intercalation capacity of V₂O₅ thin films depends on film thickness and orientation, the cyclic stability is driven by the film morphology [45-46]. The effect of film structure on the electrochemical properties can be traced to the fact that while defects and stoichiometry determine the distance between V₂O₅ layers, the film thickness and microstructure influence the lithium diffusion distance, which in turn affects the specific capacity and rates [47]. Therefore a better understanding of the influence of specific physical characteristics, including the defects, stoichiometry, and microstructure, on the electrochemical properties of V₂O₅ films will be important for optimizing these materials for electrode applications. Since composites and mixed phases can have different properties than their constituent phases, recent research on cathode materials has explored the electrochemical characteristics of composites and mixed phases. Composite films of vanadium-titanium oxides have been recognized as promising cathode materials.

1.4 HIGH-K DIELECTRIC MATERIALS

In semiconductor technology, conventional silicon dioxide, SiO_2 , is an important gate dielectric for metal oxide semiconductor field-effect transistor (MOSFETS) because of its outstanding electric and dielectric properties that meet all requirements for a gate dielectric [48]. It can be grown on Si substrate with excellent thickness control and uniformity as well as it forms a very thermodynamically stable interface on the substrate with very low interfacial defect density. It is thermally stable up to 1000 °C [49] required to fabricate MOSFETS. It has very high electronic bandgap of around 9 eV [50] with sufficient valence band and conduction band offsets. It has conduction and valence band offset of 3.1 eV and 4.8 eV respectively with silicon [51]. It has very high dielectric breakdown field of approx 13 MV/cm [52]. However dielectric constant of SiO_2 is very low around 3.9 [53] which is the main restriction to meet the demand of rapidly increasing semiconductor based technology.

There has been continuous shrinkage in the thickness of conventional SiO_2 based gate dielectrics in MOSFETS to increase the device performance as well the cost of manufacturing. However the reduction in thickness of conventional SiO_2 based gate dielectrics in MOSFETS below 1.2 nm brings a major problem [54]. Below this threshold thickness the leakage current increases exponentially with the decrease in thickness. This limitation demands other alternate materials to meet the performance and requirements of future gate dielectric as designed by the International Technology Roadmap for Semiconductors (ITRS). Another material, in

spite of its relatively low dielectric constant currently being used is silicon nitride and oxynitride, SiO_xN_y [55]. It has comparable performance of conventional SiO_2 but higher dielectric constant of about 6.9, almost double of the conventional SiO_2 dielectric. However, this material still has pretty low dielectric constant well below the scaling goal adopted by ITRS while keeping the tunneling leakage below the threshold limit of (10^{-6} A/cm²) at an lowest operating voltage of 1.1 V and a dielectric constant higher than 25.

One of the possible solutions is to replace the conventional SiO_2 dielectric by other materials with higher dielectric constants so that the equivalent or higher performance can be achieved with the thicker dielectrics. Many metal oxides with higher dielectric constant, known as high-k dielectrics such as Ta_2O_5 [56], TiO_2 [57], ZrO_2 [58], HfO_2 [59], Al_2O_3 [60], La_2O_3 [61] and other composites of these materials are being studied as potential candidates. The physical thickness of these materials could be kept large without any compromise in the performance. But these materials suffer from one or more problems such as higher leakage, lower breakdown etc and not yet ideal to fully replace conventional SiO_2 based gate dielectrics [62]. Further studies and modifications on these materials are necessary. The suitability of any new high-dielectric which can replace conventional SiO_2 based gate dielectric is determined on the basis of following requirements [63-64].

- The material should be in amorphous state to avoid grain boundary leakage. The film in its polycrystalline form possesses higher leakage due to grain boundary loss.

- The material should be an insulator with large bandgap of more than 5 eV and sufficient band offset with silicon. Generally increasing the dielectric constant leads to lower band offset for the material in contact with the silicon. There is also inverse relationship with the dielectric constant and the bandgap.
- Many studies have shown that there is inverse relationship with the film thickness and the interfacial layer quality and the charge carrier mobility.
- There should be lower interfacial trap density, D_{it} , of typically less than 10^{11} /cm²eV
- The material should be thermodynamically stable on silicon. The material should have a larger Gibb's free energy of formation to prevent reaction with silicon. Oxygen diffusion coefficient should be low to prevent the growth of large interfacial layer
- The material should possess good silicon/dielectric interface quality.

Hafnium Oxide, HfO₂, is one of the most promising materials because it is thermodynamically stable on Si and has very low leakage current [65]. It has reasonably high dielectric constant of 25 and relatively larger band gap energy of 5.68 eV [66]. However HfO₂ film presents a poor interface quality with Si, high oxygen diffusion rate through the film, causing a low-k interfacial layer growth, and a low crystallization temperature of around 400-450 °C [67] . To produce good interface quality an ultra-thin SiO₂ film is grown between both materials, producing

a high k/SiO_2 stack. The SiO_2 layer between the high- k film and the Si substrate reduces the equivalent dielectric constant. Some works report that nitrogen incorporation in HfO_2 (HfO_xN_y) produces a film with improved interface properties, suppressing impurity penetration, enhancing reliability and increasing the crystallization temperature of above $1000\text{ }^\circ\text{C}$ [68]. But HfO_xN_y possesses a relatively lower dielectric constant of approximately 13 [69]. Zirconium oxide, ZrO_2 , is another high- k dielectric material with average dielectric constant of 26. But ZrO_2 suffers from low crystallization of around $500\text{ }^\circ\text{C}$ and it has relatively high diffusivity with oxygen leading to the formation of low- k interfacial SiO_2 layer in the course of films deposition [70]. In addition incompatibility of ZrO_2 with the other materials used in the MOSFETS is also an important issue [70]. Aluminum oxide (Al_2O_3) can remain amorphous at temperature higher than $900\text{ }^\circ\text{C}$. Al_2O_3 has also very low leakage current density due to its large band-gap and band-offset of more than 2 eV with silicon [71]. But Al_2O_3 has relatively low dielectric constant of around 8 [71]. Tantalum-pentoxide (Ta_2O_5), with its intrinsic dielectric constant of 20-30, very low dielectric loss and high refractive index was initially considered as a promising high- k dielectric material [72]. But this material also suffers from some serious problems such as thermodynamically unstable when directly grown on silicon and it has very low band offset of 0.3 eV with silicon [72].

1.5 TiO₂ AS A HIGH-K DIELECTRIC MATERIAL

TiO₂ thin film possesses some unique properties for it to be used as a future high-k dielectric in MOS technology, because of high dielectric constant of around 60 [73] and its wide usage in memory capacitor applications. However, there are some issues which prevent TiO₂ to be used as a gate dielectric material in the present technology. It has lower electronic bandgap of 3.6 eV [74]. It starts to crystallize at very low temperature of 350°C [75]. It possesses two different phases: anatase and rutile with different values of dielectric constants and anatase is thermodynamically unstable. Furthermore, it has higher leakage and higher silicon/dielectric interface state density. If it is deposited onto Silicon and submitted to high temperatures it can segregate into a SiO₂ and forms metallic oxide (M_xO_x). Since these properties and performance depends on film quality and morphology as determined from different methods of preparation parameters and conditions, more investigations and modifications are necessary to get it realized as a future gate material.

TiO₂ in its pure form suffers from numbers of problems such as crystallization at lower annealing temperature of around 350 °C, depending on the preparation method, promoting higher leakage, formation of SiO₂ at the silicon-insulator interface with low dielectric constant, lower electronic bandgap and band offset with silicon, and low thermal instability. There are quite a few studies on Zr-doping in connection to its suitability as a high-k dielectric. A very few studies have shown that doping zirconium into TiO₂ at optimized concentration could help reduce

the leakage current by an order of magnitude [76]. Since ZrO_2 has high bandgap of 6 eV Zr-doping can shift the bandgap of TiO_2 to the higher value suitable for high-k requirement. Eventhough there are no reports of inhibition of crystalline form of TiO_2 with Zr-doping, it help reduce the high levels of defects on TiO_2 films and improves the film quality. The important change in the structural property due to Zr-doping above some optimal concentration is the stability of anatase phase which stabilizes the dielectric constant of TiO_2 [77] . Further the Zr doping help reduce the interface trap density as well as thermal stability with the Si substrate [78].

1.6 SCOPE OF THE THESIS

The electrochemical and dielectric properties are dramatically affected by the preparation methods, quality of the films, degree of crystallinity and morphology. So it is important to achieve the optimal performance parameters using different deposition and processing methods to improve the electrochemical and dielectric performance. This thesis mainly deals with: 1) Structural, morphological and electrochemical properties of V_2O_5 and Ti doped V_2O_5 thin films prepared using metalorganic deposition (MOD) and Sol-Gel methods. 2) Structural, morphological and dielectric properties of TiO_2 and Zr doped TiO_2 thin films prepared using metalorganic deposition (MOD) and sputter deposition and different annealing temperatures. Structure-property correlation studies have been carried out using structural characterization methods: X-ray diffraction (XRD), scanning electron

microscopy (SEM), Raman spectroscopy, transmission electron microscopy (TEM), UV/Visible spectroscopy and electrochemical property measurements using cyclic voltammetry and frequency dependent complex dielectric function and leakage characteristics.

Chapter 2

SYNTHESIS AND CHARACTERIZATION METHODS

2.1 SYNTHESIS METHODS

There are various thin film deposition methods used for preparing transition metal oxides including physical vapor deposition (PVD) [79], metal-organic vapor deposition (MOCVD) [80], plasma sputtered deposition (PSD) [81], atomic layer deposition (ALD) [82], molecular beam epitaxy (MBE) [83], sol-gel (SG) [84] etc. Large variations in film quality, morphology, crystallinity and performances are found depending on the preparation methods and conditions. Some methods like MBE and ALD produce high quality films but they are expensive as well as technically sophisticated for industrial production. Among many other thin film deposition techniques metalorganic decomposition (MOD) [85] is a quick, easy and cheaper way of preparing thin films for industrial applications. It doesn't require any technical sophistication such as high vacuum to prepare the films and recently, it has been extensively used in thin film processing due to the ease in the composition control, good homogeneity and uniform deposition over large surface area. MOD technique uses metal-organic precursors to prepare thin films by spin coating on any kind of substrate. Since organic precursor contains a large proportion of hydrocarbons, as deposited films requires high temperature baking or annealing to obtain the final oxide material. The quality of the films can be controlled by tuning the viscosity of the precursor solution, rate of temperature

increase/decrease during annealing, and using substrates of similar thermal expansion coefficients as that of the film being deposited.

METALORGANIC DECOMPOSITION (MOD)

Metalorganic decomposition is one of the easiest and simplest thin film preparation techniques using spin coating. Preparation of thin films from metalorganic decomposition technique involves three steps—precursor preparations, precursor coating on the substrate and decomposition by annealing at particular temperature for certain time. In the first step, precursor solution with proper viscosity is prepared by mixing the particular organic liquid with proper amount of organic solvent such as xylene, toluene or any other appropriate solvent. The homogeneity of the precursor can be achieved by using ultrasonic bath. A complex precursor of two or more oxides can be prepared by mixing the respective organic liquids in their proper atomic weight ratio. The precursor is then spin coated over a substrate using a spin coater.

A typical spin coating process is shown in Fig. 2.1. The substrate is cleaned in ultrasonic bath for 15 min. and then heated in the oven at 500 °C for about 2 minutes. Then the substrate is placed over the spinner in the spin coater. A few drops of precursor is dispensed over the substrate is spun at 500 °C rpm for 15 s. The spinning rate can be varied depending on the type of precursor and the thickness of the layer desired. The thickness and density of the layer depends on the

spinning rate. The microstructure of the film also may depend on the spinning rate.

The film is then baked in the furnace at 300 °C for 1.5 min.

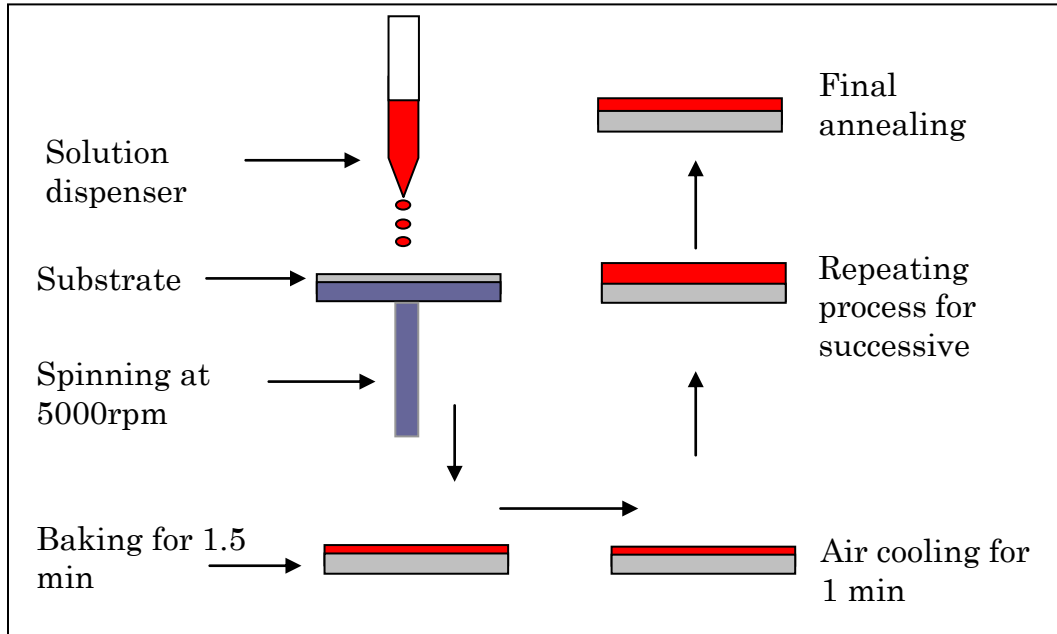


Figure 2.1 Schematic diagram of a typical spin-coating deposition technique

The process is repeated multiple times to get the desired thickness of the film. The third step is the decomposition of the film. In this step the film is annealed at 450 °C for 1 hr to remove the organic impurities in the film. Even though MOD is the cheapest and easiest method for preparing thin films; it has some drawbacks concerning the quality of the film. While removing organic impurities by heating at higher temperatures, the film is left with many cracks and defects. The film density and thickness is also not uniform because of the spinning of the particles at high spinning rates. It is also difficult to deposit the films if the optimal viscosity of the precursor is not found. The quality of the film

can be optimized by selecting the proper substrate, the spinning rate, viscosity or precursor. It has been reported in the literature that epitaxial film with very good quality can be prepared by mixing proper polymers with the precursor and adjusting the spinning rate.

SOL-GEL METHOD

The sol-gel method is another easier and cheaper non-vacuum technique that provides the perfect control over the morphology, crystal structure and chemical composition of the material and thus regarded as one of the versatile techniques to synthesize varieties of high quality materials in different form such as bulks, thin films, nanoparticles, nanotubes, nanorods etc. on varieties of substrates. This method has been used to prepare varieties of metal oxide thin films with different morphology and crystal structure for cathode materials. Based on this synthetic route, variations of precursors, solvents, ligands, different additions sequences of compounds and further treatment as well as other changes in sol-gel methods have been reported and widely applied in the preparation of, e.g., glasses, ceramics, inorganic fillers and coatings. The synthesis technique in sol-gel method (see Fig. 2.2 for a schematic) involves multiple steps in a sequence as (a) Initial Precursors (b) Hydrolysis (c) Monomer formation (d) Condensation (e) Sol formation and (f) Gelation. The preparation starts from the suitable precursor in a complex organic compound form. The first step involves the hydrolysis of the precursor. The

hydrolysis can be catalyzed by acid (most commonly by HCl or HNO₃), which increases the reaction rate. The second stage of the process is polycondensation of the hydrolysis products, which yields a 3D cross-linked network. The precursor sol can be deposited on a substrate to form a thin film in varieties forms such as aerogel, xerogel, dense film etc. It can be cast into a suitable container with the desired shape to obtain monolithic ceramics, glasses, fibers, membranes, aerosols etc. or can be used to synthesize powders like microspheres, nanospheres etc.

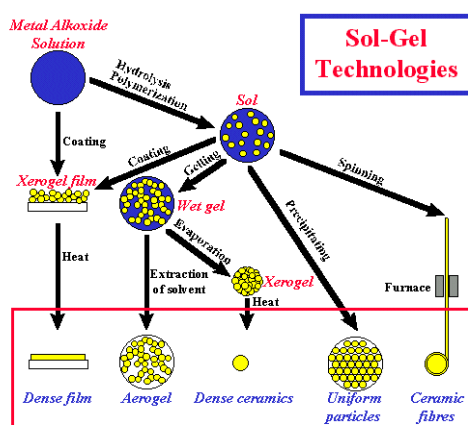


Figure 2.2 Schematic diagram of a sol–gel technique [86]

For the present research, we have prepared vanadium, Titanium and Ti-doped vanadium precursors for our thin film using sol-gel methods. The precursors were spin coated on ITO coated glass substrate using the steps as explained in the metalorganic synthesis method. Only difference is the films were baked at 100 °C for 1.5 min in the furnace during film preparation instead of backing at 300 °C for MOD precursors. The vanadium precursor was prepared using the sol–gel method reported elsewhere in the literature by controlled hydrolic polycondensation of

vanadium-triisopropoxide, $\text{VO}(\text{OC}_3\text{H}_7)_3$ in isopropanol, $\text{C}_3\text{H}_7\text{OH}$. The appropriate amount of $\text{VO}(\text{OC}_3\text{H}_7)_3$ was mixed with proper amount of isopropanol (1:6 in general) in an open beaker, stirred for 60 to 90 minutes and allowed to hydrolyze under the ambient humidity. The titanium precursor was prepared from 0.033 mol/l (0.2ml) acetic acid, catalyzed hydrolysis of acetylacetonone 0.028 mol/l (0.33g) and 0.028 mol/l (0.94g) of modified titanium (IV) tetraisopropoxide (99.995%) in isopropanol (14 ml) in argon atmosphere inside the glove box the vanadium precursor was prepared by dissolving 0.5g of V_2O_5 powder in 30 ml of 15% H_2O_2 and stirred for 5 minutes at 80 °C in water bath, producing a red-brown gel, which was re-dispersed in de-ionized water.

RF SPUTTER DEPOSITION

We have prepared TiO_2 films using RF magnetron sputtering process. This is a vacuum based deposition process in which the atoms from a target material are ejected by the bombardment of highly energetic ions and deposited onto the substrate. The target is connected to the negative terminal of RF source acting as a cathode and the substrate, facing the target, serves as the anode. There are two types of R. F sputtering systems: DC sputtering system or AC sputtering system. The disadvantages of DC sputtering system are very high positive charge buildup on the cathode (target) and very high voltage needed to sputter insulators. These

problems can be avoided in AC sputtering system in which the polarity of the target changes and sputtering only occurs when the target is negative.

The material to be sputtered is made into a target and mounted onto a circular copper backing plate. The target consists of a circular disk (2 or 3" diameter) of high purity (99.99 %) material. The anode in turn can be grounded, charged positively or negatively, heated, cooled or combination of one or more of these depending on the requirements of the condition of deposition. The chamber is evacuated to its lowest possible pressure on the order of $\sim 10^{-6}$ torr before the start of sputtering. To start sputtering, very little amount of sputtering gas particularly pure argon (Ar) is introduced into the evacuated chamber to a pressure $\sim 10^{-2}$ torr. The electric field applied to the cathode accelerates the residual electrons which collide with the Ar atoms and produces Ar^+ ions forming plasma. These positive ions are accelerated towards the cathode (target) and start to bombard it dislodging atoms from the target material.

In magnetron sputtering, crossed electric field and magnetic field are created. The negative potential on the target creates the electric field normal to it while the permanent magnet fixed on the back of the target produces a magnetic field parallel to the electric field. This combination of electric and magnetic field confine plasma in front of the target. A small magnetic field (20-200 mT) sufficient to influence only electrons is maintained which causes the electrons to move in a cycloid path leading to the very high ionization efficiency near the cathode. Only fewer electrons reach the substrate which in turns help reduce the substrate temperature. Some other

advantages of the magnetron sputtering system include low substrate temperature, high deposition rate, high thickness uniformity of the films etc. Reactive sputtering can be performed by introducing a little amount of oxygen gas into the argon. This can be varied depending on the type of the substrate and the sputtering temperature. This helps deposit films on their oxides form from the metal target.

2.2 CHARACTERIZATION METHODS

X-RAY DIFFRACTION

X-ray diffraction is a very powerful tool to identify what type of material it is, whether the material is in crystalline or amorphous phase, the degree of crystallinity, whether the material is pure or mixed with other impurities, whether the material has lattice defects etc. X-rays are the short wavelength electromagnetic waves with the wavelength range from 0.1 to 100 Å. For the typical material inter atomic distance ranges from 1 to 3 Å. For the diffraction of the electromagnetic waves from the crystal from the different crystal lattices the wavelength of the X-ray should be comparable to the inter-planner distance. When a beam of monochromatic x-rays with the wavelength the wavelength comparable to the inter-planner distance coming with an angle θ with the lattice plane collide with atoms in the different lattice planes they are diffracted from the lattices. For a give set of lattice planes (see Fig. 2.3 for a schematic), the diffraction peak appear when it satisfies the following Bragg's condition

$$2d_{hkl} \sin \theta = n\lambda_{hkl} \quad (2.1)$$

where d is the distance between two consecutive lattice planes, λ is the wavelength of the x-rays and n is the integer which identifies the order of diffraction. The diffraction from two consecutive planes is the first order diffraction, $n=1$. The integers h , k , and l are known as Miller indices whose values identify the set of particular planes. For example $h=k=l=1$ identifies the (111) set of planes.

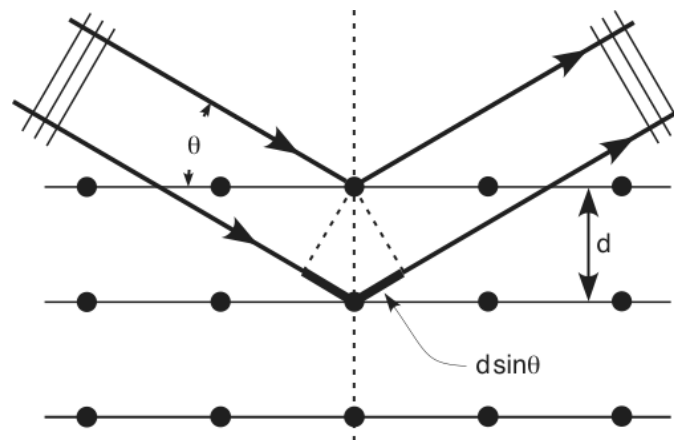


Figure 2.3 Bragg's diffraction of x-rays from different planes [87]

The particular material that is to be analyzed under XRD is exposed to a continuous beam of monochromatic x-rays and all the possible interference data are collected and analyzed. A series of continuous spectrum arising as a result of Bragg's diffraction is called x-rays diffraction pattern of the particular material. Depending on the structure of the crystal only a few allowed peaks due to the result of constructive interference from different planes are formed. This XRD pattern is a

hallmark of the particular crystal structure, thus the identification of the particular material. In addition a lot of other very important information can be collected from the XRD pattern. The highest relative intensity peak provides the information about the preferred crystal growth planes. The sharpness of the peaks provides the degree of crystallinity of the material as well as the crystallite size of the material. If the size of the crystallite is in nanometer range the peaks are seen broad. The grain size (D) of the material can be calculated using the Debye-Scherrer's full-width half maximum relation [88]

$$D = \frac{0.9\lambda}{FWHM(\text{radian}) \cdot \cos \theta_{hkl}} \quad (2.2)$$

The XRD data of many internationally known structures are stored as JCPDF power diffraction files which are available in all commercial x-ray diffractometer and can be compared to XRD pattern of the structure of interest. For our research XRD measurements of our samples were done using Rikagu X-Ray Diffractometer, which is the central instrumental facility located in the chemistry department of Wayne State University. The XRD patterns of the samples were collected using CuK_α radiation in θ - 2θ mode.

RAMAN SPECTROSCOPY

When incident photons collide with the atoms or molecules in the materials there are three possibilities- the photons are completely absorbed, photons are

scattered without change in energy or photons are scattered with their energy partially absorbed. If the photons are completely absorbed and re-emitted the phenomenon is called fluorescence in which the electrons jump from lower energy state to higher energy state and back. If the photons are scattered elastically the scattering is called Raleigh Scattering. If the scattered photons have energy higher or lower than the energy of the incident photons, due to exchange of energy with the molecule depending on the nature of excitation of its vibrational modes, the phenomenon is called Raman scattering. If the molecules of the material gain energy from the photons then the scattered photons have less energy which is called Stokes-Raman, while if the molecules of the material lose energy to the photons then scattered photons have high energy which is called anti-Stokes Raman. Raman scattering is intrinsically a weak process (1 in 10 million photons) and furthermore, Raman activity depends on the polarizability of the molecules. A Raman spectrum is the plot of the intensity of the scattered radiation versus the Raman shift, where Raman shift is the difference in energy between the incident photon and scattered photons and can be calculated as [89]

$$\bar{\nu}(cm^{-1}) = \frac{1}{\lambda_{incident}} - \frac{1}{\lambda_{scattered}} \quad (2.3)$$

Raman spectroscopy is a very effective and reliable method of investigating structure of the material as well as qualitative and quantitative component of the impurities. In solids, the incident photons are scattered by phonons (lattice

vibrations) which are characteristic of the material. In our research, Raman spectra of the samples were collected using green excitation line at 514.5 nm (2.41 eV) from an Ar-ion laser in the back-scattering geometry using a Renishaw 1000 Raman Microscope.

UV/VIS SPECTROSCOPY

UV/Vis spectrum consists of a small portion of the whole electromagnetic spectrum ranging from 190 – 900 nm. Since the human visual is approximately 400 – 750 nm, UV-Vis spectroscopy is a very useful tool to characterize the optical, electrical, electronic and structural properties of various technologically important materials such as pigments, coatings, windows and filters on the basis of amount of UV/VIS light absorbed, transmitted, and reflected. When electromagnetic waves interact with the materials some portion of it is reflected, some portion is absorbed and some is transmitted, depending on the frequency of electromagnetic wave and the structure of materials. The energy of the electromagnetic waves is calculated using $E = h\nu$, where h is the Planck's constant and ν is the frequency of the electromagnetic waves. Since most of the oxide materials have band gap energy in the range of energy of the UV/VIS spectrum, UV/VIS spectrometry is the very important to study the optical properties of the materials. When the energy of the electromagnetic waves is comparable to the band gap of the material then it is

completely absorbed by the material. This means the electrons in the valence band of the material are excited to the conduction band.

UV/VIS spectroscopy is also very useful to calculate many important parameters such as refractive index, dielectric constant, thickness of the film and the energy band of semiconductor and insulator thin films. We studied the optical properties such as transmittance, reflectance, and absorption and calculated the energy band gap of the vanadium pentoxide and Ti-doped vanadium pentoxide thin films for electrochemical studies using a Lambda 900 UV/VIS/IR spectrometer located in the Engineering Department of Wayne State University. The transmittance spectra of the thin films are obtained by plotting the transmittance intensity in percentage versus wavelength of the UV/VIS radiation. The band gap energy can be roughly estimated by noting the wavelength at which the electromagnetic waves are completely absorbed. When electromagnetic radiation in the UV/VIS range is directed into the materials under study such as thin films and other organic compounds, the absorption of the electromagnetic radiation is of exponential nature. The change in intensity of the electromagnetic radiation through the transparent material can be estimated using Beer-Lambert Law.

$$I = I_0 e^{-\alpha(\lambda)d} \quad (2.4)$$

where I is the intensity of the transmitted electromagnetic wave passed through the sample, I_0 is the intensity of the incident wave into the sample, α is the coefficient of absorption and d is the thickness of the material. The equation can be simplified as

$$\frac{1}{d} \log \left(\frac{I_0}{I} \right) = \alpha(\lambda) \quad (2.5)$$

$$\frac{1}{d} \log T = \alpha(\lambda) \quad (2.6)$$

$$\text{Or} \quad \frac{I}{I_0} = A = \frac{1}{T} \quad (2.7)$$

where A is the absorption and T is the transmittance of the UV/Vis radiation through the sample. The value of energy of the UV/VIS radiation can be calculated using the relation

$$E = h \frac{c}{\lambda} \quad (2.8)$$

where h is the Plank's constant and λ is the wavelength of the electromagnetic radiation. For the group of materials with direct band gap, the band gap energy can be calculated using the relation [90]

$$(h\nu\alpha)^2 = A(h\nu - E_g) \quad (2.9)$$

$$\text{Or} \quad \alpha(\lambda) = A \frac{(h\nu - E_g)^{1/2}}{h\nu} \quad (2.10)$$

where A is the constant and its value depends on the transition probability. In the plot of $(h\nu\alpha)^2$ versus E, the value of E at $(h\nu\alpha)^2=0$, gives the value of band gap energy E_g . The general formula to calculate the band gap energy of any material can be expressed as follows [90]

$$\alpha(\lambda) = A \frac{(E - E_g)^m}{h\nu} \quad (2.11)$$

where $m = 2, 1/2, 3$ and $3/2$ for indirect allowed, direct allowed, indirect forbidden and direct forbidden transitions. So for indirect allowed transition,

$$\sqrt{\alpha h\nu} = A(E - E_g) \quad (2.12)$$

The extrapolation of the line at $\sqrt{\alpha h\nu} = 0$ in the plot of $\sqrt{\alpha h\nu}$ versus E is the value of indirect band gap energy in the case of the materials with indirect allowed band gap energy.

SCANNING ELECTRON MICROSCOPY

Scanning Electron Microscopy (SEM) uses a beam of electrons to obtain topographical image of a specimen as well as its elemental composition. It is a scanning technique where a beam of electrons is focused on the specimen and the resulting secondary electrons (emitted by the sample) or backscattered electrons are collected to form an image. The incident electrons undergo two types of scatterings- elastic scattering and inelastic scattering. The types of signals used by SEM include secondary electrons, backscattered electrons and characteristic x-rays. When a specimen is bombarded with electrons some electrons lose energy to excite the electrons in the specimen to the higher unstable states. The excited electrons move

towards the surface and escape the surface if they have energy enough to overcome the work function of the specimen. The production of secondary electrons is topographically dependent due to the low energy of the secondary electrons. Thus only those secondary electrons within few nanometers can escape the surface of the specimen and can be examined. Secondary electrons form the low energy but highest intensity spectrum. Secondary electron imaging produces high-resolution images of a sample surface to a few nanometers in size. Back scattered electrons are high energy electrons that are reflected or backscattered from the specimen by elastic scattering. The intensity of signal from the backscattered electrons depends on the atomic number of the elements present in the specimen. Since elements with higher intensity backscatter more efficiently and look brighter, backscattered images can provide information about the distributions of different elements in a specimen. Thickness of the thin film samples can be examined in cross-sectional SEM because the substrate and the film have different image contrasts, depending on the atomic number of the substrate and the thin film.

During the bombardment of the specimen with the beam of electrons, characteristic X-rays are generated by the elements of the specimen. The EDS (Energy Dispersive Spectrum) X-ray detector can measure the intensity of the x-rays versus the energy. This can provide qualitative measurement of the quantity of different elements present in the specimen. We used a Hitachi S-2400 SEM in the chemistry department to study topography, morphology and elemental analysis for

our V_2O_5 and Ti-doped V_2O_5 thin films. The films were gold-coated for conductivity using a coater available in the same laboratory.

TRANSMISSION ELECTRON MICROSCOPY

Transmission electron microscopy (TEM) is an imaging technique in which a beam of electrons is transmitted through a very thin specimen under study and its image is collected by an imaging device like florescent screen or photographic plate or CCD camera. TEM works on the same basic principles as the optical microscope but uses a beam of electrons and magnetic lenses instead to focus the electron beams. Since the resolution of the image is of the order of the wavelength, the resolution power of TEM is thousand times higher than the resolution power of optical microscope because the wavelength of electrons is thousands times shorter than the wavelength of the visible light. Using powerful TEM it is possible to resolve the image up to the order of a few angstroms which makes it possible to study the small details of biological cells or any other materials down to the atomic level. In materials research TEM is an indispensable tool to study morphological features such as size, shape and arrangement of the particles and crystallographic information such as arrangements of atoms in the material, degree of order and planar defects. There are two basic modes of imaging techniques in TEM-bright field imaging and dark field imaging. In bright field imaging all Bragg reflected beams are excluded through the objective aperture and only beams directly passing through the specimen are collected into the detector. This mode determines the mass-thickness contrast of the specimen. Since thick areas with heavy atoms

scatter more electrons the image appears with dark contrast and interpreting the image can be difficult. In Dark field imaging mode, all unscattered beams are excluded and scattered beams are collected to form the image. Thus the field around the specimen is generally dark. Dark field imaging is a very powerful technique to study the microstructure, crystal defects and atomic imaging. The dark field imaging is free of artifacts due to the nature of imaging process. Since the specimen needs to be illuminated very strongly to get the clear image, the specimen can be damaged, depending on the nature of the specimen. We used a JOEL-2010 TEM to study our thin films.

2.3 ELECTROCHEMICAL PROPERTY MEASUREMENTS

Cyclic Voltammetry (CV) a versatile electroanalytical technique in which a linearly varying voltage is applied between the working electrode and reference electrode and the faradic current is measured between counter electrode and working electrode.

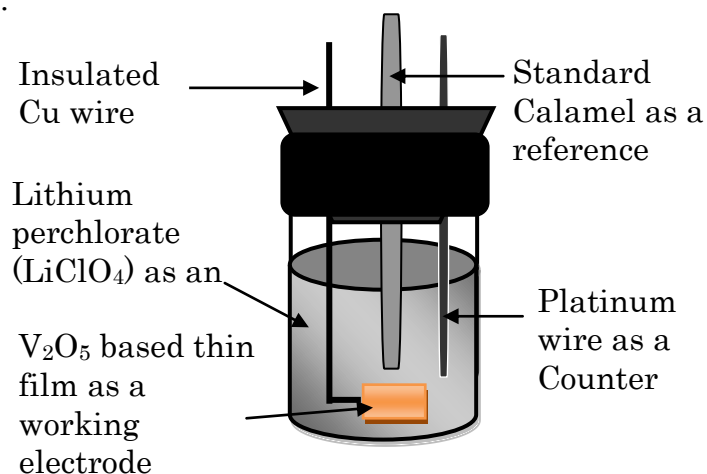


Figure 2.4 A typical three electrode electrochemical cell

Figure 2.4 shows the schematic of a three electrode electrochemical cell. Cyclic voltammetry is used to study the potential stability window of the materials and to determine the rate of controlling process. A closed loop is obtained when the current is scanned between two cut-off values of the voltage as shown in schematic in Fig. 2.5.

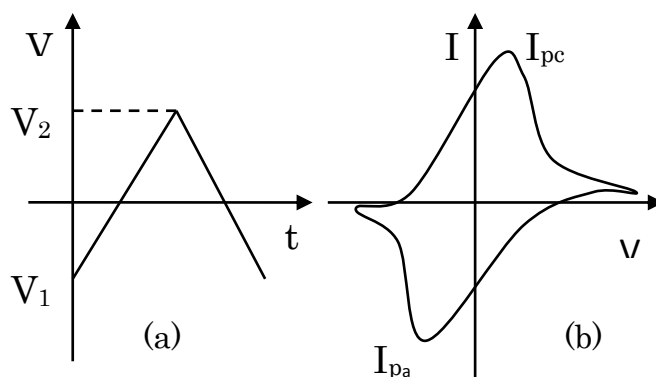


Figure 2.5 (a) Scanning Voltage and (b) Typical Voltammogram

A redox reaction can be expressed as [13]



where O and R represent the oxidized and reduced species respectively and n is number of electrons involved in the reaction. For the forward sweep, the potential (E) at any time during the scan can be expressed as

$$E = E_i + vt \quad (2.14)$$

where E_i represents the initial scanning potential, v is the scan rate and t is the time. Similarly for the reversed sweep,

$$E = E_i - vt \quad (2.15)$$

At the start of the measurement, when the redox potential is lower than the bulk potential, there is no redox reaction. Above the redox potential, the current starts to increase exponentially in the positive or negative direction (reduced or oxidized) reaching its maximum value, I_{pa} . As the sample is reduced or oxidized, concentration gradients develop and diffusion occurs. At the peak anodic or cathodic current, the redox potential is sufficiently positive or negative so that the species reaching the electrode surface is immediately oxidized or reduced. Beyond this maximum value, the current depends on the rate of mass transfer to the electrode surface and starts to decay as $t^{1/2}$. If the redox system remains in equilibrium throughout the scan, the electrochemical reaction is reversible. Some of the important features of a reversible reaction are:

- Cathodic peak current, I_{pc} , and anodic peak current, I_{pa} , are equal
 - The peak potentials, E_{pc} and E_{pa} , are independent of scan rate
 - The voltage separation, ΔE , between the two current peaks is equal to $59mV/n$
- [13]

$$\Delta E = \frac{2.3RT}{nF} = \frac{59mV}{n} \quad (2.16)$$

- The peak currents are proportional to the square root of the scan rate

$$I_{pa}(I_{pc}) \propto \sqrt{v} \quad (2.17)$$

- E^0 is positioned midway between two peak voltages, E_{pc} and E_{pa}

$$E = E^0 + \frac{RT}{nF} \ln \left[\frac{C_o}{C_R} \right] \quad (2.18)$$

$$E^0 = \frac{E_{pc} + E_{pa}}{2} \quad (2.19)$$

For a reversible redox reaction, the relation between applied potential difference (E) and concentration is given by Nernst equilibrium equation [91]

where C_o and C_R represent surface concentration of oxidized and reduced species respectively. Under these condition conditions, the peak current I_p is given by the Randles Sevcik equation [91].

$$I_p = 2.69 \times 10^5 n^{3/2} AD^{1/2} v^{1/2} C_0 \quad (2.20)$$

where A is the electrode area, n is the number of electrons involved, D is the diffusion coefficient. The electrochemical properties of thin films were studied using cyclic voltammogram (CV) using a three electrode cells. Cyclic voltammograms (CV) were recorded at different scan rates from 0.5mV/s to 30mV/s. A three electrodes electrochemical cell was prepared using 1 mol/L solution of lithium perchlorate (99.99% Aldrich) in propylene carbonate (99.97%) as an electrolyte, a platinum wire as a counter electrode, a standard calomel as a reference electrode and a thin film as working electrode. The cyclic voltammetry measurements were carried out using a Gamry PCI4/300 potentiostat/galvanostat.

2.4 DIELECTRIC PROPERTY MEASUREMENTS

In order to measure dielectric properties of oxide thin films, a MIM (metal-insulator-metal) sandwich capacitor structure (schematically shown in Fig 2.6) was fabricated. Approximately 1 mm diameter gold dots with an average thickness of ~ 100 nm were deposited using a mask over the film surface using a gold sputter (Effa Coater) unit available in the SEM laboratory at WSU Central Instrumentation Facility. The MIM structure was gold/ thin film/highly conducting n-type (*100*) silicon substrate. Contacts to electrodes were made using 0.1 mm diameter gold wires with silver paste, making sure that the latter material stays within the gold dot.

Two types measurements were performed on the films: 1) I-V characteristics of the films using the LC Precision meter (Radiant Technologies) with a maximum bias ranging from – 10 V to + 10V, 2) Capacitance versus frequency (100 Hz - 1M Hz) using HP LCR meter. Capacitance data is used to calculate complex dielectric function, $\varepsilon(f) = \varepsilon_r' + \varepsilon_r''$. Oxide films being insulators, the analysis of I-V (leakage) characteristics can provide an understanding on conduction mechanisms in the films as well as break down voltage (dielectric strength). On the other hand, analysis of $\varepsilon(f)$ data yields dielectric parameters like ε_0 (static dielectric constant), ε_∞ (high frequency dielectric constant), dielectric relaxation time, etc.

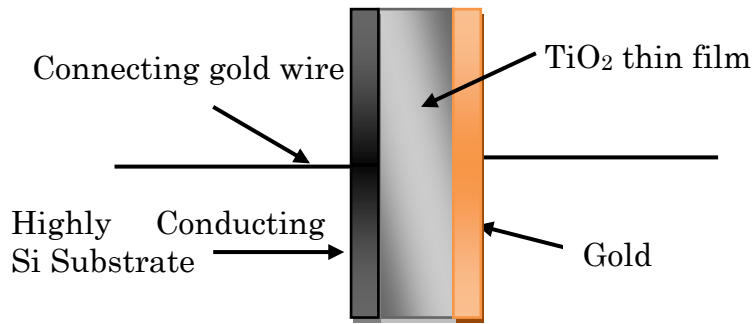


Figure 2.6 A typical MIM capacitor structure

2.5 ANALYSIS OF I-V CHARACTERISTICS

The structural and stoichiometric quality of oxide thin films and their correlation with material properties are very important for any practical application. For example, highly insulating stoichiometric oxide thin films are used as dielectric barriers in gated electronics. The stoichiometry of oxide thin films affects dielectric response and thus corresponding device performance. In order to understand the effect of stoichiometry and structural defects in TiO_2 thin films, we measured current-voltage (I-V) characteristics of a number of TiO_2 thin films fabricated using different growth methods and post growth heat treatments. Several workers [87-88] have studied I-V characteristics to analyze the various types of conduction mechanisms such as Schottky emission, Poole-Frankel emission, space-charge limited conduction etc., within the wide range of electric field with respect to film morphology, crystallinity, doping etc., which critically depend on many factors such as film preparation conditions, preparation methods and

experimental ambient conditions. The conduction mechanism in oxide thin films is mainly governed by the grain boundary defect states [89-90] and other native defects and their concentration depending on many conditions as stated before. Thus the defect states which effectively act as either trapping or recombination centers play an important role in determination of conduction mechanism in oxide films deposited under different growth conditions.

2.6 CONDUCTION MECHANISMS IN DIELECTRIC FILMS

The leakage current has been an important concern in the fabrication of microelectronic devices because of continuous shrinkage of devices into the nanoscale range. Without a better knowledge of leakage phenomenon due to different conduction mechanisms, the leakage current cannot be controlled. There are various conduction mechanisms that contribute to the overall leakage in the dielectric media under the influence of an electric field. The major types of conduction mechanisms in dielectrics are: (a) Schottky emission (b) Direct or Fowler-Nordheim tunneling (c) Poole-Frenkel conduction (d) Space Charge limited currents. We have studied these conduction mechanisms in our films in the form of metal-insulator-metal (MIM) sandwich capacitor structures of Gold-TiO₂ or Zr-doped TiO₂- highly conducting n-type silicon, in an applied dc field. The physics of various types of dominant phenomena are discussed below.

SCHOTTKY EMISSION (SE)

The Schottky barrier height is the difference of energy required to cross the electrons through the barrier between the metal and semiconductor or insulator interface. The electrons cross the junction if they get energy either from the thermal process or from the applied electric field which lowers the barrier height. The SE process is an electrode limited conduction which strongly depends on the nature of barrier between the metal/semiconductor and the insulator. SE is a non-ohmic rectification process. Not all the junctions act as rectifiers. The magnitude of current density in Schottky emission depends on number of factors and is expressed by the following relation [92]

$$J = AT^2 \exp\left\{-\frac{1}{kT}(q\phi - \beta_{SE}\sqrt{E})\right\} \quad (2.21)$$

where A is a constant ϕ is the Schottky barrier height, q is the electronic charge, E is the external electric field, k is the Boltzmann constant and T is the temperature.

The constant β_{SE} is given by

$$\beta_{SE} = \sqrt{\frac{q^3}{4\pi\epsilon_0\epsilon_r}} \quad (2.22)$$

where ϵ_0 is the permittivity of the free space and ϵ_r is the dynamic dielectric constant of the material. If Schottky conduction mechanism is a dominant phenomenon, a plot of $\ln(J/T^2)$ Vs $1/kT$ at some particular value of E should produce a straight line with negative slope which is related to the Schottky barrier

height Φ , an important parameter for MIS devices. In terms of J and E , if other parameters are assumed constant, the plot of J Vs \sqrt{E} should produce a straight line with positive slope. We have analyzed Schottky emission of our films at lower and higher electric fields at room temperature.

DIRECT OR FOWLER-NORDHEIM TUNNELING

Field emission or Fowler-Nordheim tunneling is a type of emission process whereby electrons tunnel through a triangular barrier by quantum tunneling in the presence of a high electric field. This quantum mechanical tunneling process is a dominant and an important mechanism for thin barriers as those in metal-semiconductor junctions when the film thickness is < 5 nm. The tunneling current increases exponentially when film thickness is < 2 nm. The charge carriers in Fowler-Nordheim tunneling do not get through the whole insulator but tunnel through the triangular barrier. The current density in Fowler-Nordheim tunneling depends on several parameters and is expressed as [93],

$$J = AE^2 \exp\left(-\frac{B}{E}\right) \quad (2.23)$$

where,

$$A = \frac{m}{m^*} \frac{q^3}{8\pi h \phi_B}$$

$$B = \frac{8\pi}{3} \left(\frac{2m^*}{h^2} \right)^{1/2} \frac{\phi_B^{3/2}}{q}$$

E , m , m^* and ϕ_B are electric field, electron mass, effective mass and the barrier height. The other parameter remaining constants, a plot of $\ln(J/E^2)$ Vs $1/E$ should generate a straight line with a negative slope equal to $-B$, from where the value of barrier height can be calculated. Since thickness of the films we studied were 200nm or higher, we can rule out the possibility of dominance by Fowler-Nordheim tunneling in our films. The other aspect is in higher electric field where Fowler-Nordheim tunneling can occur even in thicker films and can be a dominant phenomenon if the films are perfectly crystalline and free of defects. Since our methods of film preparation generates lots of defects in the films, we believe that Fowler-Nordheim tunneling should be insignificant compared to other types of conduction phenomena such as Poole-Frenkel emission and Space Charge Limited Current. Because of these factors we did not do the Fowler-Nordheim tunneling analysis in our samples.

POOLE-FRENKEL (PF) EMISSION

Poole-Frenkel effect is the localized emission of the charge carriers from the columbic trapping centers in the bulk of semiconductors due to thermal energy or the externally applied electric field. Due to this addition of external energy the charge carriers are ejected from the trapping centers to the conduction band and move through the crystal before falling into the nearest columbic traps. This type of transportation of carriers in solid is the Poole-Frenkel conduction and is one of the

dominant current conduction mechanisms specifically in the region of higher electric fields. The external electric field decreases the barrier height, increasing the conductivity which is dependent on the magnitude of electric field. The current density in the Poole-Frenkel mechanism is expressed as [92, 94]:

$$J = CE \exp \left\{ -\frac{1}{\xi kT} (q\phi_B - \beta_{PF} \sqrt{E}) \right\} \quad (2.24)$$

where, ϕ_B is the ionization potential in eV, which is the amount of energy required for the trapped electron to overcome the influence of the trapping center when no field is applied, $\beta_{PF} \sqrt{E}$ is the amount by which trap barrier height is reduced by the external electric field E, C is the proportionality constant and k is the Boltzmann constant. The coefficient ξ is introduced in order to consider the influence of the trapping or acceptor centers with its value $1 < \xi < 2$. The Poole-Frenkel β_{PF} is given by

$$\beta_{PF} = \sqrt{\frac{q^3}{\pi \epsilon_0 \epsilon_r}} \quad (2.25)$$

where ϵ_0 is the permittivity of the free space and ϵ_r is the dielectric constant of the insulator. The $\ln(J/E)$ Vs $E^{1/2}$ plot, also known as Poole-Frenkel plot, should be nearly linear if the Poole-Frenkel mechanism is the dominating conduction mechanism for polycrystalline insulating thin films whereas for amorphous thin films $\ln(J/E^{1/2})$ Vs $E^{1/2}$ should show a linear dependence.

SPACE CHARGE LIMITED CURRENT (SCLC)

The charge accumulation at the interface of electrode and insulator due to the excess carriers creates an internal electric field, which starts to oppose the applied electric field and thus total electric field near the electrode decreases, which prevents the further injection of carriers from electrode into the insulator. The most common space charge limited current density and voltage relationship due to discrete trap distribution is given by [95]

$$J = \frac{9\varepsilon\mu V^2}{8d^3} \quad (2.26)$$

where V is the applied voltage, d is the film thickness, ε is the dielectric permittivity and μ is the mobility of charge carriers. The $\ln(J)$ Vs $\ln(V)$ curves will be linear for discrete trap distribution with slope 2, and greater than 2 for exponential trap distribution. The discrete trap levels correspond to the certain type of impurities in the system whereas uniform trap distribution corresponds to the structural disorder present in the thin film.

2.7 ANALYSIS OF $\varepsilon(f)$ DATA

Many theoretical models have been used to explain the observed experimental data of dielectric constant of many materials as a function of

frequency. The earliest model used to explain the dielectric relaxation was described by Debye and is represented as [96]

$$\varepsilon^*(\omega) = \varepsilon'(\omega) - i\varepsilon''(\omega) = \varepsilon_\infty + \frac{\varepsilon_s - \varepsilon_\infty}{1 + i\omega\tau} \quad (2.27)$$

where, ε^* is the complex dielectric constant with real and imaginary components ε' and ε'' , ε_s is the static (DC) dielectric constant, ε_∞ is the high frequency dielectric constant, ω is the angular frequency and τ is the relaxation time. The model works well in explaining theoretical permittivity of polar liquids and other materials with a single relaxation time τ , which is one of the constants needed to fit the experimental data using the Debye equation. Often the ε' and ε'' are written (from Eq. 2.27) as

$$\varepsilon'(\omega) = \varepsilon_\infty + \frac{\varepsilon_s - \varepsilon_\infty}{1 + \omega^2\tau^2} \quad (2.28)$$

$$\varepsilon''(\omega) = \frac{(\varepsilon_s - \varepsilon_\infty)\omega\tau}{1 + \omega^2\tau^2} \quad (2.29)$$

A plot of ε'' versus ε' (Cole-Cole plot) results in a semicircle with center on the ε' axis and intersecting this axis at $\varepsilon' = \varepsilon_s$ and $\varepsilon' = \varepsilon_\infty$. The values of ε' and ε'' are determined using τ as a fitting parameter.

Only a few materials exhibit a single relaxation time that is described with the Debye equation. Many other empirical models have been proposed to explain the frequency dependent behavior of materials with more than one relaxation times or a distribution of relaxation times. The first empirical expressions for $\varepsilon^*(\omega)$

proposed by K.S. Cole and R.H. Cole in 1951 (J. Chem. Phys. **9**, 345,1941) is as follows:

$$\varepsilon^*(\omega) = \varepsilon_\infty + \frac{(\varepsilon_s - \varepsilon_\infty)}{1 + (i\omega\tau)^{1-\alpha}} \quad (2.30)$$

where, α is the relaxation width or the distribution parameter. In principle, ε_0 and ε_∞ can be experimentally measured and the other two parameters τ and α are used as fitting parameters to best fit the experimental data. However, in most of the cases, ε_0 and ε_∞ cannot be obtained directly from the experimental data since it is difficult to perform the measurements at very low and very high frequencies and to detect the saturated values in the two limits. There are methods to calculate numerically the values of ε_0 and ε_∞ from the available experimental measurements in the limited frequency region and thus obtain the other two parameters τ and α .

Many relaxation phenomena which are more complex involve more than one type of relaxation as well as high frequency relaxation, such as relaxation in polymer molecules etc., can be modeled using more complex empirical relations developed by Cole-Davidson [97] and Havriliak-Negami [98] and are expressed, respectively, as:

$$\varepsilon^*(\omega) = \varepsilon_\infty + \frac{(\varepsilon_s - \varepsilon_\infty)}{(1 + i\omega\tau)^\beta} \quad (2.31)$$

$$\varepsilon^*(\omega) = \varepsilon_\infty + \frac{(\varepsilon_s - \varepsilon_\infty)}{\left[1 + (i\omega\tau)^{1-\alpha}\right]^\beta} \quad (2.31)$$

where β is the distribution parameter that leads to asymmetric distribution of ε . The values of both α and β lie between zero and 1. It can be seen from the above relation these relation reduce to Debye and Cole-Davidson relations depending on the values of arbitrary parameters α and β .

Chapter 3

ELECTROCHEMICAL PROPERTIES OF V_2O_5 THIN FILMS

WHY INVESTIGATE V_2O_5 THIN FILMS?

Recently, V_2O_5 has received much attention as a promising material for applications such as catalysis [99-100], gas sensors [101], window material for solar cells, electrochemical devices [102], as well as cathode material for solid-state batteries [103]. The layered structure, together with the presence of multiple oxidation states of vanadium, makes V_2O_5 a potential candidate for cathode material in lithium ion micro-batteries. Up to three Li^+ ions can be inserted while going through five different crystal structures, even though some of insertions are irreversible [104-105]. A wide range of electrochemical properties are observed in V_2O_5 thin films prepared by different techniques including: vacuum evaporation [106], sputter deposition [107-110], thermal oxidation [111-112], pulsed laser deposition [113], chemical vapor deposition [114-116], and sol-gel processes [117]. These differences arise because the electrochemical characteristics of V_2O_5 thin films depend critically on the synthesis conditions, film thickness, microstructure, and composition. For example, the $Li_xV_2O_5$ crystal structure evolution upon Li^+ intercalation depends on the crystallinity of the film and on the partial pressure of oxygen during sputtering [109,118]. While the intercalation capacity of V_2O_5 thin films depends on film thickness and orientation and ranges from 12mC/cm^2 to 45mC/cm^2 , the cyclic stability is driven by the film morphology [119-121]. One of the

main concerns with utilizing V_2O_5 thin films for cathodes is the low capacity of lithium intercalation at high discharge rates due to its small diffusion coefficient of Li^+ with $D \approx 10^{-12} \text{ cm}^2/\text{s}$. The capacity at high discharge rates can be improved by controlling the size and shape of the particles and the morphology of the films. Nanostructure electrodes offer larger capacities than thin film electrodes, because of the shorter Li^+ diffusion length and larger surface area. However, nanostructure electrodes degrade after only a few charging and discharging cycles [122-124]. Another route to increase the intercalation capacity at higher discharge rates is to increase the diffusion coefficient. It may be possible to tune the diffusion constant by varying the inter-planar distance, either by doping or by creating oxygen vacancies. A better understanding of the influence of variations in the stoichiometry on the electrochemical properties of V_2O_5 will be important for optimizing the properties of these materials for electrode applications.

Due to different oxidation states available to vanadium, V_2O_5 can accommodate a large nonstoichiometry with oxygen vacancies as the basic point defects [125]. Consequently, small changes in the synthesis conditions can lead to significant deviations in the V_2O_5 stoichiometry directly influencing the electrochemical properties. V_2O_5 thin films for electrochemical applications are generally prepared by spin coating due to its versatility, and cost effectiveness for a large scale production. Vanadium oxide gels prepared from aqueous solutions or from alkoxide precursors are used in preparing films by spin or dip coating [118]. An alternative technique to prepare the gel is to dissolve V_2O_5 powder with H_2O_2

leading to peroxovanadate sol [119]. Recently, films have also been prepared using metalorganic decomposition by spin coating technique (MOD) [126]. In the present research, the effect of small deviations from stoichiometry on the electrochemical properties has been investigated, including the intercalation capacity and Li^+ diffusion coefficient in V_2O_5 thin film electrodes.

3.1 PREPARATION OF V_2O_5 THIN FILMS

V_2O_5 thin films were deposited on indium tin oxide (ITO) coated glass substrates (resistivity $10\Omega/\square$], visible transmittance $>80\%$) by spin coating using three different precursors: (i) A metalorganic (MO) precursor–vanadium naphthenate oxide 35% in naphthenic acid (vanadium = 2.8 to 3.2%) was ultrasonically mixed with small amounts of xylene and propanol to provide the proper viscosity. Naphthenic acid is a complex of carboxylic acids and has a high carbon to vanadium ratio (ii) An organic sol-gel precursor prepared by controlled hydrolytic polycondensation of vanadium-tri(isopropoxide) oxide $[\text{VO}(\text{OC}_3\text{H}_7)_3]$ in isopropanol $[\text{C}_3\text{H}_7\text{OH}]$. Typically, 3ml of $\text{VO}(\text{OC}_3\text{H}_7)_3$ was mixed with 30 ml of isopropanol in an open beaker, stirred for 90 minutes, allowed to hydrolyze under the ambient humidity. (iii) An inorganic sol-gel precursor–prepared by dissolving 0.5g of V_2O_5 powder in 30 ml of 15% H_2O_2 and stirred for 5 minutes at 80°C in water bath, producing a red-brown gel, which was redispersed in deionized water. While the sol-gel organic precursor has 12:1 carbon to vanadium ratio, the sol-gel inorganic precursor does not have any carbon. The final annealing was done at

450°C in ambient conditions for 60 minutes. The film thickness was ~300nm as measured by a step profilometer. In the following, the films prepared by MO, sol-gel organic and inorganic precursors are designated as VNA, VOSG, and VISG, respectively.

3.2 STRUCTURAL CHARACTERIZATION OF V_2O_5 THIN FILMS

The XRD patterns of VNA, VOSG, and VISG samples with the intensity plotted on a log scale are shown in Fig. 3.1. All the three films are monophasic and comprised of V_2O_5 within the detection limit of XRD.

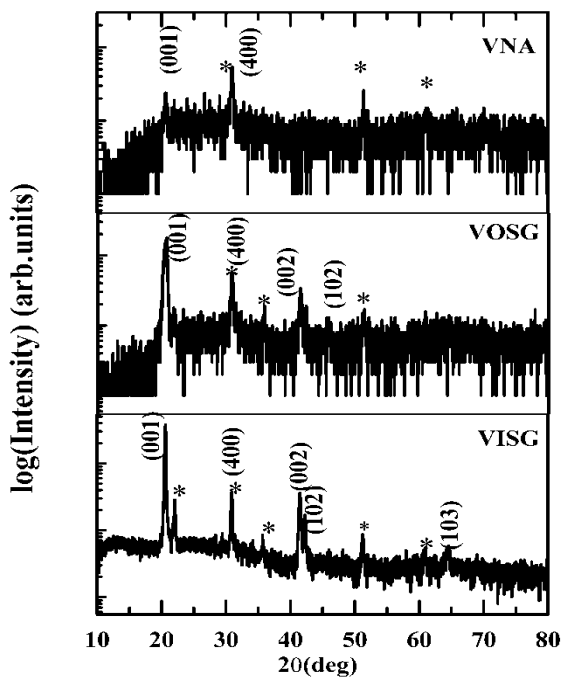


Figure 3.1 XRD spectra of V_2O_5 thin films; * = ITO peaks

The peaks are indexed according to the standard pattern [JCPDS file no.41-1426] for polycrystalline, orthorhombic V_2O_5 . Even though the peak intensities in the XRD pattern of VNA is smaller compared to VOSG and VISG, we do not observe peaks corresponding to any vanadium oxide other than V_2O_5 . Specifically, the XRD data suggest that there are no secondary vanadium oxide phases. This observation is consistent with what is known about the synthesis of V:O complex; since the films are annealed under ambient conditions, the formation of V_2O_5 is favored compared to other oxides. The higher intensity of the $(00l)$ peaks, compared to the other (hkl) reflections, suggests the preference for V_2O_5 to grow along $(00l)$ in these films. Even though the $(00l)$ peak is the strongest in a polycrystalline XRD powder pattern of V_2O_5 , the intensity ratios $(I_{(00l)}/I_{(hkl)})$ in the sol-gel prepared films is larger than in polycrystalline V_2O_5 , indicating a strong $(00l)$ texture. This preferred orientation in the sol-gel films can be understood from the properties of the starting material. The gel is formed by the hydrolysis and condensation of molecular precursors. The chemical control of these reactions allows the formation of vanadium pentoxide gels directly from the solutions at lower temperature than by standard solid state process [126-128]. Therefore, the sol-gel films are comprised of $V_2O_5 \cdot nH_2O$ [129], before annealing at 450°C. They have a V_2O_5 layered structure with trapped water molecules and are characterized by a strong structural anisotropy.

Annealing the sol-gel films for one hour at 450 °C leads to highly crystalline and textured films. In the MOD samples the V_2O_5 phase is formed by direct decomposition of metalorganic precursor at 450 °C, without the formation of an

Each layer in vanadium pentoxide is built up from VO_5 square pyramids (see Fig. 1.6 and 3.3a) sharing edges to form $(\text{V}_2\text{O}_4)_n$ zigzag double chains along $[010]$ and cross linked along $[100]$ by corner sharing [133]. Thus in each layer V is five-fold coordinated; with three V-O bonds involving three fold coordinated oxygen (O_c) belonging to $(\text{V}_2\text{O}_4)_n$ chains, one V-O bond involving two fold coordinated oxygen(O_B) constituting bridges between two chains and one involving vanadyl oxygen(O_v). The elementary structural unit is shown in Fig. 3.3 (b), which also designates the various oxygen atoms and bond length. The short and intermediate length bonds are mainly covalent, whereas the long vanadyl bond is mainly ionic. The successive layers are kept together by an equal number of weak Van der Waals bonds and much stronger double bonds [135]

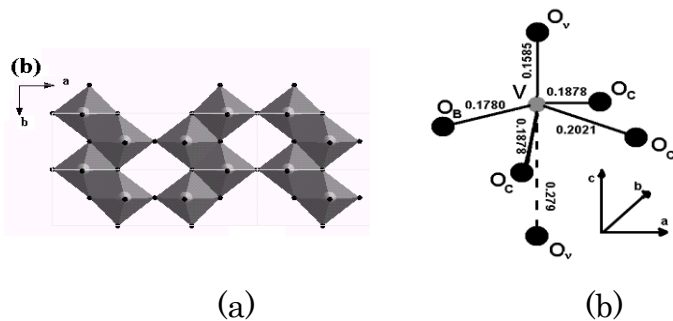


Figure 3.3 The arrangement of oxygen polyhedra in V_2O_5 in (a) (ab) plane (b) the c direction. The oxygen atoms are represented as participating in bridges (a), chains (b) and vanadyl (c) bonds. Bond distances are given in nanometers

The external modes can be considered as relative motions of the units with respect to each other, *i.e.*, translations and librations. These vibrations occur at low frequencies because each unit is considerably heavier than the constituent atoms

while the restoring force has the same order of magnitude. The external low-frequency Raman modes at 104, 142 and 194 cm^{-1} correspond to the relative motions of V_2O_5 layers with respect to each other [131]. The intensity of the peak at ~ 104 is very small compared to the peak intensity of 144 cm^{-1} and the signal is buried in the base of 144 cm^{-1} peak. The two peaks at 144 and 194 cm^{-1} are strongly associated with the layered structure and only appear when there is long range structural order. The presence of these low frequency modes in all three samples suggests that all the films have a layered structure and are well crystallized. The films grow preferentially with c -axis oriented perpendicular to the substrate plane [132]. Internal modes, which are observed in the high frequency region, are assigned to different stretching and bending of V-O bonds (Fig. 3.3) [132]. The high frequency Raman peak at 1000 cm^{-1} corresponds to vanadyl oxygen stretching mode ($\text{V}=\text{O}_\text{V}$). The second peak at ~ 700 cm^{-1} is assigned to the doubly coordinated oxygen ($\text{V}_2\text{-O}_\text{B}$) stretching mode which results from corner shared oxygen common to two pyramids. The third peak at ~ 530 cm^{-1} is assigned to the triply coordinated oxygen ($\text{V}_3\text{-O}_\text{C}$) stretching mode which results from edged-shared oxygen atoms in common to three pyramids. The two peaks located at ~ 406 and ~ 283 cm^{-1} are assigned to the bending vibration of the $\text{V}=\text{O}_\text{V}$ bonds. The peaks located at ~ 480 and ~ 303 cm^{-1} are assigned to the bending vibrations of the bridging $\text{V-O}_\text{B}\text{-V}$ (doubly coordinated oxygen), and the triply coordinated oxygen ($\text{V}_3\text{-O}_\text{C}$) bonds, respectively. It is generally believed that oxygen vacancies are the basic point defects in the V_2O_5 lattice and the vacancies are created by removing O_V with some of the V^{5+} reduced to V^{4+} for charge

balance. The exact $V^{5+}=O$ bond length depends on the V_2O_5 stoichiometry, thus the $V^{5+}=O$ stretching frequency ($\nu_{V=O}$), located at $\sim 1000\text{ cm}^{-1}$ in a stoichiometric crystal, can be used to determine even small deviations from stoichiometry. The frequency shift to lower values of this mode is due to a softening of the $V^{5+}=O$ bond in oxygen-deficient V_2O_5 films. The $\nu_{V=O}$ peak position is 999, 995, 993 cm^{-1} for VISG, VOSG and VNA, respectively. The estimated uncertainty in the peak position is $< 1\text{ cm}^{-1}$. These measurements show that the deviation from the stoichiometry increases from VISG to VOSG to VNA. However, the deviation from stoichiometry in VNA is not sufficient to degrade the film quality. This can be seen by comparing the intensity of peak near 932 cm^{-1} which corresponds to $V^{4+}=O$ and presence of sharp peak at 993 cm^{-1} corresponding to $V^{5+}=O$. Lee *et al.* [131] have found that with large deviations from stoichiometric V_2O_5 the intensity of the 932 cm^{-1} is larger than the peak at 993 cm^{-1} . With increasing nonstoichiometry the ratio of the intensity of 932 cm^{-1} and 993 cm^{-1} peak increases and with further increase in nonstoichiometry the peak at 993 cm^{-1} disappears [131]. Another probe for evaluating the degree of disorder in the films is the presence of the band at 830-840 cm^{-1} that corresponds to an infrared active mode [130]. This bond is normally Raman inactive because of the V_2O_5 symmetry but becomes active within a structurally disordered or non-stoichiometric film. The absence of the band at 830-840 cm^{-1} in VNA, VOSG, VISG confirms the high quality and near stoichiometry of the films. The small variations observed in the stoichiometry are related to the carbon content of each precursor. As mentioned earlier, the MOD precursor has a larger carbon concentration than the sol-gel

precursors. Therefore, after baking at 300 °C for one minute, the film consists of hydrocarbons together with the V_2O_5 . Similarly, VOSG films, after baking at 100 °C, contain very small amount of hydrocarbon, while VISG contains no carbonaceous component, since it is prepared using an inorganic precursor. It is known that the selective oxidation of hydrocarbons at vanadium oxide surfaces proceed by a redox mechanism, in which the hydrocarbon molecule interacts with the oxide surface losing hydrogen atoms and extracting a surface oxygen atom. Oxygen vacancies are generated at the surface and migrate into the bulk, and an equivalent number of vanadium cations are reduced [136]. When annealed at 450 °C these samples will be reduced to different extent depending on the concentration of hydrocarbons, leading to different degrees of nonstoichiometry. The observation of broad Raman bands at $\sim 1575 \text{ cm}^{-1}$ and 1370 cm^{-1} in the VNA sample before annealing confirm the presence of hydrocarbons (see Fig. 3.4 film, VNA).

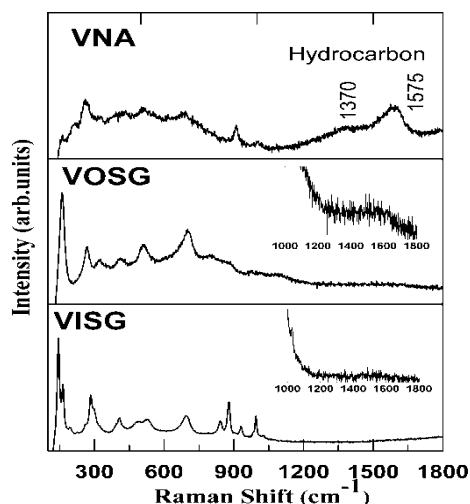


Figure 3.4 Raman spectra of three films, before annealing at 450 °C. The peaks below 1000 cm^{-1} are from V_2O_5 , distorted V_2O_5 and $V_2O_5 \cdot nH_2O$ [134]

The intensity of these peaks is considerably reduced in pre-annealed VOSG sample, and these peaks are absent in the pre-annealed VISG sample. This can be seen in the corresponding insets of VOSG and VISG showing enlarged Raman spectra from 1000 to 1800 cm^{-1} . The relative intensity of these peaks provides a direct estimation of the concentration of hydrocarbons present in the as-prepared samples. The concentration depends on the carbon content in the precursor-the higher the carbon content in the precursor results in higher hydrocarbon content in the as-prepared films. Pre-annealed VNA has the highest hydrocarbon content, while the VISG sample is formed using inorganic precursors and does not have the peak at 1500 cm^{-1} . Even though the presence of hydrocarbons in the pre-annealed samples has reduced the films, this does not lead to the formation of lower oxides of vanadium, as shown by the Raman studies. The presence of high intensity, sharp peaks at 144 and $\sim 1000 \text{ cm}^{-1}$ indicates that the films are crystalline, and have preferred orientation along $(00l)$. It is known that only monophasic vanadium oxides grow with strong texture on an amorphous substrate, except in cases where the two phases have very similar structure [39-40]. This, rules out the presence of all vanadium oxides other than V_2O_5 in these strongly textured films, except for V_6O_{13} . However, we observe none of the Raman peaks corresponding to V_6O_{13} in the spectra of VNA, VOSG, and VISG.

The TEM micrographs of VNA, VOSG, VISG, and HRTEM of VNA and VISG are shown in Fig. 3.5a-c, Fig. 3.5d, e, respectively. From the micrographs, we determined that the crystallite size is smaller in VNA and VOSG as compared to

VISG, even though all the samples are well crystallized. VNA and VOSG have a particle size distribution of 100 to 300 nm, whereas VISG is comprised of large particles with a diameter of $\sim 1.5\mu\text{m}$. The presence of oxygen vacancies inferred from the Raman spectra is corroborated by the observation of defects in HRTEM of VNA (Fig. 3.5d), which are absent in stoichiometric VISG (Fig. 3.5e).

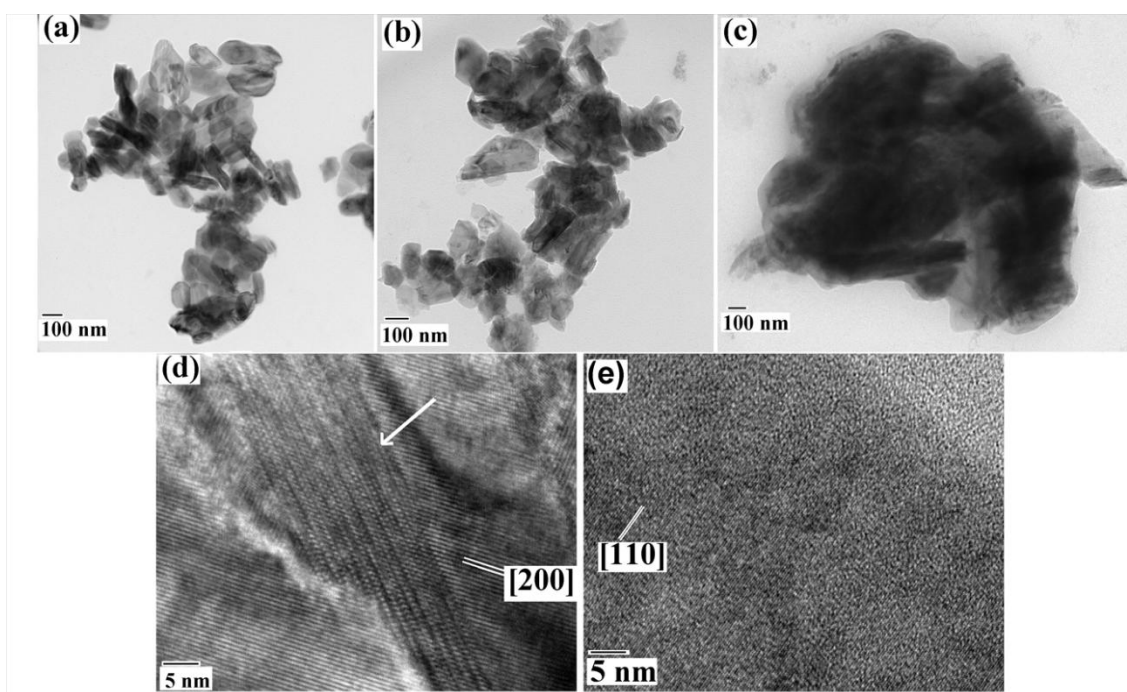


Figure 3.5 TEM micrographs of V_2O_5 thin films: (a) VNA, (b) VOSG, (c) VISG; and HRTEM of (d) VNA, (e) VISG. The planar defects in (d) are highlighted with an arrow mark [134]

The transmittance spectra of V_2O_5 thin films are shown in Fig. 3.6a. The decrease in transmission below 600 nm is associated with the fundamental absorption edge. The fundamental absorption edge shows a red shift with increasing concentration of oxygen vacancy, which corresponds to a shift in the optical band

gap to lower energy. The optical absorption coefficient α of the films is calculated using the relation $\alpha t = \ln(1/T)$ where T is the transmittance and t is the film thickness. Figure 3.6b shows the plots of $(\alpha h\nu)^{2/3}$ versus $h\nu$ for the three V_2O_5 thin film samples. The optical band gaps, which were evaluated by extrapolating the linear plots to $(\alpha h\nu)^{2/3}$ equal to zero, are 1.7, 2.2, and 2.5 eV for VNA, VOSG, and VISG films, respectively.

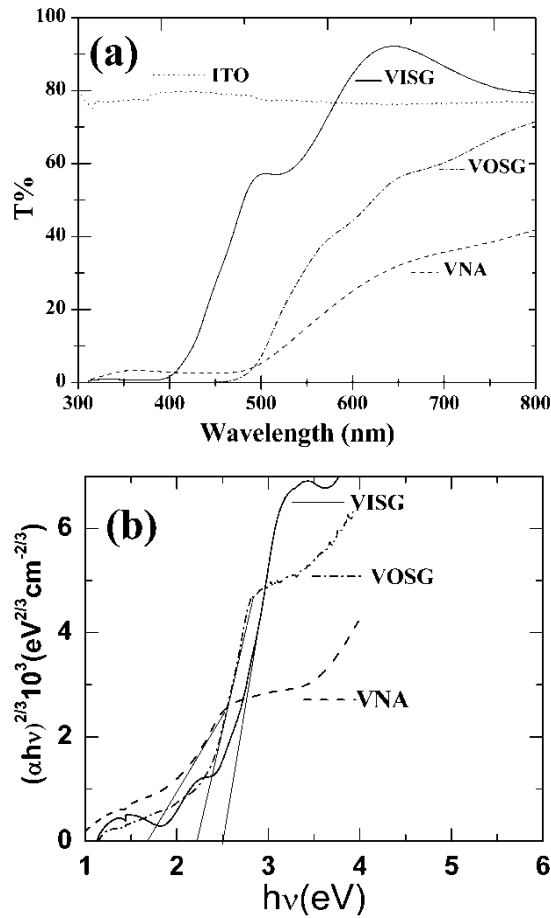


Figure 3.6 Optical transmittance of the three films and ITO coated glass substrate and (b) the corresponding plots of $(\alpha h\nu)^{2/3}$ vs. $h\nu$, the photon energy [134]

This suggests a direct forbidden transition across the energy band gap of the material, which is in good agreement with recent reports on V_2O_5 thin films prepared by sputter deposition [118]. Generally, the conduction band in V_2O_5 is formed by vanadium $3d$ bands and the valence band is formed by $2p$ bands of oxygen, which is a direct forbidden transition. In nonstoichiometric films, the empty $3d$ orbital of vanadium adjacent to a vacancy are able to localize excess electrons [138-140]. This leads to the formation of localized states in the gap, which decreases the band gap energy. From our Raman and UV-VIS studies, we argue that VNA films are more nonstoichiometric, than VISG and VOSG samples. Among sol-gel films VISG has the smallest deviations from stoichiometry.

3.3 ELECTROCHEMICAL CHARACTERIZATION OF V_2O_5 THIN FILMS

To study the electrochemical characteristics of V_2O_5 thin films, we carried out cyclic voltammetry measurements of these three films [141]. This technique is useful for determining the charge capacity of the film and reversibility of the charge exchange. Figure 3.7 shows linear-sweep cyclic voltammograms (CV), *i.e.* the plot of current versus applied voltage for the V_2O_5 thin films at sweep rates from 0.5 to 30 mV/sec. CV of the freshly prepared electrochemical cell is carried out at several different scan rates in the following order: 2, 1, 0.5, 5, 10, 20, 30 mV/Sec. The first cycle is carried out at a scan rate of 2mV/sec. The shape of the curves is consistent

with a typical diffusion controlled CV of a reversible lithium intercalation/deintercalation process.

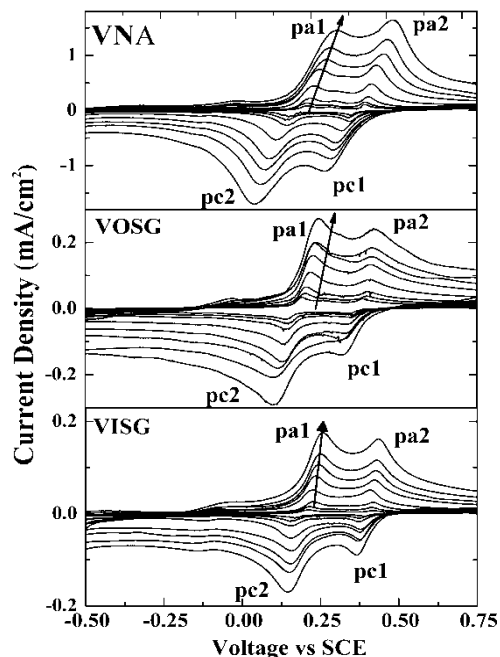


Figure 3.7 Linear-sweep cyclic voltammograms at sweep rates 0.5, 1, 2, 5, 10, 15, and 30 mV/sec of (a) VNA, (b) VOSG, and (c) VISG. The sweep rate increases in the direction of the arrow [134]

Two well defined peaks appear on sweeping the potential downward (marked as pc1 and pc2 in Fig. 3.7) and upward (marked as pa1 and pa2 in Fig. 3.7), accompanied by a two-step electrochromism, *i.e.* yellow to green and then green to blue. Since the electrochemical cell is made up of glass, we have observed the color changes during the electrochemical measurements. The peaks represent the phase transitions upon intercalation and are ascribed to the formation of different crystalline phases of $\text{Li}_x\text{V}_2\text{O}_5$ [119]. As reported in the literature, only a fraction of the V^{5+} ions are reduced to V^{4+} in the first reduction peak (peak pc1 in Fig. 3.7).

The remaining V^{5+} ions are reduced to V^{4+} in a second step (peak pc2 in Fig. 3.7). The same explanation is given for the two oxidation pairs, i.e. the V^{4+} ions incompletely oxidize leaving a (V^{4+} , V^{5+}) mixture at the first peak pa1 in Fig. 3.7, and the oxidation of the remaining V^{4+} ions leading to V^{5+} ions takes place at peak pa2 in Fig.3.7. We have not determined the percentages of Li^+ , V^{5+} , and V^{4+} at each peak. When the CV is measured at lower scan rates, the de-intercalation peak is resolved into three peaks for the VNA and VOSG samples, while the VISG sample exhibits two peaks. The middle peak is the most pronounced for the VNA sample, which has the largest deviation from stoichiometry. This can be seen most readily in Fig. 3.8, which shows the CV of three films at a scan rate of 2 mV/sec from 0 to 0.7 V, and the inset in Fig. 3.8 shows an enlarged portion of the CV of VOSG and VISG between 0.1 to 0.5 V. The appearance of the third peak in the nonstoichiometric films is not due to sample degradation, as the CV for all films were measured over the same voltage range and within the safe limits. Additionally, this peak is present in VNA and VOSG when the first CV is measured over 0.0 to 0.7 V at lower scan rates. Since the third peak intensity is reduced going from VNA to VOSG, and is totally absent in VISG, the intensity of the third peak has the same trend as the deviations from the stoichiometry. It should be noted that the particle size of VNA and VOSG are close to each other, but the electrochemical characteristics of VOSG and VISG are similar, which have approximately the same degree of nonstoichiometry. The presence of three deintercalation peaks in VNA and

VOSG suggests that the crystal structure evolution of $\text{Li}_x\text{V}_2\text{O}_5$, during Li^+ intercalation depends on the stoichiometry of the films.

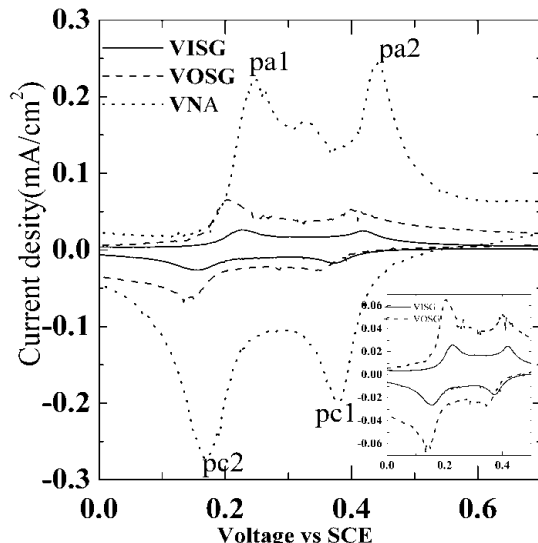


Figure 3.8 Cyclic voltammograms of the three films at the scan rate 2 mV/sec, from 0 to 0.7 V. Inset: An enlarged portion of the CV of VOSG and VISG between 0 to 0.5 V [134]

Further, as the number of peaks during intercalation and deintercalation are different, we surmise that the structural evolution in non stoichiometric samples differ during charging and discharging. However, it will be necessary to characterize the crystal structure at various peak positions to establish the origin of these features. The potential and current density corresponding to the cathodic and anodic peak positions are designated as E_{pc1} , E_{pc2} , I_{pc1} , I_{pc2} , and E_{pa1} , E_{pa2} , I_{pa1} , I_{pa2} , respectively. The anodic and cathodic peak potential, corresponding current density, $I_{pc2}-I_{pa1}$, $I_{pa2}-I_{pc1}$ and the intercalation/deintercalation capacity for the samples measured from the CV at a scan rate of 2mV/sec are summarized in Table 3.1. The peak positions appear at approximately the same voltage for all three films,

corresponding to the peak positions of the CV for crystalline V_2O_5 films measured under identical conditions [142-143]. There is no significant difference in the intercalation and deintercalation capacities, nor in the cathodic and corresponding anodic current density, which are a measure of the reversibility of the system. In the CV at 2mV/Sec, the ratio between Q_c/Q_a where, Q_c is a cathodic charge and Q_a anodic charge for VNA, VOSG, and VISG are 1.02, 1.01 and 1.01, respectively.

Table 3.1 Peak potential and current density, intercalation/deintercalation capacity as deduced from the CV at a scan rate of 2mV/sec for V_2O_5 thin films, together with difference in the cathode and corresponding anode peak current density [134]

ID	E_{pa1} (V vs SCE) / I_{pa1} (mA/c m ²)	E_{pa2} (V vs SCE) / I_{pa2} (mA/c m ²)	E_{pc1} (V vs SCE) / I_{pc1} (mA/c m ²)	E_{pc2} (V vs SCE)/ I_{pc2} (mA/c m ²)	$I_{pc2} -$ I_{pa1} (mA/c m ²)	$I_{pa2} -$ I_{pc1} (mA/c m ²)	Intercalation/ deintercalation capacity	
							mC/cm ²	mAh/g
VNA	0.24/ 0.22	0.44/ 0.24	0.38/ 0.19	0.17/ 0.27	0.05	.05	47.2/ 46.6	130.45/ 128.8
	.21/ 0.065	0.4/ 0.052	0.34/ 0.026	0.13/ 0.068	.003	.026	14/ 13.8	38.7/3 8.14
VISG	0.22/ 0.026	0.42/ 0.025	0.37/ 0.017	0.16/ 0.026	0	.001	5.2/ 5.1	14.4/ 14.1

It is observed that the peak current density and the intercalation and deintercalation capacity is distinctly larger for VNA compared to the sol-gel prepared films. The specific values decrease from VNA to VOSG to VISG, which

follows the same trend as the V:O ratio; the more non-stoichiometric films have larger peak current density and capacity. The difference in current density between the sol-gel films is smaller than the difference between the MOD films and the sol-gel films. Moreover, the capacity of the VNA films is almost one order of magnitude larger than the stoichiometric VISG films. We also note that when the sweep rate increases, the cathodic peaks move to lower potentials, while the corresponding anodic peaks move to higher potentials (Fig. 3.7).

Table 3.2 The difference in ($E_{Pa1}-E_{Pc2}$) at a scan rate of 0.5 and 30 mV/sec and the difference in ($E_{Pa2}-E_{Pc1}$) at a scan rate of 0.5 and 30 mV/sec, together with the slope and the diffusion coefficient (cm^2/sec) corresponding to the peaks as measured from the Randles-Sevcik plot for three V_2O_5 thin films [134].

ID	($E_{Pa1}-E_{Pc2}$) at 0.5mV/sec –	($E_{Pa2}-E_{Pc1}$) at 0.5mV/sec –	Slope/ diffusion coefficient (cm^2/sec) corresponding to the peaks			
	($E_{Pa1}-E_{Pc2}$) at 30mV/sec	($E_{Pa2}-E_{Pc1}$) at 30mV/sec	Pa1	Pa2	Pa3	Pa4
VNA	0.215	0.177	0.009/ 1.1×10^{-9}	0.011/ 1.7×10^{-9}	-0.007/ 6.8×10^{-10}	-0.011/ 1.7×10^{-9}
VOSG	0.096	.07	0.0016/ 3.5×10^{-11}	0.0014/ 2.7×10^{-11}	-0.0008/ 8.8×10^{12}	-0.0016/ 3.3×10^{-11}
VISG	0.066	.056	0.0011/ 1.7×10^{-11}	0.00098/ 1.3×10^{-11}	0.00055/ 4.2×10^{12}	-0.0011/ 1.7×10^{-11}

This can be parameterized by calculating the difference of ($E_{Pa1}-E_{Pc2}$) and ($E_{Pa2}-E_{Pc1}$) at 0.5 mV/sec and 30 mV/sec. These differences are presented in Table

3.2. This increase is the largest for VNA and is the smallest for VISG, and follows the same trend as the non-stoichiometry. Furthermore, the peak current densities increase with increasing sweep rate, suggesting that the electrochemical process is controlled by the diffusion of Li ions.

The rate of increase in peak current with scan rate is the highest for VNA. The anodic and cathodic peak currents vary linearly with the square root of the scan rate in the scan range 0.5 to 30 mV/sec, as shown in Fig. 3.9.

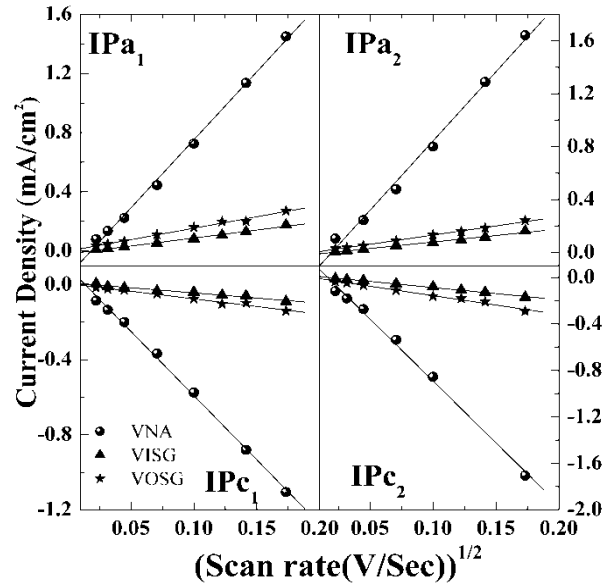


Figure 3.9 Randles-Sevcik plot (i_p vs. $\gamma^{1/2}$) for the two cathodic and anodic peaks for V_2O_5 thin films [134]

In the linear potential sweep voltammogram of a reversible system, the peak current (i_p in amperes) can be expressed using the Randles-Sevcik equation:

$$i_p = (2.69 \times 10^5) n^{3/2} A D^{1/2} C \gamma^{1/2} \quad (3.1)$$

where, n , A , D , C and γ are valence of the guest ion, the electrode area in cm^2 , the chemical diffusion coefficient in cm^2/s , the concentration of guest ions in mol/cm^3 and the sweep rate in V/s [140-142]. According to the Eq. (1), i_p vs. $\gamma^{1/2}$ is linear and the diffusion coefficient can be estimated from the slope of this curve. This slope and the diffusion coefficient for the films for the two anodic and two cathodic peaks are tabulated in Table II. Once again, the diffusion coefficient is largest for VNA.

Preliminary stability measurements on ITO coated glass substrate with respect to SCE (not shown) suggest that the VNA films are less stable than sol-gel inorganic samples. However, a proper investigation of stability of the films requires experiments with respect to a Li metal reference electrode [121]. This requires films to be prepared on substrates like stainless steel, nickel or titanium. Since our samples were prepared on ITO coated glass for technical reasons, we are unable to undertake a complete stability study on these important properties.

The electrochemical properties, such as the intercalation capacity and the diffusion coefficient of V_2O_5 are known to depend on the microstructure and texture. Nanostructure V_2O_5 exhibits a high capacity and large diffusion coefficient because of the large surface area. However, from the following discussion we suggest that the main contributing factor for the higher intercalation capacity and diffusion coefficient of VNA do not arise from the particle size. Both the VNA and VOSG films consist of particles having roughly the same size (Fig.3.5). However, the value of the intercalation capacity and the Li^+ diffusion coefficient of VOSG are small compared to VNA. The VOSG values are close to those measured in VISG, even though the

particle size in VISG is larger than in VOSG samples. Therefore, the variation in the electrochemical properties of these samples is attributed mainly to the difference in stoichiometry. The intercalation of Li^+ in V_2O_5 occurs due to the layered structure of this system, and Li^+ is accommodated within the V_2O_5 sheets, which are stacked along the c -axis. The V_2O_5 lattice in the c direction can also be considered as stacking of alternately pure vanadyl oxygen (O_v) and mixed vanadium oxygen ($\text{V}-\text{O}$) layers [37]. Along the c axis, each vanadyl oxygen is bonded to two vanadium atoms, in one direction by a double bond and in the opposite direction by a van der Waals bond. The successive O_v and $\text{V}-\text{O}$ layers are kept together by an equal number of weak van der Waals bonds and much stronger double bonds ($\text{V}^{5+}=\text{O}$). Therefore, with increase in the oxygen vacancy, due to the softening of $\text{V}=\text{O}$, the V_2O_5 interlayer distance increases. The diffusion coefficient and the Li^+ intercalation capacity of V_2O_5 depend on the distance between V_2O_5 sheets. Hence, we surmise that with decreasing interlayer interactions the inter-planar distance increases and lithium can intercalate more easily, increasing the capacity and the diffusion coefficient. Thus, from the preliminary electrochemical studies we suggest that VNA with increased interlayer distance due to the presence of higher oxygen vacancies, possess increased capacity and diffusion coefficient compared to VOSG and VISG.

In summary, we have prepared V_2O_5 thin films by spin coating using precursors with different carbon to vanadium ratios. Films synthesized from precursors having large carbon content are found to be more nonstoichiometric, due

to the selective oxidation of hydrocarbons by extracting the oxygen atom from the V_2O_5 during annealing. The non-stoichiometry of the films could be characterized by the shift in the stretching vibrational frequency of the shortest bond between vanadium and terminal oxygen. The non-stoichiometry was also confirmed by the variation in the optical band gap and by the observation of planar defects using HRTEM. Because of the increased distance between the V_2O_5 planes, the intercalation capacity and Li^+ diffusion coefficient are larger in the non-stoichiometric films. These experiments suggest that controlling the degree of non-stoichiometry may significantly improve the properties of V_2O_5 films as a cathode material for Li ion batteries. The presence of three anodic peaks in the cyclic voltammograms of the nonstoichiometric films, in contrast to the two anodic peaks present in stoichiometric samples, suggests that the crystal structure evolution of $Li_xV_2O_5$ strongly depends on the V:O ratio in the films. Further crystal structure studies on the partially intercalated phases will be needed to fully characterize the structural evolution of these films and understand the effects of non-stoichiometry.

Chapter 4

ELECTROCHEMICAL PROPERTIES OF V_2O_5 - TiO_2 COMPOSITES

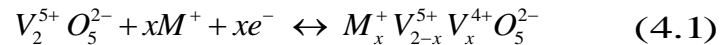
WHY INVESTIGATE V_2O_5 - TiO_2 COMPOSITE THIN FILMS?

While vanadium oxides have great potential as lithium intercalation cathode materials, their use in commercially available energy storage applications is limited for the following reasons: (i) the Li capacity of V_2O_5 decreases over successive charging and discharging cycles. This decrease is due to an increase in electrical resistance produced by ion-trapping arising from slight structural distortions, [144] and (ii) V_2O_5 has a low intrinsic electrical conductivity and diffusion coefficient. For intercalation electrodes, good ionic conductivity is required for fast ion migration during discharging and charging reactions.

Since composites and mixed phases can have different properties than their constituent phases, recent research on lithium intercalation materials has focused on the study of electrochemical characteristics of composites and mixed phases. Composite films of vanadium-titanium oxides have been recognized as promising cathode materials. Studies show that the V/Ti oxide system has a higher cyclic stability than V_2O_5 . However, there is some controversy concerning the capacity of these mixed phases. Investigations by Minett and Owen [145] have shown improved cyclic reversibility but a lower capacity for the mixed V/Ti oxide systems as compared to pure V_2O_5 . Davies *et al.* [146] found that the improved cycling stability

of the V/Ti oxide system is perhaps due to a preferential reduction of Ti^{4+} to Ti^{3+} , which prevents a reorganization of the microstructure. Özer *et al.* [147] found that 5 mol % TiO_2 added to V_2O_5 greatly improved the intercalation capacity. Lee *et al.* [148] observed enhanced intercalation when up to 20 mol % Ti was added to V_2O_5 polycrystalline thin films. Although there is a good agreement on the improvement of cycling stability of the mixed V/Ti-oxide system with the addition of TiO_2 , there are different findings on the Li^+ intercalation properties of V_2O_5 . The measured differences may potentially be attributed to the fact that the electrochemical performance of the electrode is strongly dependent on the preparation method, morphology, crystallinity, defects and oxygen vacancies (nonstoichiometry). It is generally believed that oxygen vacancies are the basic [149] point defects in nonstoichiometric V_2O_5 lattice and the vacancies are created by removing vanadyl oxygen which reduces some of the V^{5+} to V^{4+} for charge balance. The exact interlayer distance between V_2O_5 layers depends on the V_2O_5 stoichiometry. The lithium intercalation takes place according to the following reaction leading to layer separation and elongation of the vanadyl bond, [150-151] where M is a small alkaline metal.

The distance between the V_2O_5 layers plays a major role in its electrochemical properties. Incorporating Ti into the V_2O_5 results in different degrees of non-stoichiometry depending on preparation technique used. This could



in turn give rise to very different intercalation capacities observed in various experimental investigations reported in literature. In this study we have prepared pure and Ti incorporated V_2O_5 films by spin coating using two precursors, namely, Metalorganic (MO), and Sol-gel organic (SG).

4.1 PREPARATION OF V_2O_5 - TiO_2 COMPOSITE THIN FILMS

V_2O_5 - TiO_2 thin films with different mole ratios of Ti (0 -100 mol %) to V were deposited by spin coating on ITO coated glass substrates by mixing vanadium and titanium precursors. The samples used in this study were prepared using MO and SG precursors of vanadium and titanium. The MO precursors, Titanium (IV) 2-ethylhexoxide and vanadium naphthenate oxide in 35% naphthenic acid were mixed with small amounts of xylene to provide proper viscosity. The vanadium SG precursor was prepared by controlled hydrolytic polycondensation of vanadium-tri(isopropoxide) oxide $[VO(OC_3H_7)_3]$ in isopropanol $[C_3H_7OH]$. Typically, 3ml of $VO(OC_3H_7)_3$ was mixed with 30 ml of isopropanol in an open beaker, stirred for 90 minutes, allowed to hydrolyze under the ambient humidity [152]. The titanium SG precursor was prepared from the acetic acid (0.033 mol/l) catalyzed hydrolysis of acetylacetone (0.028 mol/l) modified titanium (IV) tetraisopropoxide, 99.995%, (0.028 mol/l) in isopropanol (140 ml) at 80 °C under an inert atmosphere [153-154]. The films were prepared by dispensing the appropriate precursor solution onto the substrates (area = 1 to 2 cm²) which were spun at 5000 rpm for 15 seconds, followed

by baking for 1 minute at 100/350 °C for films prepared by the SG/MO precursors. This process was repeated 5–10 times to build up the desired film thickness. The film thickness was ~ 300 nm as measured by a step profilometer. The final annealing was done at 450°C in ambient conditions for 60 minutes with heating and cooling rates of 4°C/min. In the following, the films prepared by MO and SG precursors are designated as $M_{(100-x)}V_xTi$ and $SG_{(100-x)}V_xTi$ respectively, where x is the molar percentage of Ti in the precursor. Films prepared using sol-gel organic and metalorganic precursors are named as SG and MO. The mole ratios of vanadium and titanium in the films were close to that of the precursors according to the energy dispersive X-ray spectroscopy (EDS) analysis of the films within an error of ± 1 mole percentage.

4.2 STRUCTURAL CHARACTERIZATION OF V_2O_5 - TiO_2 THIN FILMS

The XRD patterns of V_2O_5 - TiO_2 thin films and ITO coated glass substrate are shown in Fig. 4.1. The peaks are indexed following the standard pattern [JCPDS file no. 41-1426] for polycrystalline, orthorhombic V_2O_5 , with space group Pmnm and unit-cell parameters $a = 1.151$ nm, $b = 0.356$ nm, and $c = 0.437$ nm. We do not observe peaks corresponding to any other vanadium oxide phases than V_2O_5 in both MO and SG films, suggesting that there are no secondary vanadium oxide phases within the XRD detection limits. Pure V_2O_5 thin films prepared using both MO and SG precursors have preferred orientation along $(00l)$ as evidenced by the absence of

peaks from other crystal orientations. With the incorporation of Ti, the degree of preferred orientation decreases. With 30% of Ti incorporation MO films become x-ray amorphous and SG films are polycrystalline. To analyze the shift in XRD peak positions of V_2O_5 , due to Ti addition the peaks corresponding to ITO are taken as the internal standard. There is no observable shift in peak positions, suggesting that there is no noticeable influence on the lattice constant of V_2O_5 upon Ti incorporation. It is known that poor crystallinity is observed due to increased diffusion lengths for the crystallization in the mixed oxide system. No peaks corresponding to TiO_2 or complex vanadium/titanium oxide compounds are observed, indicating that the films comprise of x-ray amorphous TiO_2 phase together with V_2O_5 . Pure TiO_2 films prepared using MO and SG precursors are x-ray amorphous.

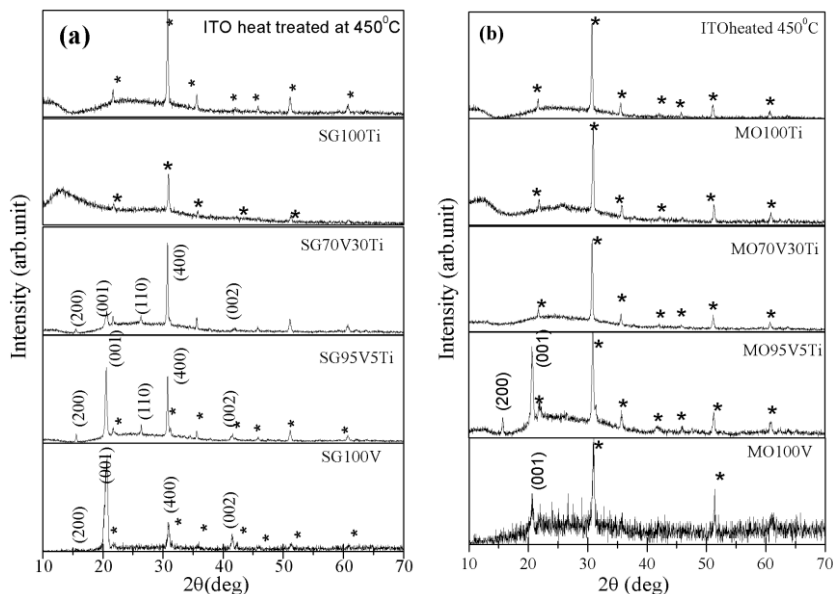


Figure 4.1 XRD of V_2O_5 - TiO_2 thin films prepared using (a) sol-gel (b) metalorganic precursors; * = ITO peaks [155]

The vanadium-oxygen system is complex due to the presence very wide range of ordered and disordered defect structures resulting in a wide range of stoichiometry of the cubic VO lattice and the existence of the homologous series of vanadium oxides [156-160] with a general formula V_nO_{2n-1} ($2 < n < 9$), commonly known as the Magnéli series between V_2O_3 and VO_2 , and the Wadsley series V_nO_{2n+1} between VO_2 and V_2O_5 . Therefore it is difficult to rule out the presence of lower oxides of vanadium and to estimate the V:O ratio in thin films using any of the characterization techniques used to determine the composition and transition metal valence state. Due to a narrow range of stability of different phases and the multivalent vanadium ion, small variation in the preparation methods and/or doping can lead to variations in the stoichiometry.

Raman spectroscopy is used analyze the crystallinity, composition, and the presence of defects in V_2O_5 thin films [154, 161-163]. The Raman modes of V_2O_5 can be classified into internal and external vibrations with respect to the structural unit. The external modes can be considered as relative motions of the units with respect to each other, *i.e.*, translations and librations. The external low-frequency Raman modes at 104, 142 and 194 cm^{-1} correspond to the relative motions of V_2O_5 layers with respect to each other [157] The two peaks at 144 and 194 cm^{-1} are strongly associated with the layered structure and only appear when there is long range structural order. The relative intensity of the 144 cm^{-1} peak with respect to other peaks can be used to estimate the degree of orientation of the film along the c -axis perpendicular to the substrate plane. We have carried out detailed micro-

Raman studies at different locations on all the films to investigate the effect of Ti doping and preparation method on texture, stoichiometry, and composition of these samples. The micro-Raman spectra measured at various locations on a given film are identical, thus confirming the uniformity of the films. The Raman spectra of V_2O_5 - TiO_2 films prepared by MO and SG precursors are shown in Fig. 4.2a and 4.2b. V_2O_5 films prepared both by MO and SG precursors are well crystallized and highly oriented which is evident from the presence of the sharp peaks at $\sim 146\text{ cm}^{-1}$ and $\sim 1000\text{ cm}^{-1}$. The intensity of Raman peaks decreases with increasing Ti concentration. The decrease in the intensity of Raman peaks are in corroboration with the XRD studies, showing the degree of orientation decreases with increasing Ti doping. From the Raman spectra of MO100Ti and SG100Ti (Fig. 4.2a and 4.2b), it can be inferred that the films are comprised of anatase TiO_2 . The Raman lines at 151, 409, 515 and 633 cm^{-1} can be assigned as the E_g , B_{1g} , A_{1g} or B_{1g} , and E_g modes of the anatase phase, respectively [164]. Since the Raman peaks of V_2O_5 and TiO_2 peak positions are very close to each other, it is difficult to resolve TiO_2 peaks in V_2O_5 - TiO_2 films due to very high intensity of V_2O_5 peaks. Internal modes of V_2O_5 , which are observed in the high frequency region, are assigned to different stretching and bending of V-O bonds (Fig. 4.2a and b) [163]. The high frequency Raman peak at 1000 cm^{-1} corresponds to vanadyl oxygen stretching mode ($V=O_v$). It is generally believed that oxygen vacancies are the basic point defects in the V_2O_5 lattice and the vacancies are created by removing O_v with some of the V^{5+} reduced to V^{4+} for charge balance.

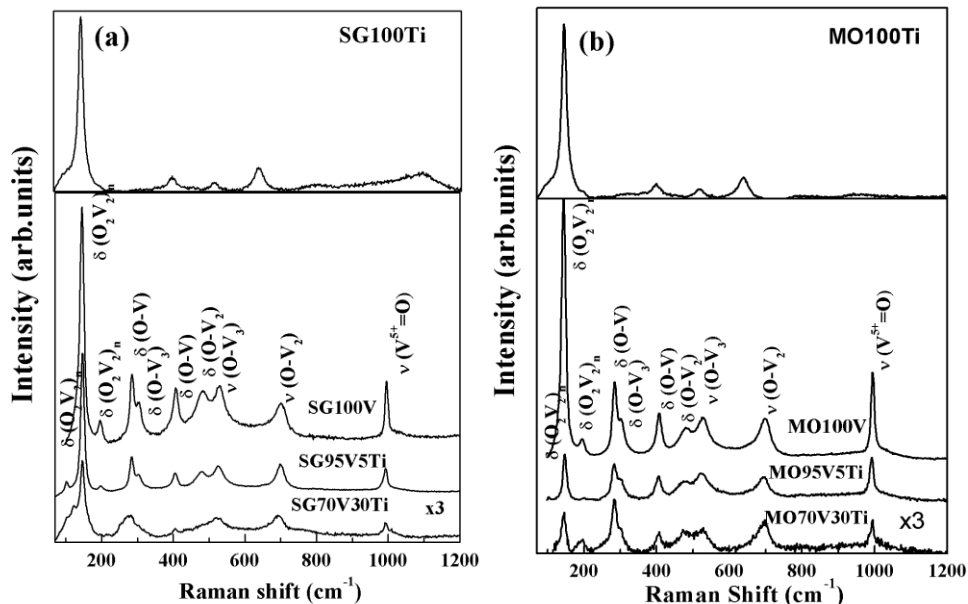


Figure 4.2 Raman spectra of V_2O_5 – TiO_2 thin films prepared using (a) sol-gel (b) metalorganic precursors. The intensities of Raman spectra of SG70V30Ti and MO70V30Ti are multiplied by 3 times the actual value to observe the peaks clearly [155]

The exact $V^{5+}=O$ bond length depends on the V_2O_5 stoichiometry, thus the $V^{5+}=O$ stretching frequency ($\nu_{V=O}$), observed at $\sim 1000\text{ cm}^{-1}$ in a stoichiometric crystal, can be used to determine even small deviations from stoichiometry. This frequency shifts down due to a softening of the $V^{5+}=O$ bond in oxygen-deficient V_2O_5 films. With Ti doping we observe shift in this peak position to lower values in films prepared by SG precursors. There is no conspicuous decrease in the peak position of $\nu_{V=O}$ in films prepared using MO precursor. This can be seen clearly in Fig. 4.3a and 4.3b, which show Raman spectra in the $800\text{ to }1200\text{ cm}^{-1}$. The estimated uncertainty in the peak position is $<1\text{ cm}^{-1}$. The actual peak positions and the presence or absence of different peaks obtained from deconvoluting the spectral profile $\sim 999\text{ cm}^{-1}$ is given as Table 4. 1. The relative intensity of the broad peaks around 933 cm^{-1} ,

840 cm^{-1} , and 1024 cm^{-1} , with respect to the intensity of 999 cm^{-1} peak can be used to determine qualitatively the quality and degree of disorder and the concentrations of oxygen vacancies in V_2O_5 films. The broad peak around 932 cm^{-1} corresponds to $\text{V}^{4+}=\text{O}$ and appears when there is a significant concentration of oxygen defects. Lee et al. [165] have found that with large deviations from stoichiometric V_2O_5 the intensity of the 932 cm^{-1} is higher than the peak at 993 cm^{-1} . With increasing nonstoichiometry the intensity ratio of 932 cm^{-1} and 993 cm^{-1} peaks increases and with further increase in nonstoichiometry the peak at 993 cm^{-1} disappears [161].

Table 4.1 The changes in the optical band gap and the appearance of IR active modes due to the symmetry breaking caused by oxygen vacancies of $\text{TiO}_2\text{-V}_2\text{O}_5$ thin films [155]

Sample	Band gap (eV)			Presence of	
				940 cm^{-1} peak	840 cm^{-1} peak
M100V	1.7		993	x	
M95V5Ti	2.3		992	x	x
M70V30Ti	2.49	2.7	992	x	x
M100Ti		3.55			
SG100V	2.1		995	x	
SG95V5Ti	2.31		992	x	x
SG70V30Ti	2.37		990	x	x
SGTi100		3.5			

Another probe for evaluating the degree of disorder in the films is the presence of the band situated at 840-860 cm^{-1} that corresponds to an infrared active

mode [159]. This mode is normally Raman inactive because of the V_2O_5 symmetry but becomes active within a structurally disordered or non-stoichiometric film. We observe a broad peak situated at 920-950 cm^{-1} in all the films except in SG100V. The intensity of this peak relative to $\sim 992\text{ cm}^{-1}$ increases with increasing Ti concentration, suggesting the increase in oxygen vacancies. However, its intensity is lower than the intensity of $\sim 992\text{ cm}^{-1}$ peak even at 30% of Ti doping suggesting that there is no degradation in the quality of the films. The peak position of stretching mode of $V^{5+}=O$, is the same for both 5% Ti incorporated V_2O_5 films. From this we surmise that the concentration of oxygen vacancies in 5% Ti incorporated films prepared using two types of precursors are of the same order. The peak at 1027 cm^{-1} is present in all the films. This peak has been attributed to the $V^{5+}=O$ stretching of terminal oxygen atoms possibly located on the surface [163].

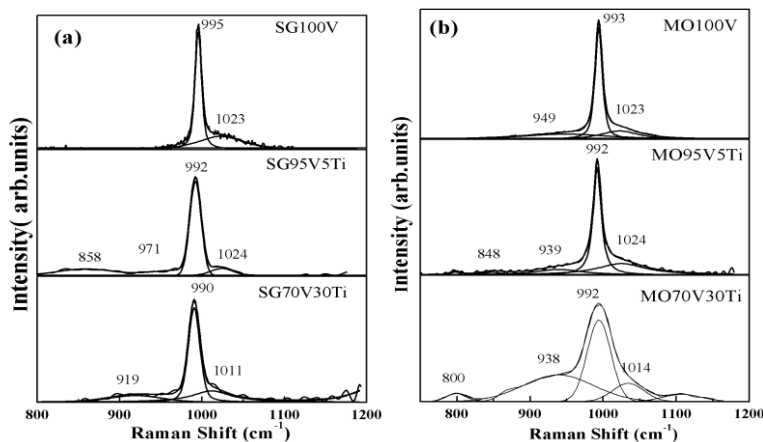


Figure 4.3 Raman spectra of V_2O_5 - TiO_2 thin films prepared using (a) sol-gel (b) metalorganic precursors. The deconvoluted peaks are also shown [155]

To study the effect of Ti incorporation on the morphology and the nature of the defects in micrographs of V_2O_5 V_2O_5 - TiO_2 films we have examined the films

using TEM and HRTEM. The TEM and 5 % Ti doping V_2O_5 prepared by SG and MO precursors is given in Fig. 4.4 and corresponding HRTEM are given in Fig. 4.5. We recorded HRTEM images with a minimum exposure time, since the irradiation of V_2O_5 by electron beam for several minutes can reduce it to lower oxides [166].

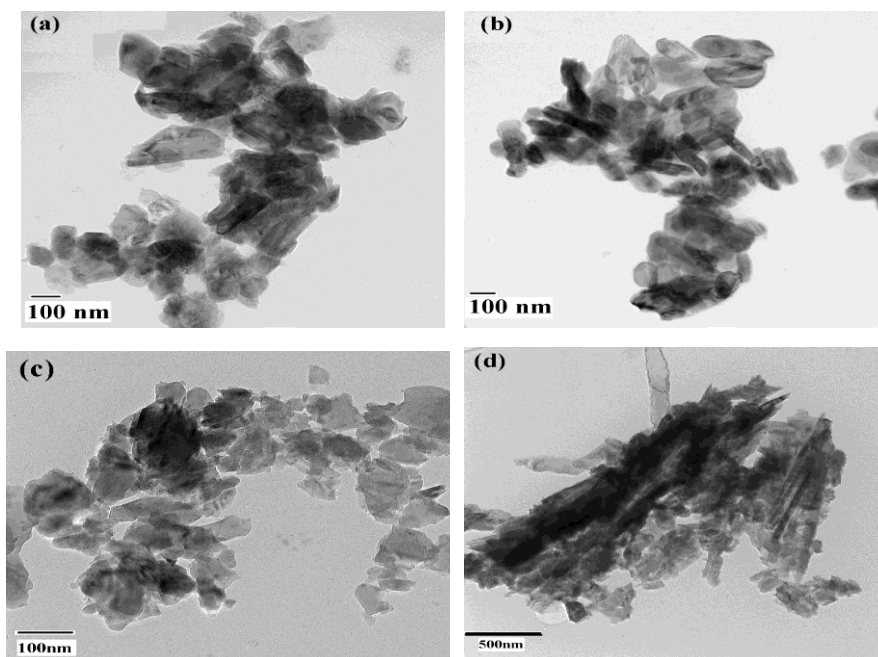


Figure 4.4 TEM micrographs of V_2O_5 - TiO_2 thin films: (a) SG100V, (b) MO100V (c) SG95V5Ti and (d) MO95V5Ti [155]

V_2O_5 films prepared using MO and SG precursors have a particle size distribution of 100 to 300 nm as seen in the Fig. 4a and 4b and the particles exhibit faceted grain growth. V_2O_5 particles have smooth surface morphology, while the V_2O_5 - TiO_2 composite particles are somewhat rough, possibly due to the increased diffusion length for the crystallization process to occur in the mixed oxide system. While 5% Ti doping in SG V_2O_5 films decreases the particle size to 50-250 nm, the

5% Ti doping in MOD film increases the range of particle size and shape distribution (Fig. 4.4c and 4.4d).

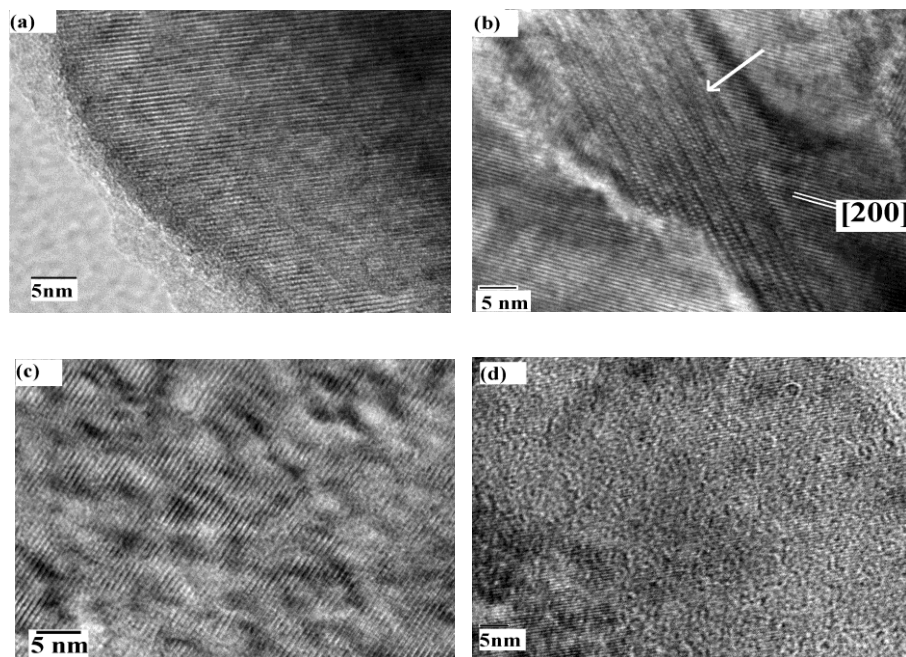


Figure 4.5 HRTEM micrographs of V_2O_5 - TiO_2 thin films: (a) SG100V, (b) MO100V (c) SG95V5Ti and (d) MO95V5Ti. Planar defects and faint and diffuse discontinuity in lattice fringes are marked by an arrow in the HRTWM of the films [155]

From the HRTEM of MO100V and SG100V, it is evident that the V_2O_5 films prepared by MO precursor have a higher concentration of defects compared to films prepared by SG precursor (Fig. 4.5a and 4.5b). Two types of defects are observed in the HRTEM (i) planar defects and (ii) local reduction of V^{5+} to V^{4+} as observed from faint and diffuse discontinuity in lattice fringes. Both local reductions of V^{5+} to V^{4+} and planar defects lead to oxygen vacancies for charge balance. While both types of defects are observed in MO100V in many regions, the SG100V have smaller regions with faint and diffuse fringes. This is in agreement with the Raman observations

that the shift in the stretching mode of $V^{5+}=O$, which is a measure of degree of nonstoichiometry is higher for M100V than SG100V. With 5% Ti doping the nonstoichiometry mainly arises from the local reduction of V_2O_5 phase. The concentration of the defects is of the same order in MO95V5Ti and SG95V5Ti films. It is to be noted here that the Raman spectra of the two films are very similar with broad peaks at 840 cm^{-1} and at 930 cm^{-1} , which appears due to the symmetry breaking in nonstoichiometric V_2O_5 .

Generally, the conduction band in V_2O_5 is formed by vanadium $3d$ bands and the valence band is formed by $2p$ bands of oxygen, which is a direct forbidden transition. In nonstoichiometric films, the empty $3d$ orbital of vanadium adjacent to a vacancy are able to localize excess electrons [167-168]. This leads to the formation of localized states in the gap, which decreases the band gap energy. Therefore, the variation in the bandgap of V_2O_5 on Ti doping can be used to understand its effect on nonstoichiometry. The transmittance spectra of $V_2O_5-TiO_2$ thin films are shown in Fig 4.6a and 4.6b. The decrease in transmission below 600 nm is associated with the fundamental absorption edge. The fundamental absorption edge shows a blue shift with increasing concentration of Ti doping, which corresponds to a shift in the optical band gap to higher energy in films prepared by MO and SG precursor. A marked increase in the optical transmittance in the visible and near infrared region was observed with Ti incorporation. Increase in the transmittance and shift in the band gap with Ti incorporation were also observed in the films prepared by other groups [149]. The optical absorption coefficient α of the films was calculated using

the relation $\alpha t = \ln(1/T)$ where T is the transmittance and t is the film thickness. Fig. 4.6c and 4.6d shows the plots of $(\alpha h\nu)^{2/3}$ versus $h\nu$ for V_2O_5 and V_2O_5 - TiO_2 thin film samples and $(\alpha h\nu)^2$ versus $h\nu$ for TiO_2 films. The optical band gaps, which were evaluated by extrapolating the linear plots to zero, are given in the Table 4.1. This suggests direct forbidden transitions across the energy band gap for V_2O_5 and V_2O_5 - TiO_2 thin films and direct allowed transition for TiO_2 thin films, which is in good agreement with recent reports [169]. The increase in the band gap with Ti doping is more pronounced in films prepared by MO precursor and at 30 % Ti doping we observe two band gaps, suggesting that the film comprises of two phases. It is well known that by alloying two transition metal oxides, it is possible to engineer the band gap either to a higher value or to a lower value [170]. It is evident from Fig. 4.6c and 4.6d, that the band gap of V_2O_5 increases with Ti doping by forming $V_{2-x}Ti_xO_5$ and band gap of TiO_2 decreases with V doping by forming $Ti_{1-x}V_xO_2$. Further due to the formation of localized states in the gap due to oxygen vacancies in a nonstoichiometric V_2O_5 film there is a decrease in the band gap energy. Therefore the net band gap is a result of the combined effects of doping and nonstoichiometry.

The Raman and optical characterization provide important information on the defect structure and oxygen non-stoichiometry in these samples. Based on the Raman studies, we argue that Ti doping enhances the creation of oxygen vacancies to a greater extent in the SG films compared MO films, despite the fact that the undoped MO V_2O_5 films have a higher degree of non-stoichiometry than the undoped SG V_2O_5 films. This is consistent with the observation that with the same

concentration of Ti, the increase in bandgap for the SG $V_{2-x}Ti_xO_5$ films is smaller than that of the MO films.

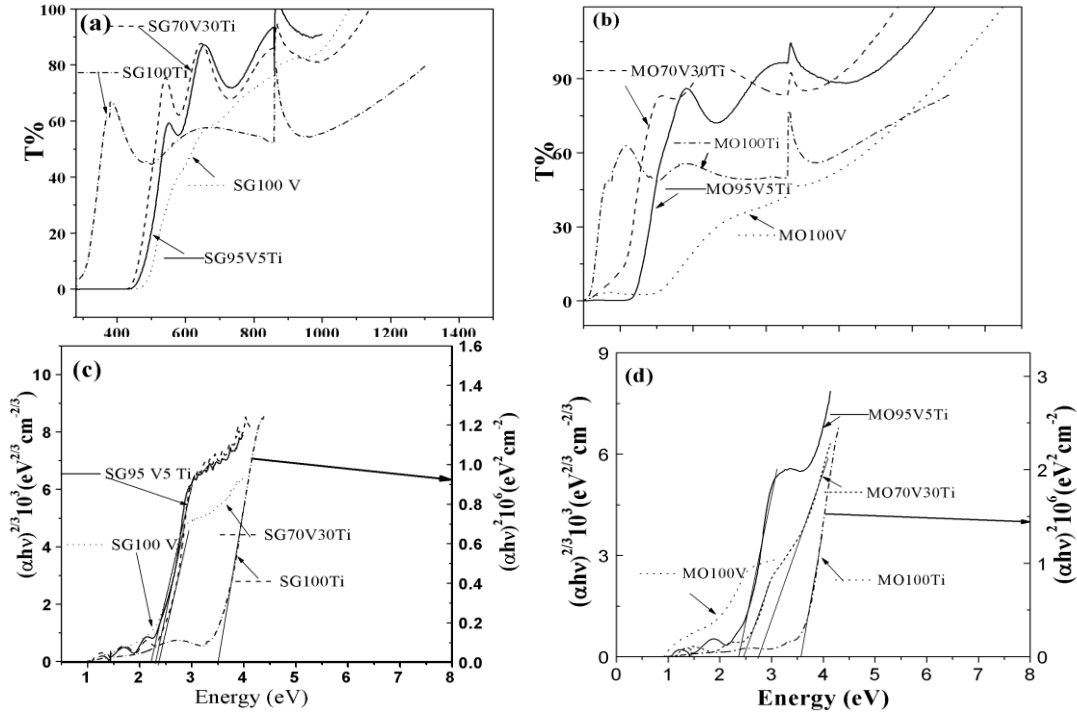


Figure 4.6 Optical transmittance of V_2O_5 - TiO_2 films on ITO coated glass substrate prepared using (a) sol-gel (b) metalorganic precursors and (c) and (d) corresponding plots of $(\alpha h\nu)^{2/3}$ vs. $h\nu$, the photon energy for V_2O_5 - TiO_2 thin films and $(\alpha h\nu)^2$ vs. $h\nu$ for TiO_2 thin films [155]

Therefore, the Ti incorporated films prepared using MO and SG precursors comprise of $V_{2-x}Ti_xO_5$, nonstoichiometric V_2O_5 , and $Ti_{1-x}V_xO_2$. We should note here that both Raman spectra and the UV-Vis spectra of M95V5Ti and SG95V5Ti have similar characteristics.

4.3 ELECTROCHEMICAL CHARACTERIZATION OF V_2O_5 - TiO_2 THIN FILMS

To study the effect of Ti doping on the electrochemical characteristics of V_2O_5 thin films, we carried out cyclic voltammetry measurements of V_2O_5 - TiO_2 thin films. Figures 4.7a and 4.7b show linear-sweep cyclic voltammograms (CV), *i.e.* the plot of current versus applied voltage at sweep rates from 0.5 to 30 mV/sec for the MO and SG V_2O_5 films.

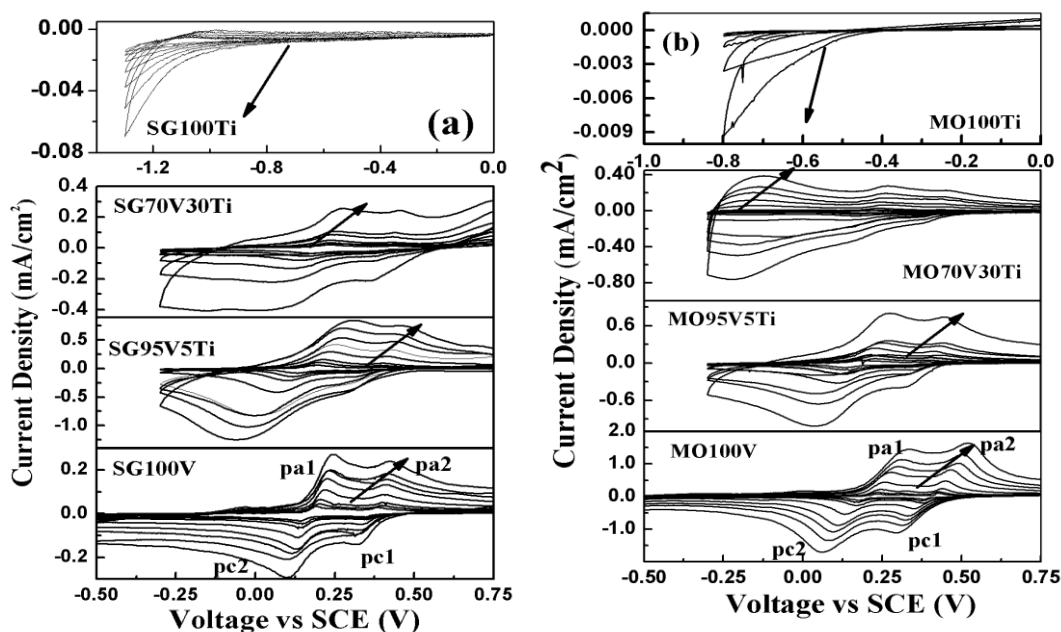


Figure 4.7 Linear-sweep cyclic voltammograms of V_2O_5 - TiO_2 thin films at sweep rates of 0.5, 1, 2, 5, 10, 15, and 30 mV/sec prepared using (a) sol-gel (b) metalorganic precursors [155]

The sweep rate increases in the direction of the arrow. The direction of the sweep is marked by an arrow on the cur in Fig. 4.7. The CV from 0 to -0.8V of MO TiO_2 films, and 0 to -1.2V for SG films is also given in the same figures for the comparison. Although anatase TiO_2 is known as the intercalation material (up to $x = 0.5$ to 1 in

Li_xTiO_2) depending on the processing condition [171-172], the CV of both type of TiO_2 films revealed very low lithium intercalation capacity within the potential range scanned, as can be seen from the low intercalation current density. However there is an onset of the lithium intercalation peak at -0.6V and -1.0 V in MO and SG films. The CV of the pure V_2O_5 films prepared by the two methods show two cathodic reduction peaks (pc1, pc2), which are attributed to lithium intercalation and two anodic peaks (pa1 and pa2), which correspond to lithium extraction. The peaks are ascribed to the formation of different crystalline phases of $\text{Li}_x\text{V}_2\text{O}_5$ [169]. At lower scan rates, there exists a small anodic peak (pa3) between pa1 and pa2, in pure V_2O_5 which is readily observed in Fig. 4.8a and 4.8b. With increase in the scan rate the three anodic peaks broaden and merge together to form two peaks. With 5% Ti titanium incorporation, each of the cathodic (pc1 and pc2) and anodic peaks (pa1 and pa2) are still distinguishable, however the peaks broaden further. In films prepared by MO precursors, at higher scan rate, noticeable contribution from TiO_2 to the CV is seen. The potential (E) and current density (I) corresponding to the cathodic and anodic peak positions are designated as E_{pc1} , E_{pc2} , I_{pc1} , I_{pc2} , and E_{pa1} , E_{pa2} , I_{pa1} , I_{pa2} , increase with 5% Ti titanium incorporation, each of the cathodic (pc1 and pc2) and anodic peaks (pa1 and pa2) are still distinguishable, however the peaks broaden further in the scan rate the three anodic peaks broaden and merge together to form two peaks.

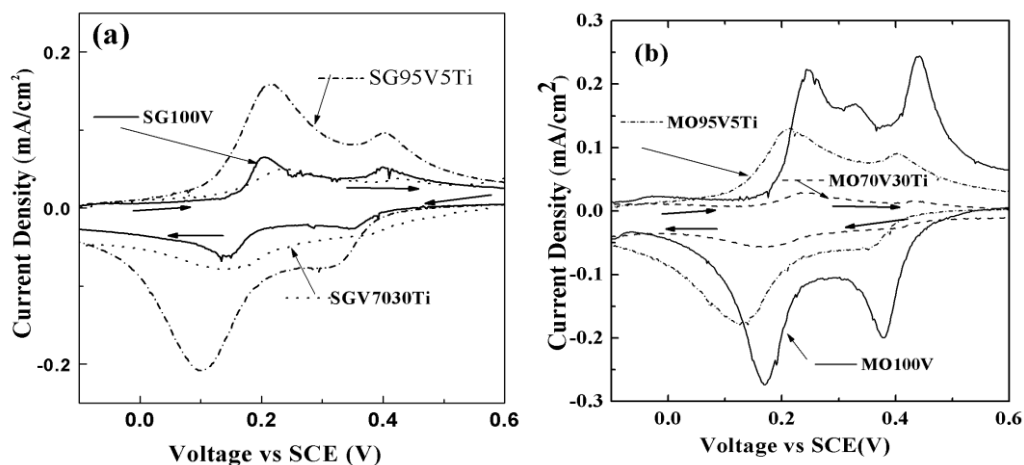


Figure 4.8 Cyclic voltammograms of V_2O_5 - TiO_2 thin films prepared using (a) sol gel (b) metalorganic precursors at a scan rate of 2 mV/sec from -0.1 to 0.6 V. The arrow mark indicates the direction of voltage sweep [154]

In films prepared by MO precursors, at higher scan rate, noticeable contribution from TiO_2 to the CV is seen. The potential (E) and current density (I) corresponding to the cathodic and anodic peak positions are designated as E_{pc1} , E_{pc2} , I_{pc1} , I_{pc2} , and E_{pa1} , E_{pa2} , I_{pa1} , I_{pa2} , respectively. The anodic and cathodic peak potential, corresponding current density, and the intercalation/deintercalation capacity for the samples measured from the CV at a scan rate of 2mV/sec are summarized in Table 4.2. The peak positions appear at approximately the same voltage for all the films, corresponding to the peak positions of the CV for crystalline V_2O_5 films measured under identical conditions [173-174]. However, at higher scan rate, with Ti incorporation, the current at cathodic peaks are significantly higher than from the corresponding anodic peak current and the difference increases with increase in Ti concentration.

Table 4.2 Peak potential and current density, intercalation/deintercalation capacity as deduced from the CV at a scan rate of 2mV/sec for V₂O₅ thin films [154]

ID	E _{pa1} (V vs SCE) / I _{pa1} (mA/cm ²)	E _{pa2} (V vs SCE) / I _{pa2} (mA/cm ²)	E _{pc1} (V vs SCE) / I _{pc1} (mA/cm ²)	E _{pc2} (V vs SCE) / I _{pc2} (mA/cm ²)	Intercalation/deintercalation capacity	
					(mC/cm ²)	(mAh/g)
M100V	0.24/0.22	0.44/0.24	0.38/-0.19	0.17/-0.27	47.2/46.6	130.45/128.8
M95V5Ti	0.21/0.13	0.41/0.089	0.35/0-057	0.13/0.18	27.7/27.1	76.5/74.9
M70V30Ti	0.24/0.029	0.44/0.016	0.41/0.026	0.17/0.056	11/10.7	30.40/29.6
SG100V	0.21/0.065	0.4/0.052	0.34/-0.026	0.13/-0.068	14/13.8	38.7/38.1
SG95V5Ti	0.22/0.16	0.4/0.096	0.32/-0.074	0.1/-0.21	29/28.5	80.2/78.8
SG70V30Ti	0.23/0.05	0.43/0.038	0.38/0.032	0.15/0.08	16.8/15.2	46.4/42

This suggests that Ti incorporated films have reversible lithium intercalation only at low scan rates unlike pure V₂O₅. The undoped MO V₂O₅ film has the highest intercalation capacity, while the capacity of the undoped SG V₂O₅ film is significantly lower. The intercalation/deintercalation capacity decreases with Ti incorporation in films prepared using MO precursors. While in films prepared by SG films, the Li⁺ intercalation capacity increases initially with 5% Ti incorporation (Fig. 4.9). As the Ti concentration increases (30%) the capacity decreases and is similar to pure V₂O₅. However the intercalation capacity of 5% Ti incorporated SG and MO V₂O₅ films have the same value of 28mC/cm². The effect of Ti incorporation

on the capacity of V_2O_5 films prepared using two precursor is more readily seen in the plot of Li intercalation capacity vs. Ti concentration. It is interesting to note that the capacities of the 5% Ti doped MO and SG films are very similar, and both these samples have similar non-stoichiometry, as determined by XRD, Raman, and optical measurements. We also note that when the sweep rate increases, the cathodic peaks move to lower potentials, while the corresponding anodic peaks move to higher potentials. Furthermore, the peak current densities increase with increasing sweep rate, suggesting that the electrochemical process is rate limited by the diffusion of Li ions.

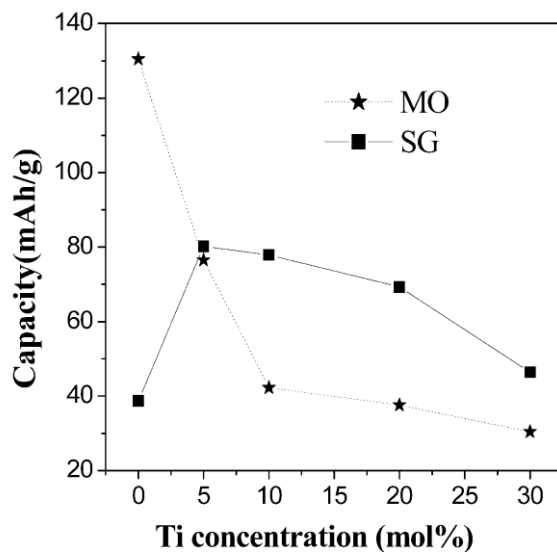


Figure 4.9 Variation in the lithium intercalation capacity of V_2O_5 thin films prepared using sol gel and metalorganic precursors with respect Ti concentration [155]

In pure and 5% Ti incorporated V_2O_5 films, the anodic and cathodic peak currents vary linearly with the square root of the scan rate in the scan range 0.5 to 30 mV/sec, as shown in Fig. 4. 10 (for pa1 and pc2). Because of the influence of Ti incorporation, it is hard to deconvolute different cathodic and anodic peaks in 30% Ti incorporated V_2O_5 films. Therefore the diffusion coefficient is calculated only for the peaks pa1 and pc2 of pure and 5% Ti incorporated V_2O_5 films.

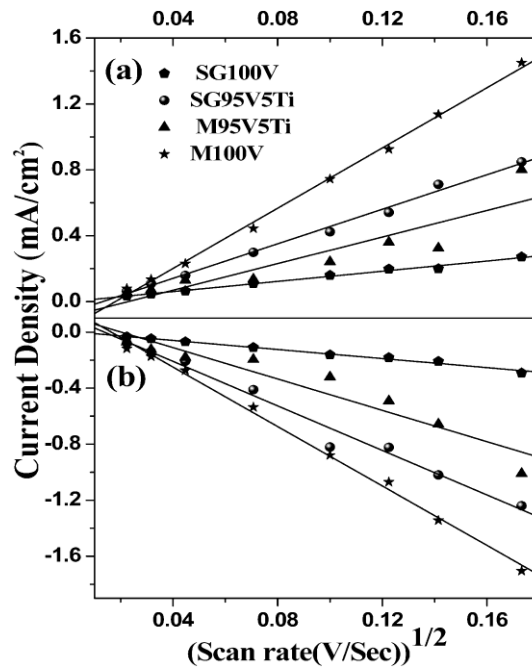


Figure 4.10 Randles-Sevcik plot (i_p vs. $\gamma^{1/2}$) for the peaks (a) pa1 and (b) pc2 of pure V_2O_5 and 5%Ti incorporated V_2O_5 thin films thin films [155]

In the linear potential sweep voltammogram of a reversible system, the peak current (i_p in amperes) can be expressed using the Randles-Sevcik equation:

$$i_p = (2.69 \times 10^5) n^{3/2} A D^{1/2} C \gamma^{1/2} \quad (4.2)$$

where, n , A , D , C and γ are valence of the guest ion, the electrode area in cm^2 , the chemical diffusion coefficient in cm^2/s , the concentration of guest ions in mol/cm^3 and the sweep rate in V/s [173-175] According to the Eq. (1), i_p vs. $\gamma^{1/2}$ is linear and the diffusion coefficient can be estimated from the slope of this curve. This slope and the diffusion coefficient for the films for the anodic and cathodic peaks are tabulated in Table 4. 3. The diffusion coefficient is the highest for MO100V, and it decreases with Ti incorporation. The diffusion coefficient is the smallest for SG100V and increases with 5% Ti incorporation. The diffusion coefficient of 5% Ti doped V_2O_5 films prepared by MO and SG have values of same order of magnitude.

Table 4.3 The diffusion coefficient (cm^2/sec) corresponding to the peaks as measured from the Randles-Sevcik plot for three V_2O_5 thin films [155]

sample	P_{a1}	P_{c2}
M100V	1.1×10^{-9}	1.7×10^{-9}
M95V5Ti	2.3×10^{-10}	4.3×10^{-10}
SG100V	3.5×10^{-11}	3.3×10^{-11}
SG95V5Ti	3.8×10^{-10}	8.7×10^{-10}

From the Raman, HRTEM and optical studies we surmise that the non-stoichiometric is in the order of $\text{SG100V} < \text{M100V} < (\text{SG95V5Ti} = \text{MO95V5Ti}) < (\text{SG70V30Ti} = \text{MO70V30Ti})$. This suggests that films having similar nonstoichio-

metry have similar values of intercalation capacity and diffusion coefficient. Critical value of nonstoichiometry is required to achieve higher capacity as the proper stoichiometry or a high nonstoichiometry results in lower intercalation capacity. Changes in the Lithium insertion capacity of V_2O_5 due to incorporation of Ti can be attributed to the changes in (1) particle size and morphology (2) crystallinity and (3) nonstoichiometry. It is well-known that the particle size and surface area of the electrode dramatically affect the intercalation rate and capacity because Li^+ diffusion within the electrode material is slower and more difficult than in a liquid electrolyte or along the grain boundaries. Therefore, a short diffusion length due to small particle size will prevent concentration polarization of Li^+ within the V_2O_5 - TiO_2 electrode. This maintains the cell voltage stopping the termination of the discharge until the maximum capacity of the material is reached. While 5% Ti doping in SG100V films decreases the particle size from 100-300 nm to 50-250 nm, 5% Ti doping in MO film increases the range of particle size and shape distribution. Therefore there is an increase in the capacity of SG V_2O_5 film and decrease in the capacity of MOD films due to the 5% incorporation of Ti. The second possible mechanism is related to the poor crystallinity or partially amorphous phase within the V_2O_5 - TiO_2 films. The mixed V_2O_5 - TiO_2 films show poor crystallinity as compared to the pure V_2O_5 film. It has been reported in various studies that amorphous vanadium oxides have a higher Li^+ intercalation capability than crystalline vanadium oxides due to their more open structure. Although it is known that TiO_2 and V_2O_5 do not form a solid solution, it might be possible that a trace amount of Ti

was incorporated into vanadium oxide structure in the present study. The films used in this work were synthesized from solutions that consist of both Ti and V ions homogeneously mixed at the atomic level such a homogeneously mixed state would likely be retained in the resulting films upon evaporation of solvent and makes it possible to achieve partial substitution at the V site by a Ti ion during firing. Surca *et al.* [176] mention the possibility of the substitution of V by Ti in amorphous V_2O_5 . The valence state of the Ti ion is lower than V ion in V_2O_5 , and the ionic radius of tetravalent titanium is greater than that of pentavalent vanadium; thus, the size and shape of the polyhedron may change, which may result in distortion of the pyramidal chain array of VO_5 and render more open space for Li^+ insertion. With Ti incorporation, the crystallinity decrease in MOD and SG films. However, only with 5% Ti incorporated SG V_2O_5 films, the capacity increases and it is equal to that of MO95V5Ti. Even though with 30% Ti incorporation both MO and SG films are close to amorphous and are more nonstoichiometric, the capacity decreases. The third possible contributing factor is the changes in the stoichiometry due to Ti incorporation. In a nonstoichiometric film the distance between V_2O_5 layers increases with increasing nonstoichiometry. This also renders lithium to get in to the structure easily. However, with large concentration of defects due to increased nonstoichiometry, the film quality degrades. In addition, reduced amount of active vanadium oxide phases due to the formation of more defective V_2O_5 films would account for the decreases in the lithium intercalation capacity with increase in Ti incorporation. Therefore we conclude from our studies that to attain higher Li

intercalation capacity it is necessary to have a critical concentration of oxygen defects in V_2O_5 structure.

In conclusion, the electrochemical studies by cyclic voltammetry indicate that the Li^+ intercalation capacity and Li^+ diffusion coefficient are increased by an order of magnitude in the nonstoichiometric films prepared by MO precursor compared to stoichiometric V_2O_5 film prepared using SG precursor. Ti incorporation also introduces some degree of nonstoichiometry in V_2O_5 films. We observe that in films prepared using MO precursors Ti incorporation decreases the intercalation capacity to $27\text{mC}/\text{cm}^2$ compared to the capacity of $47\text{mC}/\text{cm}^2$ for pure V_2O_5 film. While in films prepared using SG precursors 5% Ti incorporation increases the capacity to $27\text{mC}/\text{cm}^2$ from $14\text{mC}/\text{cm}^2$ the capacity of pure V_2O_5 film. However, the capacity of 5% Ti incorporated V_2O_5 films prepared by MO and SG precursors have same value of the intercalation capacity and diffusion coefficient. This is attributed to the similar range of nonstoichiometry observed in 5% Ti incorporated V_2O_5 films prepared using MO and SG precursors. The nonstoichiometry of the films is characterized by the shift in the stretching vibrational frequency of the shortest bond between vanadium and terminal oxygen. The non-stoichiometry was also confirmed by the variation in the optical band gap and by the observation of defects using HRTEM. The results indicate that it is essential to have a critical V:O ratio to achieve a high intercalation capacity, and values that differ from this critical value lead to a decrease in capacity.

Chapter 5

DIELECTRIC PROPERTIES OF TiO₂ THIN FILMS

WHY INVESTIGATE TiO₂ THIN FILMS?

Titanium dioxide, TiO₂, is an important wide bandgap semiconducting oxide with important technological applications in, including, gas sensors, anti-reflection coatings, electro chromic displays, dye-sensitized solar cells, wave guide, photocatalysis, high-k dielectrics etc. It has high refractive index 2.6 [177] and high dielectric breakdown strength of up to 4 MV/cm [178]. Even though pure TiO₂ is classified as an insulator because of its high resistivity of $\sim 2\text{-}4\text{ M}\Omega$, it generally behaves as an n-type semiconductor due to oxygen deficiency. TiO₂ has high dielectric constant which is highly anisotropic in a single crystal with $\epsilon_r \sim 89$ perpendicular and ~ 175 parallel to the *c*-axis respectively [179]. Various studies have shown that the dielectric constant of polycrystalline TiO₂ thin film ranges from 10 to 180 [180]. This variation in the values of dielectric constants in thin films critically depend on many factors such as film quality, morphology, crystallinity, stoichiometry, etc., which are in turn strongly determined by precursors used, preparation methods and conditions. The average dielectric constant of TiO₂ thin film is around 60, as reported by many studies [181]. Amorphous thin films have lower dielectric constant of around 20 [182] while well crystallized rutile phase has been reported to have a very high dielectric constant of up to 120 [183]. Titanium dioxide exists in three well known distinct thermodynamical phases: anatase, rutile

and brookite. Anatase is thermodynamically metastable phase which starts to form at as low as 350 °C depending on the preparation method and route and starts to convert to thermodynamically stable rutile phase with the increase in baking temperature. There is no universal temperature at which TiO₂ converts to rutile which widely varies from 550 °C to up to 1000 °C depending on the preparation methods. TiO₂ generally exists in mixed phase of anatase and rutile within a wide range of temperatures.

The dielectric properties and leakage current of TiO₂ thin film can be improved by properly doping TiO₂ with other transition metal cations. For example, proper amount of Zr⁴⁺ doping for Ti⁴⁺ can significantly improve leakage current, photocatalytic performance as well as dielectric loss [184]. We have studied the properties of pure TiO₂ and Zr-doped TiO₂ thin films prepared by spin coating using metal organic decomposition (MOD) technique. The microstructure and phase of the TiO₂ thin films are controlled by heat treatment process by annealing the thin films in the temperature range of 650 to 950 °C. Both XRD and Raman spectra show TiO₂ to be mostly in anatase form below the annealing temperature of 850 °C and in rutile phase above 850 °C. However, the Zr doping suppresses the formation of rutile phase.

We have studied I-V characteristics and frequency dependence of dielectric constants of pure and Zr-doped TiO₂ in the frequency range of 100 Hz - 1 MHz. We find an improvement in leakage current with increasing annealing temperature from 650 to 950 °C for both TiO₂ and Zr-doped TiO₂, but no significant improvement

in the leakage current upon Zr doping. The dielectric constant of pure TiO₂ films improves from 30 to 80 with increasing annealing temperature whereas that of Zr-doped TiO₂ is almost independent of annealing temperature and its value is ~36. This may be attributed to the persistence of TiO₂ anatase phase over a wide range of annealing temperatures for Zr-doping. In addition to MOD method, sputter deposition method was also used to fabricate TiO₂ thin films. It is well known that the latter method gives a denser, crack free and crystalline film. I-V characteristics as well as frequency dependent dielectric constant data are analyzed to understand the conduction/dissipation mechanism in these films.

5.1 SYNTHESIS AND CHARACTERIZATION OF TiO₂ THIN FILMS

TiO₂ and 25 at% Zr-doped TiO₂ thin films were deposited on highly conducting n-type silicon (100) substrates by MOD method (described in Chapter 2) using metal organic precursors. Silicon substrates were cut into 1.5 cm × 1.5 cm square size. The substrates were first cleaned with soap cleanser. Subsequently the substrates were cleaned ultrasonically for 15 min in acetone, methanol and deionized water for 10 minutes in each of these solutions. Titanium (IV) 2-ethylhexoxide [Ti(OCH₂CH(C₂H₅)(CH₂)₃CH₃)₄] and C₃₂H₆₀O₈Zr (97%) were used as the Ti precursor and Zr-precursor respectively. For the preparation of TiO₂ films the Titanium (IV) ethylhexoxide precursor was diluted with xylene to obtain optimal viscosity needed for spin coating. To prepare Zr-doped TiO₂ the two solutions of Ti and Zr precursors were added according to the atomic ratio of (Ti: Zr = 75:25). A

small amount of xylene was added to control the viscosity of the mixture and the proper ratio is very crucial for preparing high quality crack free films. Typical ratio of precursor to toluene was 1:1 by volume for pure TiO_2 and 1:4 for the 25% Zr-doped TiO_2 respectively. The films were spin coated on the substrates with a spinning rate of 5000 rpm for 15s. The film was immediately transferred to a furnace and baked in the ambient atmosphere at 500 °C for about 1.5 min. Then the film was taken out and cooled in air for 1 min before depositing additional film. This process was repeated 5-10 times to build up to the desired thickness. The as deposited film was finally cut into 4 equal pieces and annealed at 650 °C, 700 °C, 750 °C and 850 °C, respectively, for 1 hr with a heating/cooling rate of 3 °C/minute. The lower heating/cooling rate was chosen to prevent the development of cracks due to differential expansion/contraction of the film due to rapid annealing. The same process was used to prepare the 25% Zr-doped TiO_2 thin films.

TiO_2 thin films were also prepared by RF magnetron sputter deposition technique. Pure metallic titanium (99.99%) was used as the sputtering target, and pure oxygen (99.99%) and argon (99.995%) were used as reactive and sputtering gases respectively. The samples were deposited at an oxygen partial pressure of 1.5×10^{-3} Torr, ambient chamber temperature as the substrate temperature and sputtering pressure of 1.5×10^{-2} Torr. A deposition time of 2 hours produced around 200 nm thick films as measured from cross-sectional SEM. The as prepared film was cut into 4 equal pieces and the films were annealed in an air ambient atmosphere at 650 °C, 750 °C, 850 °C and 950 °C respectively at heating/cooling rate

of 3 °C/min. In the following text MODT and MOD75T represent TiO₂ and 25% Zr-doped TiO₂ films, respectively, prepared by MOD technique while SPDT represents TiO₂ films prepared by sputter deposition technique.

TiO₂ thin films were characterized and analyzed using various techniques. Microstructure and crystallinity of the films were studied using Raman spectroscopy and x-ray diffraction method. Cross-sectional SEM and EDAX were used to determine the film thickness and composition respectively. I-V measurements were performed to study the leakage behavior and conduction mechanisms. Frequency dependence dielectric measurements in the frequency range of 100 Hz - 1 MHz were performed using HP LCR Meter to study the dielectric behavior of the films with as a function of frequency.

The particle size of the films was calculated by applying Debye-Scherrer relation (Eq. 2.2) to x-ray diffraction peaks (to be presented in the following sections) and the plot is shown in Fig. 5.1. The particle size of the films increases with the increase in the range of annealing temperature. Above the annealing temperature of 850 °C the particle size of MOD and sputter deposited films almost remain the same while the particle size of 25% Zr-doped TiO₂ increases linearly within the range of annealing temperatures. Of the three films, sputter deposited film has the largest particle size of ~28 nm at the annealing temperature of 650 °C and increases to ~46 nm at the annealing temperature of 950 °C while 25% Zr-doped films has the smallest particle size in the range of 15 to 28 nm within the range the annealing temperature.

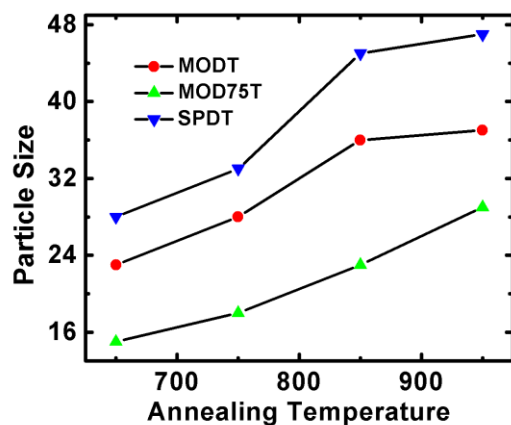


Figure 5.1 Variation in particle size with annealing temperature of the films

The thicknesses of the films were measured using cross sectional SEM. Figures 5.2 (a-c) show cross-sectional SEM images of TiO₂ films. The thickness of the MODT and MOD75T films were around 500 nm, while the thickness of the SPDT films were around 200 nm.

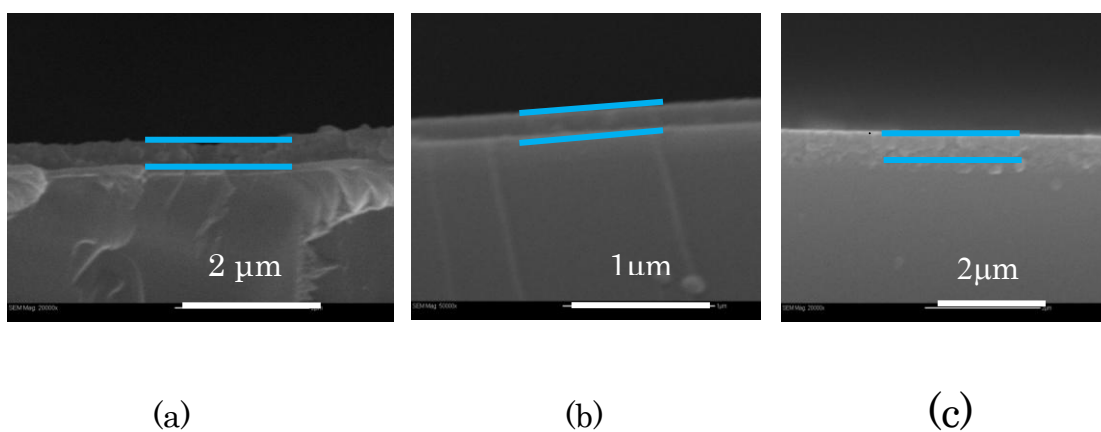


Figure 5.2 Cross-sectional images of (a) MODT (b) MOD75T and (c) SPDT films

Figure 5.3 (a) shows the XRD spectra of the MOD thin films. Sharp intensity peaks verify that all films are well crystallized and polycrystalline in nature. The

relative intensity of the x-ray reflections indicates that the particles are randomly oriented with no preferential orientation of the thin film growth. The XRD peaks of the films were indexed according to the standard index of JCPDS database (JCPDS no. 18-1175 and 84-1286). There are no peaks characteristic of rutile phase in the 650 °C annealed sample and the peaks (101), (004), (200), (211) and (118) correspond to the anatase phase as determined from the JCPDS database. With increasing annealing temperature, anatase peaks start to diminish and rutile peaks begin to appear and grow. The samples annealed at 750 °C and 850 °C have mixed phases of anatase and rutile. The sample annealed at 950 °C is predominantly rutile with no observed reflections from anatase, within the limit of x-ray detection. The peaks corresponding to the rutile phase (110), (101), (111), (211) and (200) are marked in the Fig. 5.2. The rutile phase starts to form above 650 °C and increases with increasing annealing temperature. In general, the anatase phase does not disappear even at very high temperatures, well over 1000 °C [185]. But the studies have shown that the anatase phase exists mostly on the surface of the rutile particles. Raman spectroscopy is a more powerful technique for characterizing the rutile and anatase phase. Even a small percentage of (<1%) anatase phase can be easily detected by using the Raman spectroscopy. Figure 5.3 (b) shows the Raman spectra of the films annealed at different temperatures. Raman spectra with sharp peaks is an indicative of films being well crystallized which is also supported by the results of XRD. The peaks at 300 cm^{-1} and 520 cm^{-1} correspond to the Si substrate. The film annealed at 650 °C shows only anatase peaks. The peaks at 144, 400 and

639 cm^{-1} correspond to the E_g , B_{1g} and E_g modes of the anatase TiO_2 phase. A rutile peak at 448 cm^{-1} starts to appear in the sample annealed at 750 $^\circ\text{C}$. The samples annealed at 850 $^\circ\text{C}$ and 950 $^\circ\text{C}$ show only peaks that correspond to the rutile TiO_2 . There are no peaks that correspond to the anatase phase. The peaks at 236, 448 and 612 cm^{-1} correspond to $B_{1g} + B_{1g}$, E_g and A_{1g} modes of the rutile phase. The Raman spectra of the films annealed at 850 $^\circ\text{C}$ and 950 $^\circ\text{C}$ are almost similar. This indicates that the predominant phase that forms at 850 $^\circ\text{C}$ is rutile and is stable within the large range of temperature up to 950 $^\circ\text{C}$.

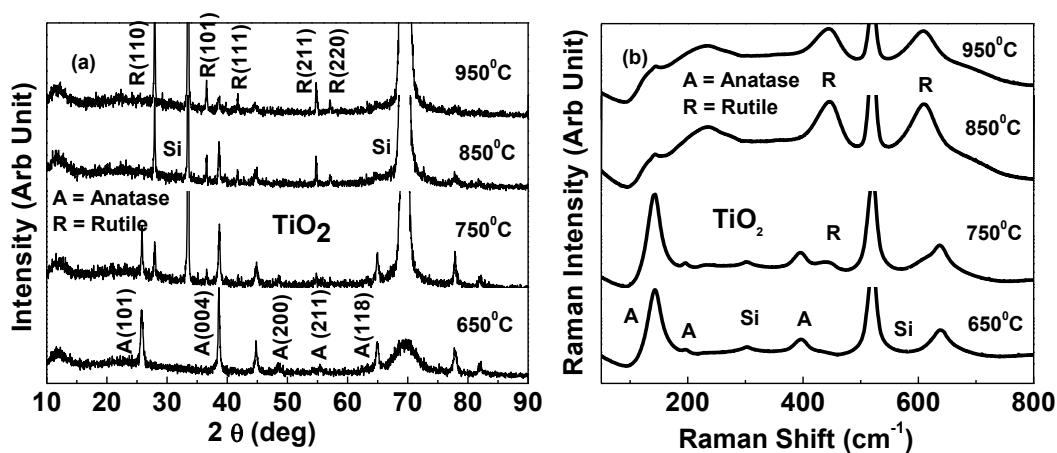


Figure 5.3 Plots of (a) XRD and (b) Raman spectra of the MODT films annealed at different temperatures

The current-voltage (I-V) curves of the films are shown in Fig 5.4. The curves are slightly non-symmetric with respect to positive and negative bias which indicates rectifying characteristics of the MIM structure. The leakage current decreases with increasing annealing temperature. The films annealed at 650 $^\circ\text{C}$ and 750 $^\circ\text{C}$ have leakage current in the range of 10^{-2} to 10^{-5} A/cm^2 compared to the films annealed above 800 $^\circ\text{C}$, where the leakage current decreased to less than 10^{-5}

A/cm^2 . The leakage current of the sample annealed at 950 °C is the lowest and is of the order of $10^{-6} A/cm^2$ at an electric field of 175 kV/cm. The thin films break down above certain applied voltage. The films annealed at 850 °C and 950 °C have higher dielectric strength of > 200 kV/cm. However, the films annealed at 650 °C and 750 °C have lower dielectric breakdown voltage of ~ 100 kV/cm. This shows that in general our thin films annealed at low temperature with predominant anatase form of the TiO_2 has higher leakage and low dielectric breakdown voltage than the high temperature annealed thin films with rutile form. The dramatic improvement in the leakage current and dielectric breakdown field with the increase in annealing temperature can be attributed to the high degree of crystallinity and removal of defects such as electron traps, dangling bonds and oxygen vacancies due to high temperature sintering.

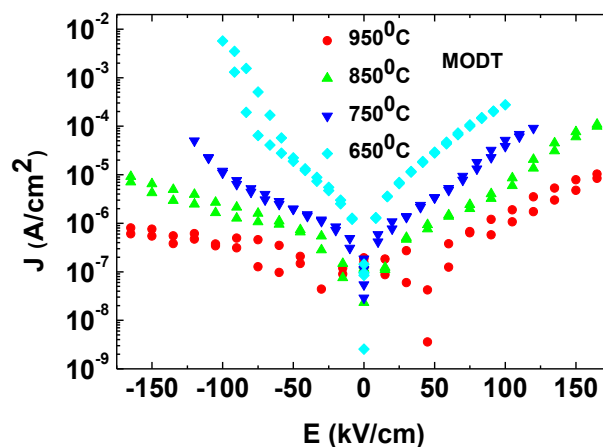


Figure 5.4 J-E characteristic of MOD TiO_2 films annealed at different temperatures

The frequency dependence of dielectric constant and loss tangent of the films in the microwave region of 100 Hz to 1 MHz measured using HP LCR Analyzer are plotted in Fig 5.5. For all films, the dielectric constant decreases with the increase in frequency. At certain frequency dielectric constant of the film starts to decrease sharply with the frequency. For the film annealed at 750 °C the dielectric constant drops off rapidly at lower frequency than the other three films. The dielectric constant of the films increases with the increase in annealing temperature. This observation is consistent with the formation of rutile phase of TiO₂ at high temperature which has much higher dielectric constant than TiO₂ in anatase form. The static dielectric constant of the film annealed at 950 °C has the highest value of ~72. However, there is no significant difference in the value of dielectric constants of the films annealed at 850 °C and 950 °C which are predominantly in rutile phase. It can be inferred that the dielectric constant remains almost independent of the annealing temperature after the formation of rutile phase. Dielectric loss data clearly shows that the relaxation frequency moves to > 1 MHz for films annealed at 850 °C and 950 °C compared to 750 °C annealed sample.

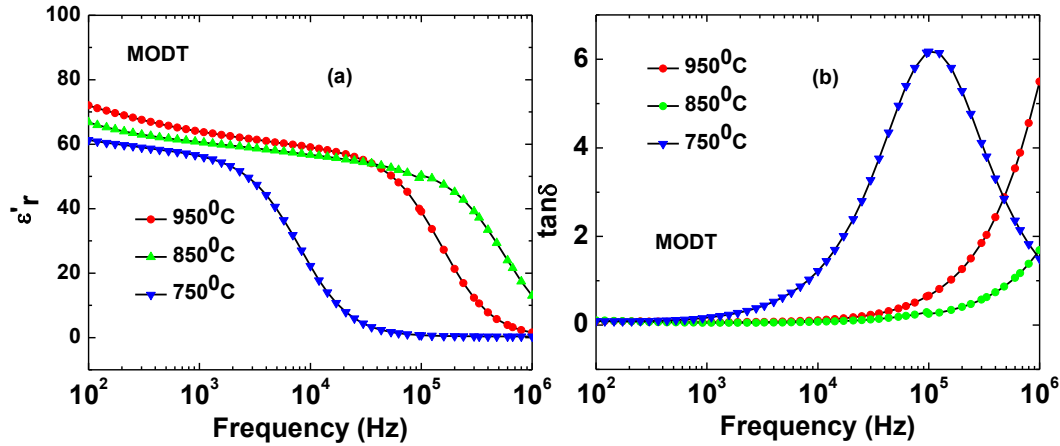


Figure 5.5 Frequency dependence of (a) dielectric constant and (b) loss tangent the films annealed at different temperatures

5.2 Zr-DOPED TiO₂ THIN FILMS

One way of improving the leakage current in TiO₂ is by doping with other transition elements. Studies have shown that the addition of proper amount of Zr can reduce the leakage current by almost one order of magnitude. The doping also helps to stabilize the dielectric constant and minimize the dielectric loss of the film. We have fabricated and studied the thin films of TiO₂ doped with Zr ~ 20% by atomic ratio.

The XRD and Raman spectra of Zr-doped films annealed at different temperatures are shown in Fig. 5.6. All peaks in XRD and Raman spectra correspond to the pure polycrystalline TiO₂ films. There are no detectable peaks corresponding to ZrO₂ in both XRD and Raman spectra which indicate that ZrO₂ could be in amorphous state. Films annealed at different temperatures show only

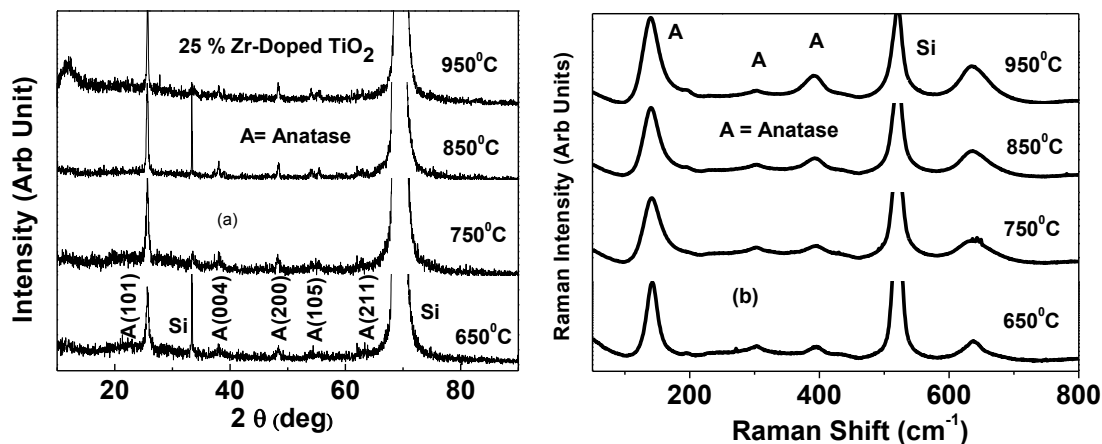


Figure 5.6 Plots of (a) XRD and (b) Raman spectra of Zr-doped films annealed at different temperature

anatase phase of TiO_2 . The higher intensity of (101) peak with respect to other (hkl) peak indicates an oriented growth of the film along the (101) direction. Since there are no peaks corresponding to the rutile structure, it can be concluded that 20% doping with Zr completely inhibits the phase transformation from anatase to rutile phase of TiO_2 films.

Figure 5.7 shows EDX measurement of the Zr-doped thin films, the composition of the Zr-doped TiO_2 . The typical concentrations of Zr and Ti in the films are approximately at 20 % and 80 at.%. The slight variation in the composition in different parts of the films indicates that Zr mixing with the TiO_2 may not be homogeneous.

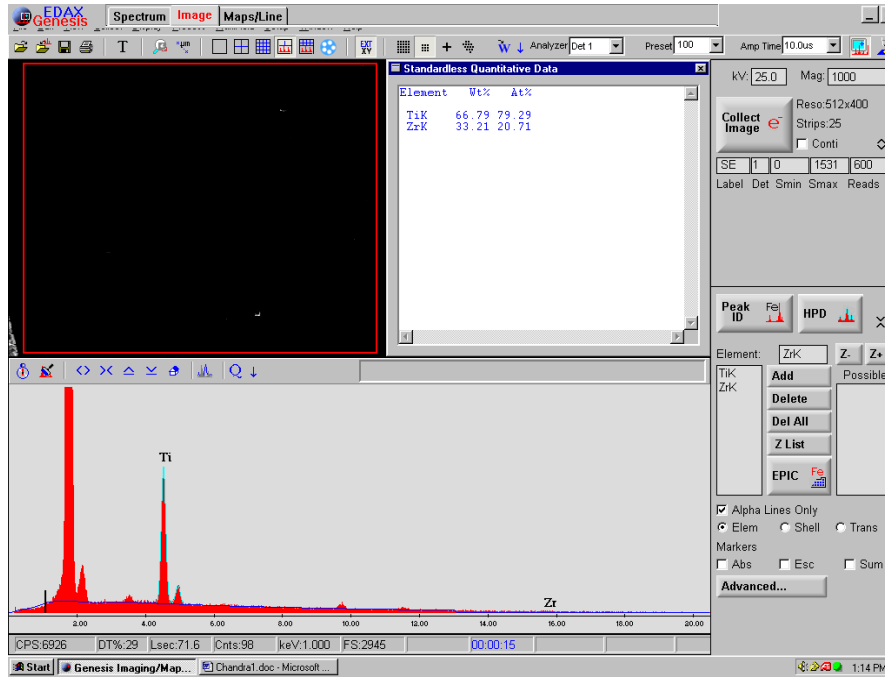


Figure 5.7 EDAX image of a Zr-doped TiO_2 film annealed at 950°C

Figure 5.8 shows I-V characteristics of Zr-doped TiO_2 films annealed at four different temperatures. Even though XRD and Raman measurements show that all the films have anatase phase the leakage currents are different. The films annealed at 650°C shows the highest leakage current of $\sim 10^{-4} \text{ A/cm}^2$ at 100 kV/cm and lowest breakdown strength of $\sim 100 \text{ kV/cm}$. Over all the magnitude of leakage currents are very similar to TiO_2 films without Zr-doping, however, with less asymmetry in forward and reverse bias especially in 950°C annealed sample.

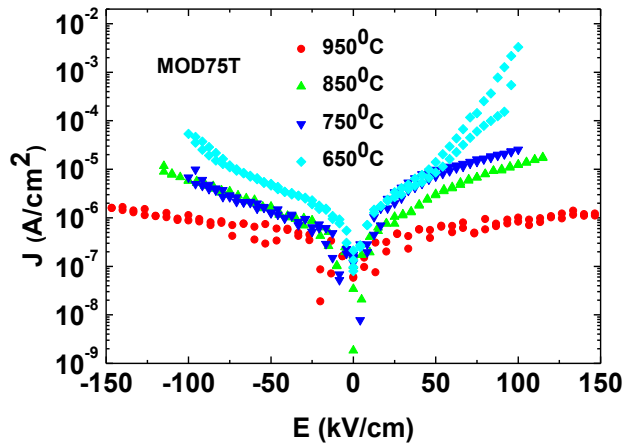


Figure 5.8 J-E curve of 25% Zr-doped MOD films annealed at different temperatures

As expected, the leakage current decreases with the increase in the annealing temperature and shows the lowest value of $\sim 10^{-6}$ A/cm² at the electric field 150 kV/cm for the films annealed at 950 °C. Since the leakage current and dielectric breakdown strength are comparable to the values of pure TiO₂ thin films annealed at the same 950 °C the Zr doping does not have much effect on these properties except in the 650 °C annealed sample in which one order of magnitude less leakage current was noted.

The frequency dependence of dielectric constant and loss tangent are shown in Fig 5.9. All films have almost similar values of dielectric constants of ~ 40 without significant variation (unlike TiO₂ films without Zr-doping) within the range of frequency measurements, except at very low frequency, perhaps, due to ohmic losses at the electrode/film interface. This value of dielectric constant is much higher than the dielectric constant of SiO₂ which is around 6. This behavior of

dielectric constant and the loss independent of annealing temperature makes it suitable as an insulator for the high-dielectric industries.

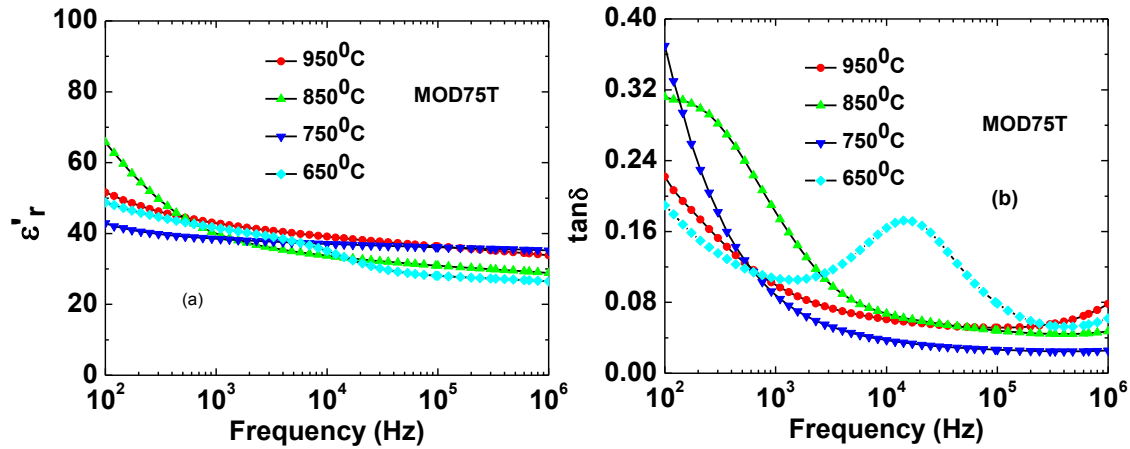


Figure 5.9 Frequency dependence of (a) dielectric constant (b) loss tangent of Zr-doped films annealed at different temperatures

5.3 SPUTTER DEPOSITED TiO_2 THIN FILMS

In general, the thin films prepared by MOD-spin coating method are of poor quality than the films prepared by sputter deposition. To make a comparison with a different deposition method, we present the electrical properties of TiO_2 thin films prepared by sputter deposition. The thickness of the sputter deposited films as measured from the cross sectional SEM was around 200 nm (Fig. 5.2). XRD and Raman spectra, Fig. 10 (a) and (b,) of the sputtered deposited films show sharp peaks with polycrystalline nature of the films. The film annealed at 650 °C has the anatase phase whereas the film annealed at 950 °C has the rutile phase. The films annealed at 750 °C and 850 °C are made of mixed phases of both anatase and rutile. While

MOD films did not show any preferred oriented growth the sputter deposited films show distinct oriented growth.

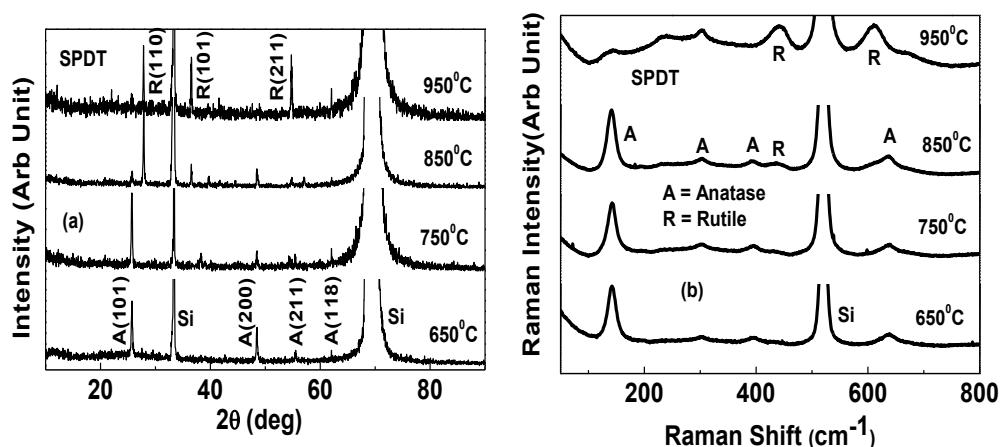


Figure 5.10 Plots of (a) XRD and (b) Raman spectra of sputtered deposited films annealed at different temperatures.

The relatively higher intensity of (101) anatase peak in the films annealed at 650 °C and 750 °C signify the oriented growth of these films along (101) direction. Similarly, the higher intensity of (110) rutile peak in the films annealed at 850 °C and 950 °C verifies the preferential growth of the rutile structure along the (110) direction. With the increase in annealing temperature from 650 °C to 950 °C the amount of anatase phase begin to decrease while the amount of rutile increases similar to the pure TiO₂ MOD films.

I-V characteristics of sputtered deposited films are shown in Fig 5.11. Leakage current decreases with the increase in annealing temperature similar to MOD prepared TiO₂ and Zr-doped TiO₂ films. Dielectric breakdown field of the film increases with the increase in annealing temperature and the films have a

minimum value of ~ 200 KV/cm. The film annealed at 950°C has the lowest leakage and highest dielectric breakdown field.

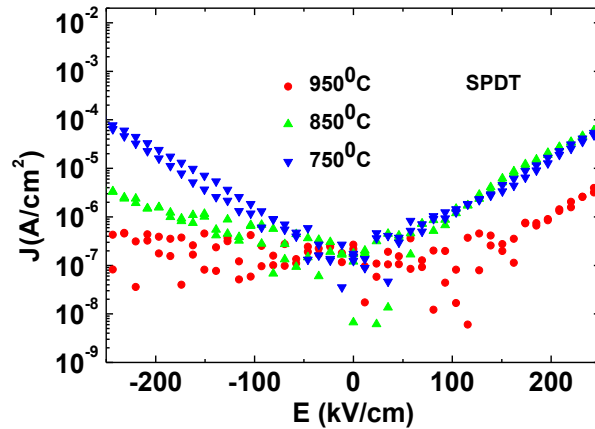


Figure 5.11 J-E characteristic of sputtered deposited films annealed at different temperatures.

The dependence of dielectric constant and loss tangent of the sputtered deposited films with respect to frequency in the range of 100 Hz to 1 MHz are shown in Fig. 5.12 (a) and (b). The dielectric constant decreases with the increase in frequency. The films annealed at 850°C shows the highest value of dielectric constant and lowest dielectric loss than the other films. The film annealed at 750°C has a lower relaxation frequency, while other two films have the relaxation > 1 MHz. The dielectric loss of the films improves with the increase in annealing temperature.

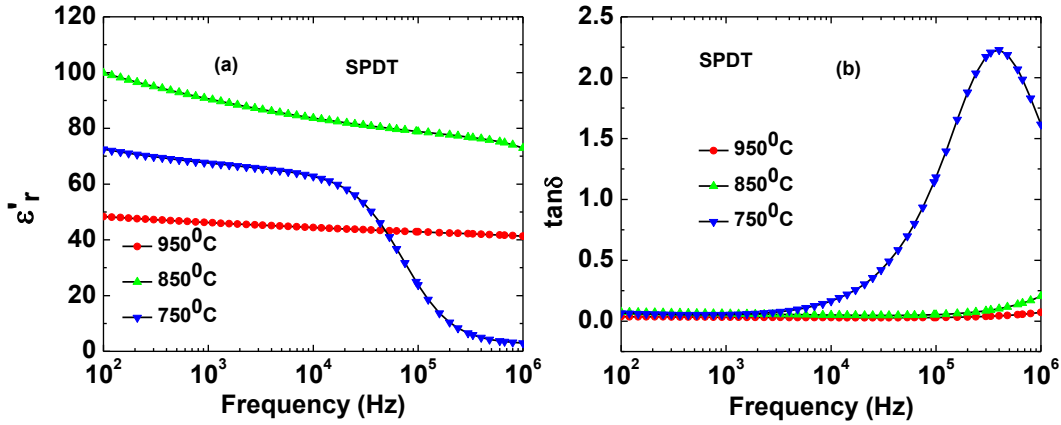


Figure 5.12 Frequency dependence of (a) dielectric loss and (b) loss tangent of sputtered deposited films annealed at different temperatures.

Figures 5.13 and 5.14 make a comparison of J-E as well as dielectric characteristics of three films annealed at 950 °C. It is observed that upon Zr-doping, MODT films show a flatter and lesser asymmetric J vs E curves, similar to SPDT films, although it does not show much improvement in leakage current.

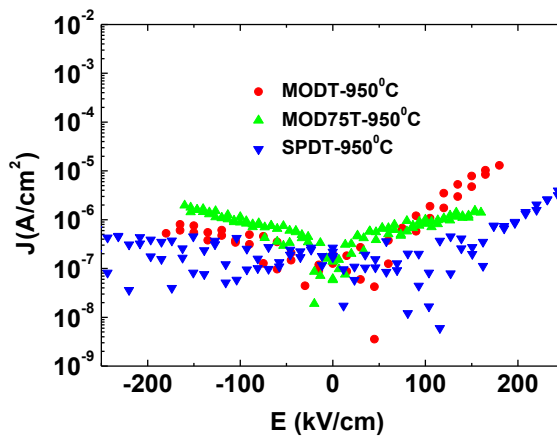


Figure 5.13 J-E characteristics of MODT, MOD75T and SPDT films annealed at 950 °C

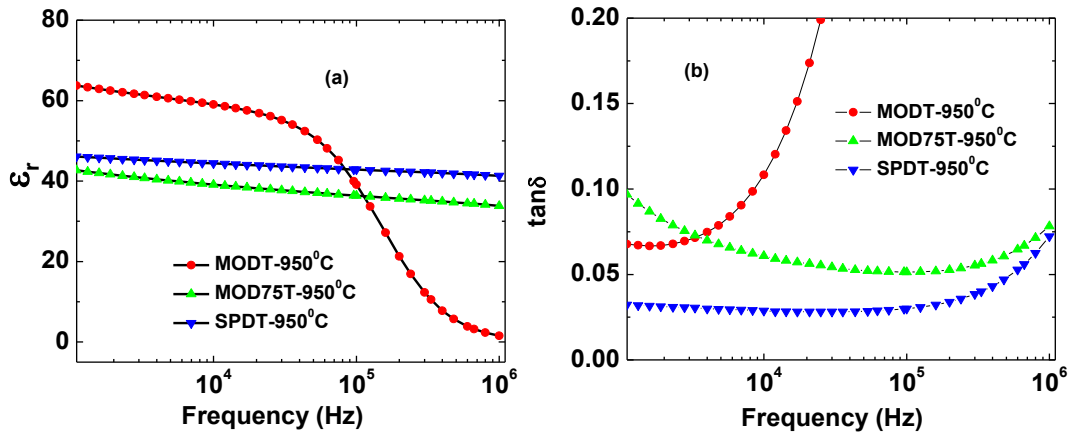


Figure 5.14 Plots of (a) dielectric constant and (b) loss tangent as a function of frequency for MODT, MOD75T and SPDT films annealed at 950 °C

It is also interesting to see that the lowest value of electric breakdown field of all three set of films increases with the increase in annealing temperature as shown in the Fig. 5.15. The breakdown field of MODT and MOD75T are very similar, whereas the SPDT films have slightly higher values. The higher value of electric breakdown strength in the SPDT films could be due to higher degree of crystallinity and lower level of defects in the films. The increase in the electric breakdown field due to annealing temperature is attributed to the higher order of crystallinity and the removal of defects at higher annealing temperatures.

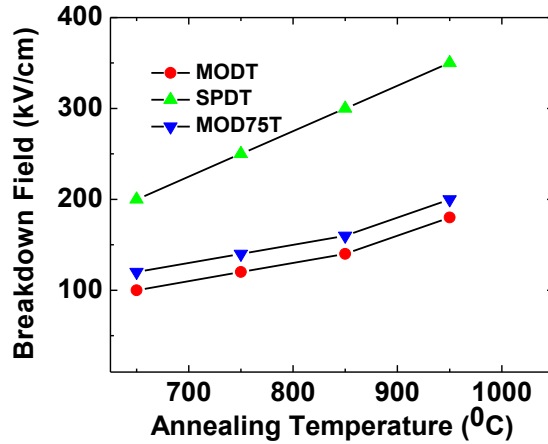


Figure 5.15 Variation in the dielectric breakdown field of the films with annealing temperatures within the region of measurements

5.4 CONDUCTION MECHANISM IN TiO₂ THIN FILMS

The I-V characteristics for the three set of films, undoped TiO₂ MOD thin films, Zr doped TiO₂ MOD thin films and RF magnetron sputtered TiO₂ thin films, annealed under different temperatures were analyzed to understand the conduction mechanism in these samples. All films under investigation are sufficiently thick enough to rule out the electrode limited tunneling processes. Various studies have shown that Schottky emission conduction (electrode limited) in TiO₂ based films is a dominant phenomenon in lower electric field region [186]. However, our data in the lower electric field region are very much scattered making it difficult to discern the magnitude of Schottky emission conduction in our films. To confirm the degree of Schottky emission, temperature dependent measurements are necessary which are lacking in our investigation. We, thus, focused mainly on bulk limited current

conduction mechanisms, mainly the space charge limited current (SCLC) conduction and Poole-Frenkel (PF) conduction. We utilized the $\ln(J)$ Vs $\ln(E)$ plots for the SPLC and $\ln(J/E)$ Vs $E^{1/2}$ plots for the PF conduction mechanism analysis.

SPACE-CHARGE LIMITED CONDUCTION

The plots of $\ln(J)$ Vs $\ln(E)$ for all three sets of films annealed at different temperatures are shown in Fig. 5.16. All films show two distinct straight lines with different slopes, one in lower electric field region and another in the higher electric field region. The straight line in the lower electric field region for these films is probably due to ohmic type of conduction. In the low field region, the slope of $\ln(J)$ Vs $\ln(E)$ curves vary between 1 and 2 for most of the samples, indicating that space charge limited current in this region is mainly trap free (ohmic) or discrete trap assisted. We also do not see any systematic annealing temperature dependence, which indicates that local defects are more dominating reflecting in this random behavior at high field regions, the slope of $\ln(J)$ Vs $\ln(E)$ curves is always greater than 2 and in some cases it is as high as ~ 5 (see Table 5.1), indicating that traps may be distributed within the bandgap of the material and the conduction mechanism may be more temperature dependent which are lacking in this investigation.

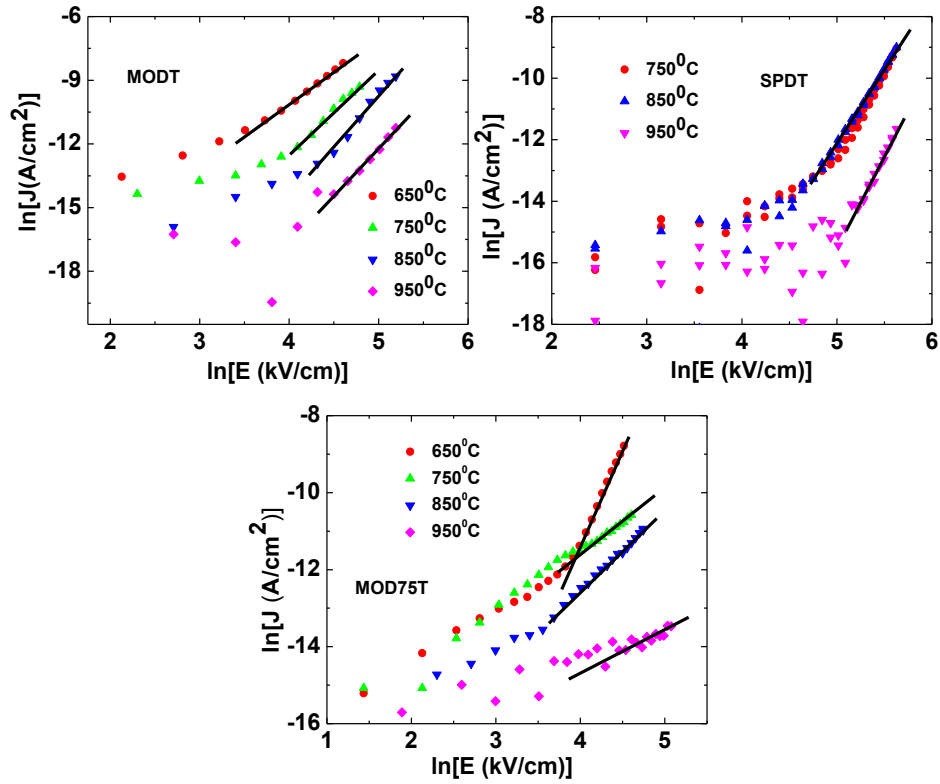


Figure 5.16 Plots of $\ln(J)$ Vs $\ln(E)$ of three sets of films annealed at different temperatures.

Table 5.1 Slopes of SCLC plots (High Field region)

Annealing Temp.	Slope(High Field Region)		
	MODT	SPDT	MOD75T
950 °C	4.5	4.9	0.6
850 °C	5.7	4.6	2.07
750 °C	4.3	5.8	1.53
650 °C	3.2	-	4.93

Since the space charge formation is connected to the free charges inside the films or charges in the shallow trap regions, both MODT and SPDT films seem to contain higher degree of defects that contribute to the formation of space-charge in

these films. The plots of Zr-doped films also show distinct linear behavior in both lower and higher electric field regions. At higher fields, it is interesting to note that only 650 °C annealed film has a slope higher than 2 (higher level of trapped defects), whereas other three samples have slopes smaller than 2 indicating that the dominant mechanism could be due to discrete traps.

POOLE-FRENKEL (PF) CONDUCTION ANALYSIS

The PF plots, $\ln(J/E)$ vs $E^{1/2}$ of all three sets of films are shown in Fig 5.17. Many previous studies have shown dominance of PF conduction in TiO₂ based films in the higher electric field region [187]. So the straight line nature of the curves in the higher electric field region should indicate the presence of PF conduction in the films. The value of high field slope of these curves fluctuates around $\sim 0.7 \sqrt{10^{-3}}$ (cm/V)^{1/2}, except for Zr-doped films annealed at 750-950 °C (see Table 5.2). We used this slope to extract the high frequency dielectric constant using $\xi = 1$ in Eq. 2.24. The calculated value of dynamic dielectric constant ϵ using the observed slope is 1.76 for $\xi = 1$. This value will be shown to be very close to the value extracted from Cole-Cole plot analysis of the frequency dependent dielectric data in the next section.

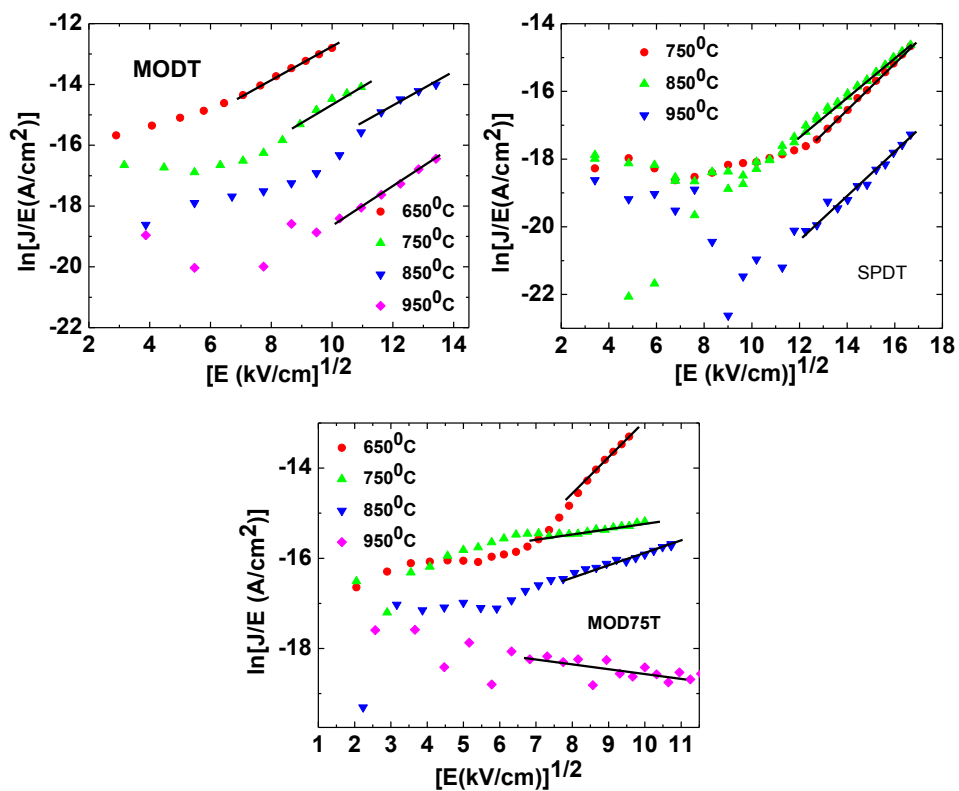


Figure 5.17 Plots of $\ln(J/E)$ Vs $E^{1/2}$ of three sets of films annealed at different temperatures.

Table 5.2 Slopes of PF plots (High Field region)

Annealing Temp.	Slope(High Field Region)		
	$\sqrt{10^{-3}} \text{ (cm/V)}^{1/2}$		
	MODT	SPDT	MOD75T
950°C	0.68	0.7	-0.12
850°C	0.51	0.84	0.26
750°C	0.59	0.69	0.14
650°C	0.52	-	0.9

From the various types of conduction mechanism analysis we conclude that MODT and SPDT exhibit both types of conduction mechanism: SPLC as well as PF conduction. The Zr-doped films annealed at 750-950 °C however do not exhibit either space-charge limited or Poole-Frenkel conduction mechanism indicating that the dominant conduction mechanism in this film could be of Schottky type which has to be further confirmed from temperature dependent measurements. The temperature dependent measurements are necessary to clearly distinguish between Schottky emission and P-F conduction.

5.5 COLE-COLE ANALYSIS OF DIELECTRIC DATA

Cole-Cole analysis of frequency dependent complex dielectric data provides information on various kinds of relaxation phenomena as well as the static and dynamic dielectric constants which are crucial for device fabrication in microelectronics. The Cole-Cole analyses (described in section 2.7) were performed on three sets of films in the range of 100 Hz - 1 MHz (limited range available in our measuring instrument) to determine relaxation time (τ), static and high frequency dielectric constant. For example, Fig. 5.18 shows Cole-Cole plots of 750 °C annealed films and the corresponding fitting of real imaginary part of dielectric data using Eq. 2.30 are shown Fig. 5.19. Table 5.3 shows the corresponding fitting parameters used in the analysis for all the films.

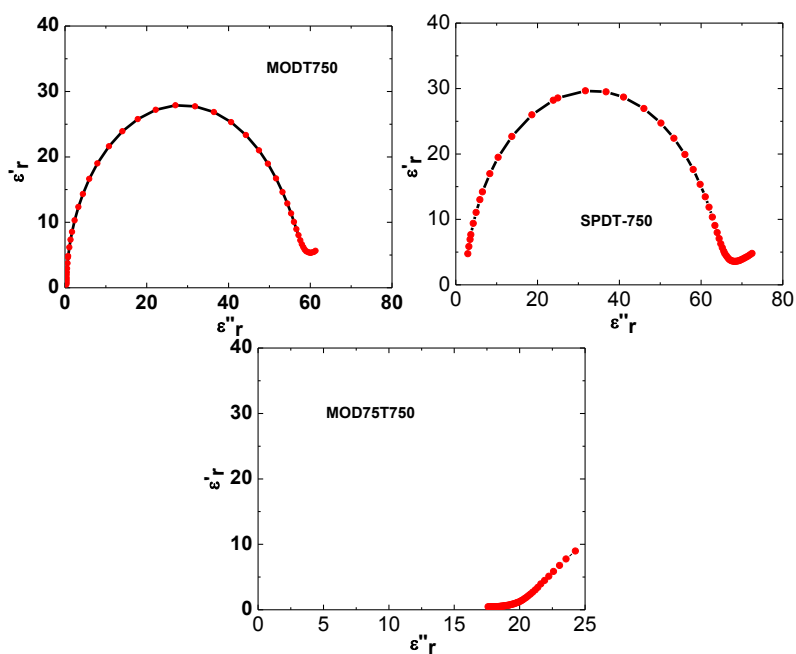


Figure 5.18 Cole-Cole plots of films annealed at 750°C

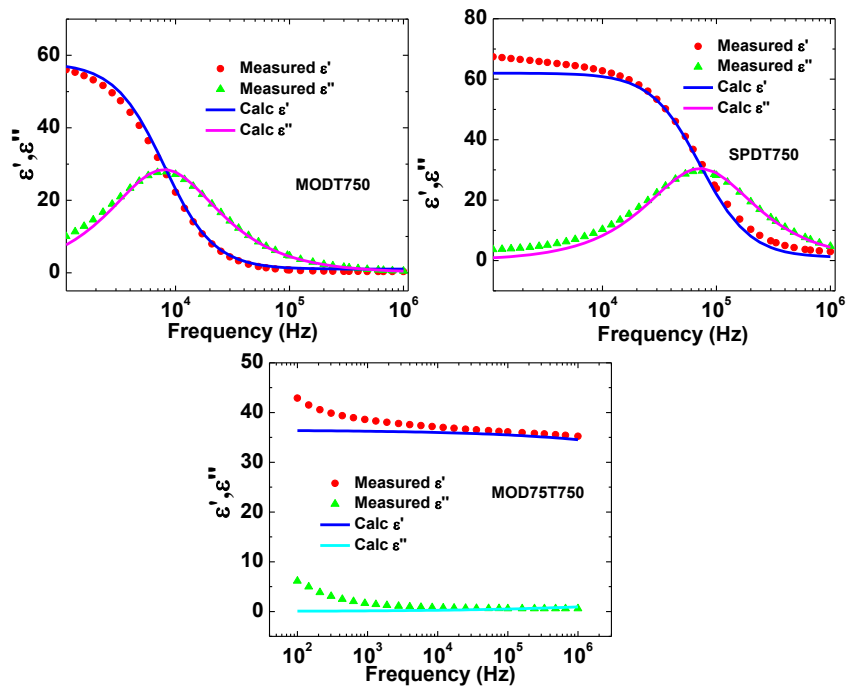


Figure 5.19 Real and imaginary dielectric constants for films annealed at 750 °C, symbols (experimental) and solid lines (fitted)

Table 5.3 Fitting parameters for Cole-Cole analysis of dielectric data

Films	ϵ_s	ϵ_∞	$\tau(s)$	α
MODT750	58	2.0	2.0×10^{-5}	0
MODT850	55	2.0	3.0×10^{-7}	0
MODT950	58	2.0	1.0×10^{-6}	0
MOD75T750	37	2.0	1×10^{-10}	0.7
MOD75T850	36	2.0	5×10^{-9}	0.7
MOD75T950	40	2.0	1×10^{-9}	0.7
SPDT750	62	2.5	2.0×10^{-6}	0
SPDT850	76	2.5	4×10^{-8}	0
SPDT950	43	2.5	1.5×10^{-9}	0.4

It is interesting to note that the static dielectric constant does not show much variation with annealing temperature in MOD prepared films except that Zr-doping reduces the value from ~ 56 to ~ 38 . However, the relaxation time decreases by more than three orders of magnitude upon Zr-doping. The need for fitting parameter α for Zr-doped samples shows that there is a distribution of relaxation time. Furthermore, annealing of films at higher temperatures consistently move the relaxation frequency to higher values. This is in agreement with the observation of lowest leakage current for samples annealed at 950 °C. Within our limited study we could infer that Zr-doping could be suitable for high frequency applications in microelectronic devices, perhaps due to stabilization of TiO₂ in anatase phase.

The need for fitting parameter α for Zr-doped samples shows that there is a distribution of relaxation time. Furthermore, annealing of films at higher temperatures consistently move the relaxation frequency to higher values. This is in agreement with the observation of lowest leakage current for samples annealed at 950°C. Within our limited study we could infer that Zr-doping could be suitable for high frequency applications in microelectronic devices, perhaps due to stabilization of TiO₂ in anatase phase.

Chapter 6

SUMMARY AND CONCLUSIONS

The properties of many transition metal oxide thin films can be drastically manipulated and even new properties can be created by engineering the microstructure and composition, which makes the study of these materials ever challenging and exciting. The focus of this thesis was to study the structure-property correlation in thin films of V_2O_5 and TiO_2 based transition metal oxides as functional materials.

V_2O_5 AS A CATHODE MATERIAL FOR Li-ION BATTERY

Vanadium based oxide materials are being explored as future cathode materials for Li-ion battery. Among the various vanadium oxides, vanadium pentoxide (V_2O_5) is more interesting due to a number of factors such as it is cheaper, easy to prepare, higher stability window, higher capacity etc. V_2O_5 thin films were prepared by spin coating technique using three different types of precursors: MOD, sol-gel organic and sol-gel inorganic precursor. The films were characterized using various techniques such as XRD, Raman, UV/Vis, cyclic voltammetry (CV) measurement etc. The film prepared from MOD precursor contains highest degree of non-stoichiometry, as confirmed from Raman, UV/Vis and HRTEM, and possesses highest value of capacity ~ 130 mAh/g, which is slightly smaller than the theoretical value of 148 mAh/g for the polycrystalline V_2O_5 film. The highest degree of non-

stoichiometry in the MOD film arises from the highest amount of carbon content in the MOD precursor. We confirm that the degree of non-stoichiometry is crucial for the optimal value of capacity. The diffusion coefficient of the order of $\sim 10^{-9}$ cm²/s is a maximum for MOD films, which is higher by about two order of magnitude than the reported value of $\sim 10^{-11}$ cm²/s in pure TiO₂ film prepared by using different method of preparations.

One way of improving the electrochemical performance is by doping transition metal oxides. For e.g. capacity of the V₂O₅ can be improved by doping suitable metal oxides such as TiO₂. We prepared 5% to 30% Ti-doped thin films using MOD and sol-gel precursor. The degree of nonstoichiometry increases with the increase in the amount of Ti-doping in both MOD and sol-gel (VOSG) films. However, the capacity increased only in 5% Ti-doped VOSG film while it decreased in other MOD and sol-gel films. This can be attributed to the optimal degree of non-stoichiometry in 5% Ti-doped film. This indicates controlling the degree of stoichiometry in the film is crucial for the optimal performance.

Various studies have shown that the highest capacity of ~ 780 mAh/g can be achieved for the aerogel and 560 mAh/g for xerogel V₂O₅ films. But aerogel/xerogel form is vulnerable in crystal stability and capacity degrades very rapidly during successive charging/discharging. Doping or coating with other transition metal oxides can also lead to higher value of capacity and cyclic stability. We have not measured the cyclic stability in our films which is crucial for its usability as a cathode material. A detailed study of its cyclic performance and its optimization is

very important. Since part of the degree of non-stoichiometry is the result of multiple oxidation of vanadium oxide, it is also important to measure the ratios of different oxidation states of vanadium which can lead to a better understanding of the degree of nonstoichiometry and to control and modify for the optimal performance. Vacuum annealing or annealing in the partial pressure of oxygen is another possible way of modifying the degree of non-stoichiometry. In addition, the problem of low electronic conductivity of V_2O_5 can be improved by suitably coating conducting material. There is still a lot to be done before V_2O_5 based thin films are realized as a future cathode material.

TiO₂ AS A HIGH DIELECTRIC MATERIAL

TiO₂ is an excellent candidate for use as a high-k dielectric material because of its very high dielectric constant and high electric breakdown of ~ 4 MV/cm. One problem to employ TiO₂ as a high-k dielectric is its higher leakage current density which is above the threshold value $\sim 10^{-6}$ A/cm² of high-k industry requirement. TiO₂ exists in two thermodynamical phases: anatase and rutile. Many high-k dielectric parameters such as dielectric constant and leakage current density depend on the structural phase of the material. It is crucial to stabilize the phase of TiO₂ to minimize the fluctuation of dielectric constant and leakage current with temperature. Proper doping with suitable transitional metal oxide can inhibit phase transformation of TiO₂. We have successfully prepared and characterized single phase TiO₂ over a wide range of temperature from 650 °C to 950 °C.

TiO₂ and 25% Zr-doped TiO₂ films were prepared by spin coating using MOD precursors. In addition TiO₂ films were also prepared using sputter deposition technique to compare the results with the pure TiO₂ films prepared from MOD. All films were characterized using Raman, XRD, I-V measurement and frequency dependence of dielectric response in the range of 100 Hz-1MHz. Dielectric constant and loss improves with increase in annealing temperature in all three set of films. Similarly, the leakage current density improves almost by one order of magnitude for every 100 °C increase in annealing temperature, in all three sets. There is no appreciable difference in leakage current and dielectric constant of MOD TiO₂ and sol-gel TiO₂ films. While there is a phase change, as determined by Raman and XRD, in pure MOD and sol-gel film with an increase in annealing temperature, there is no phase change in Zr-doped film. This indicates that 25% Zr-doping completely inhibits phase transformation of TiO₂. All Zr-doped TiO₂ films exhibit anatase phase, independent of annealing temperature. However, the films annealed at 950 °C exhibits the best overall performance in term of leakage current density and electric breakdown strength among all Zr-doped films. The dielectric constant of the films, however, does not show any variation due to different annealing temperature. There is no appreciable improvement in leakage current due to Zr-doping. However, the rate of increase in leakage current density with the increase in electric field is lower in Zr-doped TiO₂ films and this is a crucial parameter for high-k dielectric.

REFERENCES

- [1]. Web Elements (www.webelements.com)
- [2]. National Renewable Energy Laboratory, Golden, CO 80401-3393, USA, *Solar Energy Materials & Solar Cells*, **88** (2005) 1–10
- [3]. N. Takahashi, A. Suda, I. Hachisuka, M. Sugiura, H. Sobukawa, H. Shinjoh, *Applied Catalysis B: Environmental*, **72** (2007) 187–195
- [4]. Z.G. Wei, C.Y. Tang, W.B. Lee, L.S. Cui, D.Z. Yang, *Materials Letters*, **32** (1997) 3 13-3 17
- [5]. C-Wei Liu, C-L Cheng, J-T Jeng, B-T Dai, S-W Huang, *Microelectronic Engineering*, **85** (2008) 1766–1771
- [6]. J. M. Tarascon and M. Armand, *Nature (London)*, **414** (2001) 359
- [7]. A. Manthiram and J. Kim, *Chem. Matter*, **10** (1998) 2895
- [8]. Y.J. Park, J.G. Kim, M.K. Kim, H.T. Chung, W.S. Um, M.H. Kim, H.G. Kim, *Journal of Power Sources*, **76** (1998) 41–47
- [9]. M. Higuchi, K. Katayama, Y. Azuma, M. Yukawa, M. Suhara, *Journal of Power Sources*, **119** (2003) 258–261
- [10]. M. Wu, Q. Zhang, H. Lu, A. Chen, *Solid State Ionics*, **169** (2004) 47–50
- [11]. S-T Myung, S. Komaba, N. Kumagai, *Electrochimica Acta*, **47** (2002) 3287-3295

- [12]. S. Venkatraman, V. Subramanian, S. Gopu Kumar, N.G. Renganathan, N. Muniyandi, *Electrochemistry Communications*, **2** (2000) 18–22
- [13]. Z-F Huang, C-Z Wang, X. Meng, D-P Wang, G. Chen, *Journal of Solid State Chemistry*, **179** (2006) 1602–1609
- [14]. L. Herna´n, J. Morales, L. Sa´nchez, J. Santos, *Solid State Ionics*, **118** (1999) 179–185
- [15]. Y.K. Yoon, C.W. Park, H.Y. Ahn, D.H. Kim, Y.S. Lee, J. Kim, *Journal of Physics and Chemistry of Solids*, **68** (2007) 780–784
- [16]. T. Tsuji, H. Umakoshi, Y. Yamamura, *Journal of Physics and Chemistry of Solids*, **66** (2005) 283–287
- [17]. Z.P. Guo, S. Zhong, G.X. Wang, H.K. Liu, S.X. Dou, *Journal of Alloys and Compounds*, **348** (2003) 231–235
- [18]. C. Li, H.P. Zhang, L.J. Fu, H. Liu, Y.P. Wu, E. Rahm, R. Holze, H.Q. Wu, *Electrochimica Acta*, **51** (2006) 3872–3883
- [19]. M. Wu, Q. Zhang, H. Lu, A. Chen, *Solid State Ionics*, **169** (2004) 47–50
- [20]. Y.J. Park, J.G. Kim, M.K. Kim, H.T. Chung, W.S. Um, M.H. Kim, H.G. Kim, *Journal of Power Sources*, **76** (1998) 41–47
- [21]. S-H Wu, M-T Yu, *Journal of Power Sources*, **165** (2007) 660–665
- [22]. Y.K. Yoon, C.W. Park, H.Y. Ahn, D.H. Kim, Y.S. Lee, J. Kim, *Journal of Physics and Chemistry of Solids*, **68** (2007) 780–784

- [23]. G.X. Wang, Steve Bewlay, Jane Yao, Y. Chen, Z.P. Guo, H.K. Liu, S.X. Dou, *Journal of Power Sources*, **119–121** (2003) 189–194
- [24]. C. Li, H.P. Zhang, L.J. Fu, H. Liu, Y.P. Wu, E. Rahm, R. Holze, H.Q. Wu, *Electrochimica Acta*, **51** (2006) 3872–3883
- [25]. S.J. Kwon, C.W. Kim, W. T. Jeong, K.S.B. Lee, *Journal of Power Sources*, **137** (2004) 93–99
- [26]. Z-R. Chang, H-J. Lu, H.-W. Tang, H-J. Li, X-Z Yuan, H. Wang, *Electrochimica Acta*, **54** (2009) 4595–4599
- [27]. B. Zhao, Y. Jiang, H. Zhang, H. Tao, M. Zhong, Z. Jiao, *Journal of Power Sources*, **189** (2009) 462–466
- [28]. G.X. Wang, S. Needham, J. Yao, J.Z. Wang, R.S. Liu, H.K. Liu, *Journal of Power Sources*, **159** (2006) 282–286
- [29]. P. Balog, D. Orosel, Z. Cancarevic, C. Schön, M. Jansen, *Journal of Alloys and Compounds*, **429** (2007) 87–98
- [30]. J. Haber, M. Witko and R. Tokarz, *Applied Catalysis A General* **157**, 3, (1997)
- [31]. R.T. Rajendra Kumar, B. Karunagaran, V. Senthil Kumar, Y.L. Jeyachandran, D. Mangalaraj, Sa. K. Narayandass, *Materials Science in Semiconductor Processing*, **6** (2003) 543–546
- [32]. S. Koike, T. F., T. Sakai, S. Higuchi, *Journal of Power Sources*, **81–82** (1999) 581–584

- [33]. C. Julien, E. Haro-Poniatowski, M.A. Camacho-Lo'pez, L. Escobar-Alarcin J. Jimenez-Jarquín, *Materials Science and Engineering B*, **65** (1999) 170–176
- [34]. H. Groult, K. Le Vana, A. Mantoux, L. Perrigaud, P. Doppelt, *Journal of Power Sources*, **174** (2007) 312–320
- [35]. F. Coustier, Jong-Min Lee, S. Passerini, W. H. Smyrl, *Solid State Ionics*, **116** (1999) 279–291
- [36]. F. Coustier, G. Jarero, S. Passerini, W. H. Smyrl, *Journal of Power Sources*, **83** (1999) 9–14
- [37]. G.N. Kryukova, G.A. Zenkovets, N. Pfnder, D.S. Su, R. Schlogl, *Materials Science and Engineering A*, **343** (2003) 8-12
- [38]. Y-M Li, M. Hibino, Y. Tanaka, Y. Wada, Y. Noguchi, S. Takano, T. Kudo, *Solid State Ionics*, **143** (2001)67–72
- [39]. S.Y. Zhan, C.Z. Wang, K. Nikolowski, H. Ehrenberg, G. Chen, Y.J. Wei, *Solid State Ionics*, **180** (2009) 1198–1203
- [40]. C. Navone, R. Baddour-Hadjean, J.P. Pereira-Ramos, R. Salot, *Electrochimica Acta*, **53** (2008) 3329–3336
- [41]. S. Koike, T. Fujieda, T. Sakai, S. Higuchi, *Journal of Power Sources*, **81–82** (1999) 581–584
- [42]. Y. J. Park, K. S. Ryu, K. M. Kim, N-G Park, M.G. Kang, S.H. Chang, *Solid State Ionics*, **154–155** (2002) 229– 235

- [43]. R. Baddour-Hadjean, C. Navone, J.P. Pereira-Ramos, *Electrochimica Acta*, **54** (2009) 6674–6679
- [44]. J.M. McGrawb, J.D. Perkinsa, J.-G. Zhanga, P. Liua, P.A. Parillaa, J. Turnera, D.L. chulz C.J. Curtis , D.S. Ginley, *Solid State Ionics*, **113–115** (1998) 407–413
- [45]. W. Wu, Y.Wang, X. Wang, Q. Chen, X. Wang, S. Yang, X. Liu, J. Guo, Z. Yang, *Journal of Alloys and Compounds*, **486** (2009) 93–96
- [46]. Y. Chen, H. Liu and W-L. Ye, *Scripta Materialia*, **59** (2008) 372– 375
- [47]. W. D. Brown, and W.W. Granneman,, *Solid State Electronics*, **21** (1978) 837
- [48]. M. L. Green, P. K. Schenck, K.-S. Chang, J. Ruglovsky, M. Vaudin, *Microelectronic Engineering*, **86** (2009) 1662–1664
- [49]. A. Templeton, X. Wang, S.J. Penn, S.J. Webb, L.F. Cohen and N.M. Alford Microwave dielectric loss of titanium oxide. *J. Am. Ceram. Soc.*, **83** (2000) 95–100.
- [50]. R. Paily, A. Das Gupta, N. Das Gupta, P. Bhattacharya, P. Misra, T. Ganguli , L.M. Kukreja, A.K. Balamurugan, S. Rajagopalan and A.K. Tyagi, 2002, *Appl. Surf. Sci.*, **187** 297–304
- [51]. M. Houssa, L. Pantisano, L.-A., Ragnarsson, R. Degraeve, T. Sharma, G. Pourtois S. De Gendt, G. Groeseneken M.M. Heyns, *Material Science & Engineering, R*, **51** (2006) 37

- [52]. M.K. Bera, C.K. Maiti, *Materials Science in Semiconductor Processing*, **9** (2006) 909–917
- [53]. M.L. Green, P.K. Schenck, K.-S. Chang, J. Ruglovsky, M. Vaudin, *Microelectronic Engineering*, **86** (2009) 16-62-1664
- [54]. Q. Lu, D. Park, A. Kalnitsky, C. Chang, C.-C. Cheng, S.P., Tay, T.-J. King, C. Hu, *IEEE ED Lett.*, **19** (1998) 341
- [55]. S.A. Campbell, D.C. Gilmer, X. Wang, M. Hsieh, H.S. Kim, W.L. Gladfelter, *IEEE Trans Electron Dev*, **43** (1999) 383-392
- [56]. G. Lucovsky, G. B. Rayner Jr., Y. Zhang, C. C. Fulton, R. J. Nemanich, G. Appel, H. Ade, J. L. Whitten, *Applied Surface Science*, **212–213** (2003) 563–569
- [57]. H. Hu, C. Zhu, X. Yu, A. Chin, M.F. Li, B.J. Cho, D.-L. Kwong, P.D. FOO, M.B. Yu, X. Liu, J. Winkler, *IEEE Electron Device Lett.*, **24** (2003) 60
- [58]. S.-J. Ding, H. Hu, C. Zhu, S.J. Kim, X. Yu, M.-F. Li, B.J. Cho, D.S.H. Chan, M.B. Yu, S.C. Rustagi, A. Chin, D.-L. Kwong, *IEEE Trans. Electron Devices*, **51** (2004) 886
- [59]. C. Lin, J. Kang, D. Han, D. Tian, W. Wang, J. Zhang, M. Liu, X. Liu, R. Han, *Microelectronic Engineering*, **66** (2003) 830–834
- [60]. L. Shi, Y. Yuan, X.F. Liang, Y.D. Xia, J. Yin, Z.G. Liu, *Applied Surface Science*, **253** (2007) 3731–3735
- [61]. R. M. Wallace, *Applied Surface Science*, **231–232** (2004) 543–551

- [62]. J.A. Kittl, K. Opsomer, M. Popovici, N. Menou, B. Kaczer, X.P. Wang, C. Adelman, M.A. Pawlak et.al, *Microelectronic Engineering*, **86** (2009) 1789–1795
- [63]. D.-O. Lee, P. Roman, C.-T. Wu, P. Mumbauer, M. Brubaker, R. Grant, J. Ruzyllo, *Solid-State Electronics*, **46** (2002) 1671–1677
- [64]. K. Iwamoto, W. Mizubayashi, A. Ogawa, T. Nabatame, H. Satake, A. Toriumi, *Solid-State Electronics*, **50** (2006) 999–1003
- [65]. P.F. Lee, J.Y. Dai, H.L.W. Chan, C.L. Choy, *Ceramics International*, **30** (2004) 1267–1270
- [66]. F. Chen, X. Bin, C. Hella, X. Shi, W.L. Gladfelter, S.A. Campbell, *Microelectronic Engineering*, **72** (2004) 263–266
- [67]. G. He, Q. Fanga, L.D. Zhang, *Materials Science in Semiconductor Processing*, **9** (2006) 870–875
- [68]. W. Liu, X.Su, S. Zhang, H. Wang, J. Liu, L. Yan, *Vacuum*, **82** (2008) 1280–1284
- [69]. C.K. Maiti, G.K. Dalapati, S. Chatterjee, S.K. Samanta, S. Varma, S. Patil, *Solid-State Electronics*, **48** (2004) 2235–2241
- [70]. M.K. Bera, C. Mahata, C.K. Maiti, *Materials Science in Semiconductor Processing*, **11** (2008) 254–258
- [71]. R. Sohal, G. Lupina, O. Seifarth, P. Zaumseil, C. Walczyk, T. Schroeder, *Surface Science*, **604** (2010) 276–282

- [72]. E. Atanassova, A. Paskaleva, *Microelectronics Reliability*, **47** (2007) 913–923
- [73]. M.K. Bera, C.K. Maiti, *Materials Science in Semiconductor Processing*, **9** (2006) 909–917
- [74]. S. Kim, M. Ham, J. Lee, W. Lee, J. Myoung, *Applied Surface Science*, **254** (2008) 3943–3948
- [75]. M. D. Stamate, *Thin Solid Films*, **372** (2000) 246–249
- [76]. K.C. Yang, P. Shen, D. Gan, *Journal of Solid State Chemistry*, **179** (2006) 3478–348
- [77]. B. Gao, T. M. Lim, D. P. Subagio, T. Lim, *Applied Catalysis A: General*, **375** (2010) 107–115
- [78]. D.J. Reidy, J.D. Holmes, M.A. Morris, *Journal of the European Ceramic Society*, **26** (2006) 1527–1534
- [79]. T. Shih, T. Huang, Y. Luo, S. Lan, K. Chiu, *Journal of Crystal Growth*, **280** (2005) 442–447
- [80]. J.K. Choi, H.J. Kim, B.H. Jun, C.J. Kim, *Physica C*, **426–431** (2005) 920–925
- [81]. K. Nieh, J.N. Matossian, F.G. Krajenbrink, *Plasma-Enhanced, Magnetron-sputtered Deposition (PMD) of Materials*, U.S. Patent No. 5,346,600 (1994)
- [82]. D.R.G. Mitchell, D.J. Attard, G. Triani, *Journal of Crystal Growth*, **285** (2005) 208–214

- [83]. Y. Homma, J. Osaka and N. Inoue, *Jpn. J. Appl. Physics*, **33** (1994) 563-566
- [84]. J.D. Wright, Nico A, J.M. Sommerdijk, *Sol-Gel Materials: Chemistry and Applications*
- [85]. T. Ishibashi, Mizusawa, N. Togashi, T. Mogi, M. Houchido and K. Sato, *Journal of Crystal Growth*, **275** (2005) 2427–2431
- [86]. C. J. Brinker and G. W. Scherer, *Sol-Gel Science - The Physics and Chemistry of Sol-Gel Processing*, New York, Academic Press, 1990
- [87]. http://commons.wikimedia.org/wiki/File:Bragg_diffraction.png
- [88]. http://www.mpip-mainz.mpg.de/~andrienk/journal_club/xray.pdf
- [89]. http://www.ccmr.cornell.edu/igert/modular/docs/Raman_Scattering.pdf
- [90]. K. Oe and Y. Toyoshiman, *J. Non-Cryst. Solids*, **58** (1973) 304
- [91]. P. M. S. Monk, *Fundamental of Electroanalytical Chemistry*, Wiley Publication
- [92]. S. Chakraborty, M.K. Bera, S. Bhattacharya, C.K. Maiti, *Microelectronic Engineering*, **81** (2005) 188–193
- [93]. Y. L. Chiou, J. P. Gambino, M. Mohammad, *Solid State Electronics*, **45** (2001) 1787-1791
- [94]. J. G. Simmons, *J. Phys. D: Appl. Phys.*, **4** (1971) 613-657
- [95]. R. Sathyamoorthy, J. Dheepa, S. Velumani, *Materials Characterization*, **58** (2007) 842–846
- [96]. G. Barbero 1, I. Lelidis, *Physics Letters A*, **372** (2008) 2079–2085

- [97]. J. S. Hwang, Y. T. Al-Janabi, *Spectrochimica Acta*, **56** (2000) 273–284
- [98]. S. Havriliak, S. Negami, *J Polym Sci. C*, **14** (1966)14-99
- [99]. V.I. Parvulescu, S. Boghosian, V. Parvulescu, S.M. Jung, and P. Grange, *J. Catal.*, **217** (2003) 172
- [100]. Z. Huang, Z. Zhu, Z. Liu, and Q. Liu, *J. Catal.*, **214** (2003) 213.
- [101]. S. Zhuiykov, W. Wlodarski, and Y. Li, *Sens. Actuators B*, **77** (2001) 484
- [102]. S. Passerini, A.L. Tipton, and W.H. Smyrl, *Sol. Energy Mater. Sol. Cells*, **39** (1995) 167
- [103]. C. Julien, H. Poniatowski, C. Lopez, M.A. Escobar-Alarcon, *J. Jarquin, Mater. Sci. Eng. B*, **65** (1999), 170
- [104]. C. Delmas, H. Cognac-Auradou, J. M. Cocciantelli, M. Ménétrier and J. P. Doumerc, *Solid State Ionics*, **69** (1994) 257
- [105]. F. Coustier, S. Passerini, and W. H. Smyrl, *J. Electrochem. Soc.*, **145** (1998) L73
- [106]. Z. Lu , M.D. Levi, G. Salitra, Y. Gofer, E. Levi, D. Aurbach, *J. Electroanal. Chem.*, **491** (2000) 211
- [107]. K. West, B. Zachau-Christiansen, S. Skaarup and F.W. Poulsen, *Solid State Ionics*, **57** (1992) 41
- [108]. Y.J. Park, K.S. Ryu, K.M. Kim, N.G. Park, M.G. Kang and S.H. Chang, *Solid State Ionics*, **154** (2002) 229

- [109]. S.C. Mui, J. Jasinski, V. J Leppert, M. Mitome, D.R Sadoway, A.M Mayes, *J. Electrochem. Soc.*, **153** (2006) A1372
- [110]. A. Benayad, H. Martinez, A. Gies, B. Pecquenard, A. Levasseur, D. Gonbeau, *Journal of Electron Spectroscopy and Related Phenomena*, **150** (2006) 1
- [111]. T. Szorenyi, K. Bali, I. Hevesi, *Journal of Non-Crystalline Solids*, **35-36(2)** (1980) 1245
- [112]. K. Inumaru, T. Okuhara, M. Misono, N. Matsubayashi, H. Shimada, A. Nishijima, *Journal of the Chemical Society, Faraday Transactions*, **88** (1992) 625
- [113]. R. Lindstrom, V. Maurice, S. Zanna, L. Klein, H. Groult, L. Perrigaud, C. Cohen, P. Marcus, *Surface and Interface Analysis* , **38** (2006) 6
- [114]. J. Swiatowska-Mrowieck, V. Maurice, S. Zanna, L. Klein, E. Briand, I. Vickridge, P. Marcus, *Journal of Power Sources*, **170** (2007) 160
- [115]. G.J. Fang, Z.L. Liu, Y. Wang, Y.H. Liu and K.L. Yao, *J. Vac. Sci. Technol. A*, **19** (2001) 887
- [116]. A. Mantoux, H. Groult, E. Balnois, P. Doppelt and L. Gueroudji, *J. Electrochem. Soc.*, **151** (2004) A368
- [117]. D.B. Le, S. Passerini, A.L. Tipton, B.B. Owens and W.H. Smyrl, *J. Electrochem. Soc.*, **142** (1995) L102
- [118]. A. Talledo, C.G. Granqvist, *J. Appl. Phys.*, **77** (1995) 4655
- [119]. Z. Wang, J. Chen, and X. Hu, *Thin Solid Films*, **375** (2000) 238.

- [120]. N. Ózer, *Thin Solid Films*, **305** (1997) 80
- [121]. A. Gies, B. Pecquenard A. Benayad, H. Martinez, D. Gonbeau, H. Fues and A. Levasseur, *Solid State Ionics*, **176** (2005) 1627
- [122]. V. Vivier, J. Farcy, and J-P Pereira-Ramos, *Electrochimica Acta*, **44**, (1998) 831
- [123]. T. Watanabe, Y. Ikeda, Takashi Ono, M. Hibino, M. Hosoda, K. Sakai, T. Kudo, *Solid State Ionics*, **151** (2002) 313
- [124]. Y. Wang , K. Takahashi , K. H. Lee , G. Z. Cao, *Adv. Funct. Mater*, **16** (2006) 1133
- [125]. R.J.D. Tilley, *Defect crystal chemistry and its applications*, Blackie Glasgow and London, 1987
- [126]. K-S Hwang, J-H. Ahn, B-H. Kim, *J Mater. Sci.* **41** (2006) 3151
- [127]. J. Livage, *Chem. Mater*, **3** (1991) 578
- [128]. C.J. Brinker and G.W. Scherer, *Sol-gel Science, the Physics and Chemistry of Sol-Gel processing*, Academic Press, New York, 1990
- [129]. B. Alonso and J. Livage, *J. Solid State Chem.*, **148** (1999) 16
- [130]. C. Julien, J. P. Guesdon, A. Gorenstein, A. Khelfa and I. Ivanov, *Appl. Surf. Science*, **90** (1995) 389
- [131]. S-H Lee, H. M. Cheong, M. J. Seong, P. Liu, C. E. Tracy, A. Mascarenhas, J. Roland Pitts and S. K. Deb, *Solid State Ionics*, **165** (2003) 111

- [132]. G. J. Fang, Z.L. Liu, Y.Q. Wang, H.H. Liu and K.L. Yao, *J. Phys. D: Appl. Phys.*, **33** (2000) 3018
- [133]. L. Abello, E. Husson, Y. Repelin, and G. Lucazeau, *Spectrochimica Acta*, **39** (1983) 641
- [134]. M. B. Sahana, C. Sudakar, C. Thapa, G. Lawes, V. M. Naik, R. J. Baird, G. W. Auner, R. Naik, K. R. Padmanabhan, *Material Science and Engineering B*, **143** (2007) 42-50
- [135]. J. Haber, M. Witko, and R. Tokarz, *Appl. Catal. A*, **157** (1997) 3
- [136]. Y. Zavalij and M.S. Whittingham, *Acta Cryst.*, **B55** (1999) 627
- [137]. M.B. Sahana, G.N. Subbanna, S.A. Shivashankar, *J. Appl. Phys.*, **92** (2002) 6495
- [138]. M.B. Sahana, S.A. Shivashankar, *J. Mater. Res.*, **19** (2004) 2859
- [139]. C.V. Ramana, O.M. Hussain, B. Srinivasulu-Naidu and P.J. Reddy, *Thin Solid Films*, **305** (1997) 219
- [140]. C.V. Ramana, O.M. Hussain, S. Uthanna and B. Srinivasulu Naidu, *Opt. Mater.*, **10** (1998) 101
- [141]. P.M.S. Monk, *Fundamentals of Electroanalytical Chemistry*, Wiley, New York, 2001
- [142]. K. Nagase, Y. Shimizu, N. Miura, and N. Yamazoe, *Appl. Phys. Lett.*, **60** (1992) 802
- [143]. M. Benmoussa, A. Outzourhit, A. Bennouna and E. L. Ameziane, *Thin Solid films*, **405** (2002) 11

- [144]. H-K. Kim, T-Y. Seong and Y. S. Yoon, *J. Vac. Sci. and Techn., B*, **21** (2003) 754
- [145]. M.G. Minett, and J. R. Owen, *J. Power Sources*, **32** (1990) 81
- [146]. A. Davies, R.J. Hobson, M. J. Hudson, W. J. Macklin, J. Williamand R.J. Neat, *J. Mat. Chem.* **6** (1996) 49
- [147]. N. Özer, S. Sabuncu, and J. Cronin, *Thin Solid Films*, **338** (1999) 201.
- [148]. K. Lee and G. Cao, *J. Phys. Chem. B* **109** (2005) 11880
- [149]. J. Haber, M. Witko and R. Tokarz, *Appl. Catalysis A: General*, **157** (1997) 3
- [150]. A. Talledo and C. G. Granqvist, *J. Phys. D: Appl. Phys.*, **27** (1994) 2445
- [151]. L. Abello, E. Husson, Y. Repelin, and G. Lucazeau, *Spectrochimica Acta*, **39** (1983) 641
- [152]. C. Delmas, H. Cognac-Auradou, J. M. Cocciantelli, M. Menetrier and J. P. Doumerc, *Solid State Ionics*, **69** (1994) 257
- [153]. P. Sawunyama, A. Yasumori, and K. Okada, *M R S Bulletin*, **33** (1998) 795
- [154]. F. Babonneau, A. Leautic, and J. Livage, *Mater. Res. Soc. Symp. Proc.*, **121** (1988,) 317
- [155]. M.B. Sahana, C. Sudakar, C. Thapa, V.M. Naik, G.W. Auner, R. Naik, K.R. Padmanabhan, *Thin Solid Films*, **517** (2009) 6642-6651

- [156]. D.P. Partlow, S.R. Gurkovich, K.C. Radford, and L.J. Denes, *J. Appl. Phys.* **70** (1991) 443
- [157]. C.H. Griffiths and H.K. Eastwood, *J. Appl. Phys.*, **45** (1974) 2201
- [158]. G. Anderson, *Acta. Chem. Scand.*, **10** (1956) 623
- [159]. J. B. Mcchesney and H. J. Guggenheim, *J. Phys. Chem. Solids*, **30** (1969) 225
- [160]. K. Kosuge, *J. Phys. Chem. Solids*, **28** (1967) 1613
- [161]. C. Julien, J. P. Guesdon, A. Gorenstein, A. Khelfa and I. Ivanov, *Appl. Surf. Sci.*, **90** (1995) 389
- [162]. S-H Lee, H. M. Cheong, M. J. Seong, P. Liu, C. E. Tracy, A. Mascarenhas, J. Roland Pitts, and S. K. Deb, *Solid State Ionics*, **165** (2003) 111
- [163]. G. J. Fang, Z.L. Liu, Y.Q. Wang, H.H. Liu and K.L. Yao, *J. Phys. D: Appl. Phys.*, **33** (2000) 3018
- [164]. S. P. S. Porto, P. A. Fleury, and T. C. Damen, *Phys. Rev.*, **154** (1967) 522
- [165]. D. B. Le, S. Passerini, J. Guo, J. Ressler, B. B. Owens, and W. H. Smyrl, *J. Electrochem. Soc.*, **143** (1996) 2099
- [166]. D. S. Su, M. Wieske, E. Beckmann, A. Blume, G. Mestl and R. Schlogl, *Catalysis Lett.*, **75** (2001) 81
- [167]. C.V. Ramana, O.M. Hussain, B. Srinivasulu-Naidu and P.J. Reddy, *Thin Solid Films*, **305** (1997) 219

- [168]. C.V. Ramana, O.M. Hussain, S. Uthanna and B. S. Naidu, *Opt. Mater.* **10** (1998) 101
- [169]. A. Talledo, C.G. Granqvist, *J. Appl. Phys.*, **77** (1995) 4655
- [170]. A. Ohtomo, M. Kawasaki, T. Koida, K. Masubuchi, H. Koinuma, Y. Sakurai, Y. Yoshida, T. Yasuda and Y. Segawa, *Appl. Phys. Lett.*, **72** (1998) 2466
- [171]. T. Ohzuku, Z. Takehara and S. Yoshizawa, *Electrochimica Acta*, **24** (1979) 219
- [172]. F. Bonino, L. Busani, M. Lazzari, M. Manstretta, B. Rivolta and B. Scrosati, *J. Power Sources* **6** (1981) 261
- [173]. K. Nagase, Y. Shimizu, N. Miura, and N. Yamazoe, *Appl. Phys. Lett.*, **60** (1992) 802
- [174]. M. Benmoussa, A. Outzourhit, A. Bennouna and E. L. Ameziane, *Thin Solid films*, **405** (2002) 11
- [175]. P.M.S. Monk, *Fundamentals of Electroanalytical Chemistry*, Wiley, New York, 2001
- [176]. A. Šurca, S. Benčič, B. Orel, B. Pihlar, *Electrochim. Acta*, **44** (1999) 3075
- [177]. D. Mergela, D. Buschendorf, S. Eggert, R. Grammesb, B. Samset, *Thin Solid Films*, **371** (2000) 218-224
- [178]. C.N. Wilmsen, *Physics and Chemistry of Compound III–V, Semiconductor Interfaces*, Plenum Press, New York (1985)

- [179]. L. Messick, *J. Appl. Phys.*, **47** (1976) 4949
- [180]. Y.H. Lee, K.K. Chan, M.J. Brady, *J Vac Sci Technol A*, **13** (1995) 596
- [181]. J.H. Noh, H.S. Jung, J-K Lee, J-R Kim, K.S. Hon, *Journal of the European Ceramic Society*, **27** (2007) 2937– 2940
- [182]. S.S. Huang, J.S. Chen, *J. Mater. Sci., Mater. Electron.* **13** (2002) 77
- [183]. B.H. Lee, Y. Jeon, K. Zawadzki, W.J. Qi, J. Lee, *Appl. Phys. Lett.*, **74** (1999) 3143
- [184]. H. Seager, *Solid State Communications*, **20** (1976) 539-542
- [185]. G-R Gu, Y-A Li, Y-C Tao, Z. He, J-J Li, H. Yin, W-Q Li, Y-N Zhao, *Vacuum*, **71** (2003) 487–490
- [186]. M. J. Lee, K. S. Chung, J. I. Han, W. K. Kim, S. J. Hong and S. K. Park, *J. Korean Phys. Soc.*, **39** (2001) 686
- [187]. N. D. Young, G. Harkin, R. M. Bunn, D. J. McCulloch, R. W. Wilks and A. G. Knapp, *IEEE Electron Dev. Lett.*, **18** (1997) 19

ABSTRACT**A STUDY OF STRUCTURE-PROPERTY CORRELATION IN V₂O₅ AND TiO₂
BASED THIN FILMS AS FUNCTIONAL MATERIALS**

by

CHANDRA THAPA**August 2010****Advisor:** Dr. Ratna Naik**Co-Advisor:** Dr. K. R. Padmanabhan**Major:** Physics**Degree:** Doctor of Philosophy

The focus of this thesis is to study the structure-property correlation in thin films of V₂O₅ and TiO₂ based transition metal oxides as functional materials. V₂O₅ is investigated as a cathode material for lithium ion battery and TiO₂ as a high-k dielectric material.

We studied V₂O₅ thin films prepared by spin coating using three different types of precursors, MOD precursor, sol-gel organic precursor and sol-gel inorganic precursor. On the basis of structural and electrochemical studies, we find that the capacity is dependent on the degree of non-stoichiometry. We have also studied the effect of addition of Ti. Although Ti doping enhances non-stoichiometry, the capacity

was found to increase only in 5% Ti-doped sol-gel film. This means the optimal degree of non-stoichiometry is crucial to enhance the capacity.

TiO₂ is one of the possible high-k dielectric materials because of its very high dielectric constant. We studied leakage characteristics, the dielectric strength and frequency dependent behavior of dielectric constant of TiO₂ thin films prepared by MOD, sputter deposition and annealed at different temperatures. We find dielectric constant increasing with the increase in annealing temperature and leakage current density improvement by almost one order of magnitude with each 100 °C increase in annealing temperature. Since TiO₂ possess two distinct thermodynamic phases: anatase and rutile, which dramatically influences the values of dielectric constant and leakage current density, it is crucial to stabilize the phase of TiO₂ by doping. We find that 20% Zr-doping completely stabilizes TiO₂ phase in its anatase form. The dielectric constant of the films is independent of annealing temperature but the leakage current density improves by one order of magnitude with every 100 °C increase in annealing temperature.

Autobiographical Statement

CHANDRA THAPA

Education:

PhD, Physics, Wayne State University, Detroit, MI, USA, Expected 2010

M. S., Physics, Wayne State University, Detroit, MI, USA, 2006

M. Sc., Physics, Tribhuvan University, Kathmandu, Nepal, 1997

B. Sc., Physical Science, Tribhuvan University, Pokhara, Nepal, 1990

I. Sc., Physical Science, Tribhuvan University, Pokhara, Nepal, 1988

High School, Janata High School, Baglung, Nepal, 1986

Work Experience:

Graduate Teaching/Research Assistant, WSU, MI, USA, 2003-2009

Founder/Teacher, MDM High School, Kathmandu, Nepal, 1997-2003

Science/Math Teacher, SJ High School, Baglung, Nepal, 1990-1994

Membership: American Physical Society and Nepal Physical Society

Publications:

1. M.B. Sahana , C. Sudakar, C. Thapa, G. Lawes, V.M. Naik, R.J. Baird, G.W. Auner, R. Naik, K.R. Padmanabhan, 'Electrochemical properties of V_2O_5 thin films deposited by spin coating', *Materials Science and Engineering B*, **143** (2007) 42–50
2. M.B. Sahana, C. Sudakar, C. Thapa, V.M. Naik, G.W. Auner, R. Naik, K.R. Padmanabhan, 'The effect of titanium on the lithium intercalation capacity of V_2O_5 thin films', *Thin Solid Films*, **517** (2009) 6642–6651

Conference Presentations:

1. 'The effect of titanium on the lithium intercalation capacity of V_2O_5 thin films', APS March meeting, Denver, CO, 2006.
2. 'Dielectric properties of TiO_2 and Zr-doped TiO_2 thin films', Ohio section meeting of America Physical Society, Flint, MI, 2010.